Disease Markers

Microvessel Structure and Microvascular Alterations in Chronic Diseases 2022

Lead Guest Editor: Yi Shao
Guest Editors: Jin Yuan, Qi-Cheng Yang, Wensi Tao, and Nan Jiang

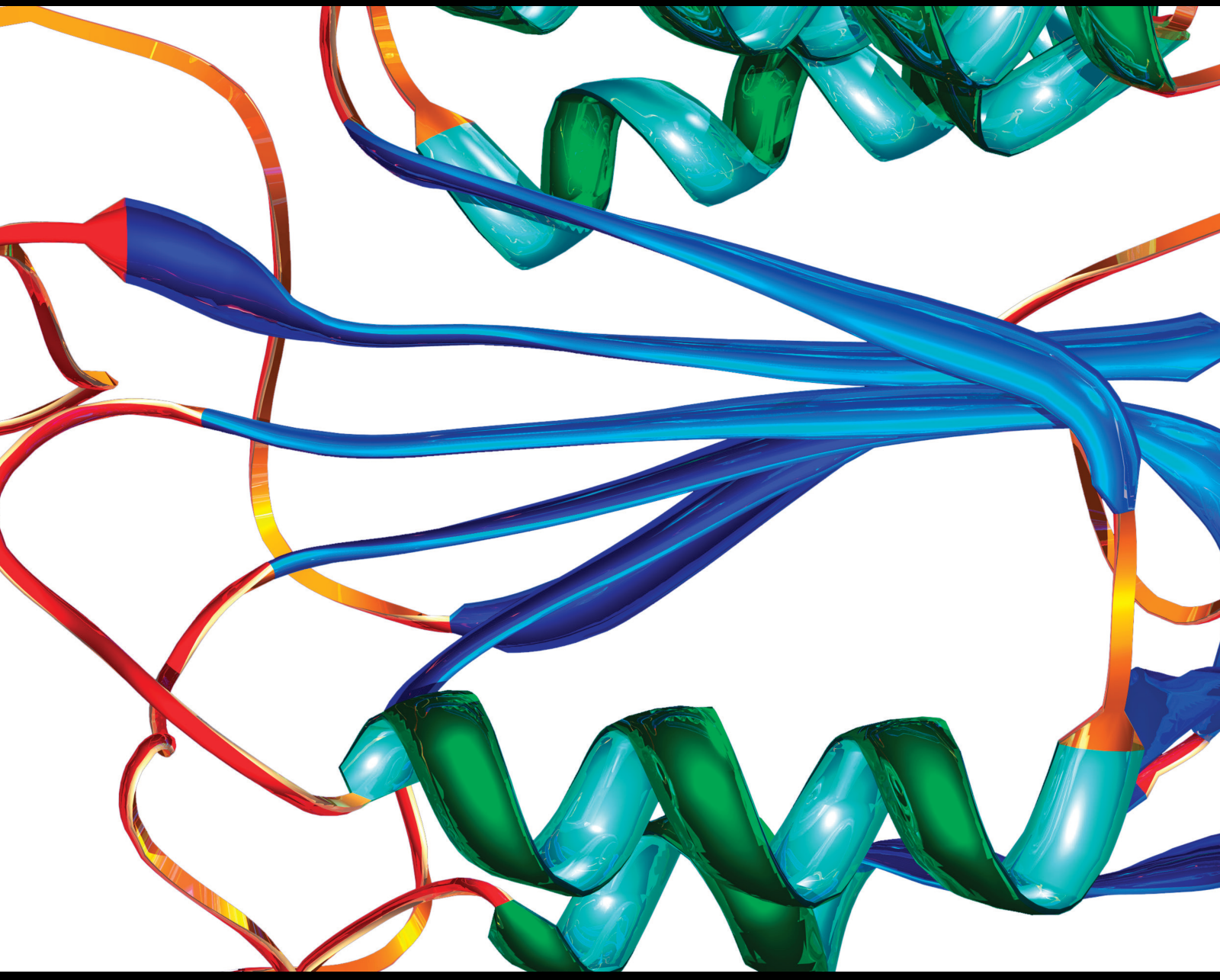

Microvessel Structure and Microvascular Alterations in Chronic Diseases 2022

Disease Markers

Microvessel Structure and Microvascular Alterations in Chronic Diseases 2022

Lead Guest Editor: Yi Shao
Guest Editors: Jin Yuan, Qi-Cheng Yang, Wensi Tao, and Nan Jiang

Chief Editor

Paola Gazzaniga, Italy

Associate Editors

Donald H. Chace, USA
Mariann Harangi, Hungary
Hubertus Himmerich, United Kingdom
Yi-Chia Huang, Taiwan
Giuseppe Murdaca, Italy
Irene Rebelo, Portugal

Academic Editors

Muhammad Abdel Ghafar, Egypt
George Agrogiannis, Greece
Mojgan Alaeddini, Iran
Atif Ali Hashmi, Pakistan
Cornelia Amalinei, Romania
Pasquale Ambrosino, Italy
Paul Ashwood, USA
Faryal Mehwish Awan, Pakistan
Atif Baig, Malaysia
Valeria Barresi, Italy
Lalit Batra, USA
Francesca Belardinilli, Italy
Elisa Belluzzi, Italy
Laura Bergantini, Italy
Sourav Bhattacharya, USA
Anna Birková, Slovakia
Giulia Bivona, Italy
Luisella Bocchio-Chiavetto, Italy
Francesco Paolo Busardó, Italy
Andrea Cabrera-Pastor, Spain
Paolo Cameli, Italy
Chiara Caselli, Italy
Jin Chai, China
Qixing Chen, China
Shaoqiu Chen, USA
Xiangmei Chen, China
Carlo Chiarla, Italy
Marcello Ciaccio, Italy
Luciano Colangelo, Italy
Alexandru Corlateanu, Moldova
Miriana D'Alessandro, Saint Vincent and the Grenadines
Waaqo B. Daddacha, USA
Xi-jian Dai, China
Maria Dalamaga, Greece
Serena Del Turco, Italy
Jiang Du, USA
Xing Du, China
Benoit Dugue, France
Paulina Dumnicka, Poland
Nashwa El-Khazragy, Egypt
Zhe Fan, China
Rudy Foddis, Italy
Serena Fragiotta, Italy
Helge Frieling, Germany
Alain J. Gelibter, Italy
Matteo Giulietti, Italy
Damjan Glavač, Slovenia
Alvaro González, Spain
Rohit Gundamaraju, USA
Emilia Hadziyannis, Greece
Michael Hawkes, Canada
Shih-Ping Hsu, Taiwan
Menghao Huang, USA
Shu-Hong Huang, China
Xuan Huang, China
Ding-Sheng Jiang, China
Esteban Jorge Galarza, Mexico
Mohamed Gomaa Kamel, Japan
Michalis V. Karamouzis, Greece
Muhammad Babar Khawar, Pakistan
Young-Kug Kim, Republic of Korea
Mallikarjuna Korivi, China
Arun Kumar, India
Jinan Li, USA
Peng-fei Li, China
Yiping Li, China
Michael Lichtenauer, Austria
Daniela Ligi, Italy
Hui Liu, China
Jin-Hui Liu, China
Ying Liu, USA
Zhengwen Liu, China
César López-Camarillo, Mexico
Xin Luo, USA
Zhiwen Luo, China
Valentina Magri, Italy
Michele Malaguarnera, Italy
Erminia Manfrin, Italy
Upender Manne, USA

Contents

Hindawi
Disease Markers
Volume 2023, Article ID 1316821, 13 pages
https://doi.org/10.1155/2023/1316821

Research Article

Relationship between Angiotensin II, Vascular Endothelial Growth Factor, and Arteriosclerosis Obliterans

Yulian Liu,[1] Yuzhi Cui,[1] Zongqi Zhou,[1] Bin Liu,[2] Zheng Liu,[3] and Gang Li[2]

[1]*Department of Interventional Diagnosis and Treatment, Tai'an Traditional Chinese Medicine Hospital, Tai'an 271000, China*
[2]*Department of Vascular Surgery, The Second Affiliated Hospital of Shandong First Medical University, Tai'an 271000, China*
[3]*Department of Peripheral Vascular Diseases, Affiliated Hospital of Shandong University of Traditional Chinese Medicine, Jinan 250014, China*

Correspondence should be addressed to Zheng Liu; lz2000jn@163.com and Gang Li; ligang111666@163.com

Received 18 September 2022; Revised 11 November 2022; Accepted 24 November 2022; Published 21 February 2023

Academic Editor: Yi Shao

Objective. To investigate the relationship between angiotensin II (Ang II), vascular endothelial growth factor (VEGF), and arteriosclerosis obliterans (ASO). *Methods*. 60 ASO patients diagnosed and treated from October 2019 to December 2021 were selected for the observation group while 30 healthy physical examiners were for the control group. The general information (gender, age, history of smoking, diabetes, and hypertension) and arterial blood pressure (systolic and diastolic blood pressure) of the two groups were collected, and parameters like disease site and duration, Fontaine stage, and ankle-brachial index (ABI) of ASO patients have been evaluated. Ang II, VEGF, uric acid (UA), low-density lipoprotein (LDL), high-density lipoprotein (HDL), triglyceride (TG), and total cholesterol (TC) were also detected for the two groups. The variations in UA, LDL, HDL, TG, and TC among two groups along with levels of Ang II and VEGF in ASO patients in accordance to conditions like the general situation, disease duration, disease site, Fontaine stage, and ABI risk level have been studied to establish a correlation between Ang II and VEGF and ASO. *Results*. (1) The proportion of males with a history of smoking, diabetes, and hypertension was higher ($P < 0.05$) among ASO patients in comparison to the control group. The diastolic blood pressure, LDL, TC, Ang II, and VEGF levels were found to be higher ($P < 0.05$) whereas HDL was low ($P < 0.01$). (2) The level of Ang II in male patients with ASO was significantly higher than that in female ASO patients ($P < 0.05$). In ASO patients, the levels of Ang II and VEGF increased not only with age ($P < 0.01$) but also with progression in Fontaine stages II, III, and IV ($P < 0.01$). (3) Logistic regression analysis revealed Ang II and VEGF as risk factors for ASO. (4) An AUC (area under the ROC (receiver operator characteristic) curve) for Ang II and VEGF for the diagnosis of ASO was 0.764 (good) and 0.854 (very good), respectively, while their combined AUC in diagnosing ASO was 0.901 (excellent). The AUC of Ang II and VEGF together in diagnosing ASO was greater than that of Ang II and VEGF alone along with higher specificity as well (all $P < 0.05$). *Conclusion*. Ang II and VEGF were correlated with the occurrence and development of ASO. The AUC analysis demonstrates that Ang II and VEGF were highly discriminative of ASO.

1. Introduction

Arteriosclerosis obliterans (ASO) is a common peripheral arterial occlusive disease. It is manifested in systemic arteriosclerosis in the arteries of the lower limbs. In the early stages, the clinical manifestations involve limb cooling, fear of cold, numbness, intermittent claudication, etc. In the later stages, ulceration and gangrene may occur with amputation occurrence in serious cases [1]. ASO has been reported to involve more middle-aged and elderly people (over 45 years old) also with more males than females [2]. It is also reported that the incidence rate of ASO is as high as 15%~20%, and the annual mortality is 4%~6% [3]. As China's population ages, the incidence rate of ASO is increasing year by year

affecting both physical and mental health as well as patient quality of life [4]. Atherosclerosis (AS) is the pathological basis of ASO [5] where the pathogenesis of AS is complex and there are many theories about it. Among them, the theory of chronic inflammation had played a crucial role in studying AS pathogenesis and also received widespread attention in the medical community [6, 7].

In 1997, researchers first found that Ang II can induce endothelial cells to produce adhesion molecules, which are closely related to inflammation. With the deepening of research, a new idea has been proposed that Ang II can cause inflammation and participate in the pathogenesis of AS [8].

Angiotensin II (Ang II) can induce the aggregation of a variety of inflammatory cytokines, lead to the proliferation of the middle layer of the artery, and promote inflammatory infiltration in the surrounding area of the middle layer of the artery, thus accelerating the development of AS. Its advantages in evaluation are increasingly prominent [9]. In addition, the abnormal proliferation of vascular smooth muscle cells (VSMCs) also plays an important role in the development of AS. As a critical functional factor of the renin-angiotensin-aldosterone system (RAAS), Ang II can act on VSMCs through autocrine and paracrine pathways, thus stimulating the abnormal proliferation of VSMCs [10] and stimulating angiogenesis in lower concentrations but inhibits in higher concentrations [11]. The process of angiogenesis involves the differentiation, proliferation, and migration of endothelial cells (ECs) and results in tubulogenesis and formation of vessels [12]. Ang II promotes EC proliferation and angiogenesis through the angiotensin type 1 receptor (AT1R) [13, 14]. Buharaliogl et al. found that Ang II-induced angiogenesis was phosphorylated by splenic tyrosine-mediated kinase through VEGF receptor-1.

Vascular endothelial growth factor (VEGF) is a highly specific mitogen of vascular endothelial cells [15] that can induce endothelial cell proliferation, increase vascular permeability, and promote inflammatory response [16]. Studies have found that once neovascularization occurs in AS plaques, the expression of VEGF and its receptor in AS plaques will increase, so it is inferred that there is a close association between VEGF expression and the development of AS plaques [17–20]. Simultaneously, studies have also confirmed [21] that VEGF has strong expression in smooth muscle and macrophages of atherosclerotic plaques. VEGF plays a crucial role in the formation of AS, which may be due to the fact that although VEGF can promote angiogenesis; these new blood vessels are often immature and prone to rupture, leading to thrombosis, and in-cooperated with highly expressed fibrinogen (FIB) to accelerate the formation and development of AS [22]. Meanwhile, studies have found that VEGF and its receptor are critically linked to the abnormal proliferation of VSMCs [23]. This study intends to explore the characteristics variations of Ang II and VEGF levels in ASO patients for preliminarily exploring the relationship between Ang II, VEGF, and ASO.

2. Material

Main experimental reagent and software product information.

3. Methods

3.1. Study Subjects. The subjects in the observation group were all ASO patients hospitalized in the peripheral vascular department of the Affiliated Hospital of Shandong University of Traditional Chinese Medicine from October 2019 to December 2021. The control groups were all from the health checkers in the physical examination center of the Affiliated Hospital at Shandong University of Traditional Chinese Medicine. This study was approved by the Ethics Committee of the Affiliated Hospital of Shandong University of Traditional Chinese Medicine ((2022) Lunlun-Review No. (108) -KY). The following data have been utilized as diagnostic criteria: ASO western medical diagnostic criteria [24] with (1) age > 40 years old; (2) history of smoking, diabetes, hypertension, hyperlipidemia, and other high-risk factors; (3) clinical manifestations of ASO in lower limbs; (4) arterial pulsation in the distal end of the ischemic limb weakened or disappeared; and (5) ABI ≤ 0.9; (6) color doppler ultrasound, CTA, MRA, DSA, and other imaging examinations showed stenosis or occlusion of the corresponding arteries. A clinical diagnosis of ASO can be made by meeting the following 4 diagnostic criteria: Fontaine staging standard [25] stage I: asymptomatic, stage II: intermittent claudication, stage III: resting pain, and stage IV: tissue ulcer and gangrene. The following case inclusion criteria were utilized: (1) those who met the diagnostic criteria of ASO, (2) 40 years old < age ≤ 80 years old, and (3) those who have signed the informed consent form. The following were case exclusion criteria: (1) those who have suffered from serious cardiovascular and cerebrovascular diseases in the past 3 months; (2) accompanied by serious infectious diseases, malignant tumors, and autoimmune diseases; (3) pregnant and lactating women; (4) those who have a mental illness or are unable to cooperate; and (5) incomplete data affecting judgment.

3.2. Study Subjects and Grouping. A total of sixty ASO patients who met the natriuretic excretion criteria were set as an observation group while 30 healthy physical examiners during the same period acted as a control group.

3.3. Clinical and Laboratory Variables. This represents the general data where the following clinical indicators were used: (1) gender, (2) age, (3) disease duration, (4) the site of the disease, (5) Fontaine staging, (6) smoking history, (7) history of diabetes, and (8) history of hypertension. The following parameters were utilized as laboratory variables for the detection of AS like (1) blood pressure: systolic blood pressure and diastolic blood pressure, (2) angiotensin II (Ang II), (3) vascular endothelial growth factor (VEGF), (4) ankle-brachial index (ABI), and (5) biochemical indicators: low-density lipoprotein (LDL), high-density lipoprotein (HDL), triglyceride (TG), total cholesterol (TC), and uric acid (UA).

3.4. Study Procedures. The following study procedures were utilized for this study that involves (1) measurement method of blood pressure: the subject rested calmly for 5 min before receiving the examination, took a sitting or lying position, used a mercury sphygmomanometer to measure three times,

and calculated the average value of three times of blood pressure. The blood pressure of both arms was measured while the higher one was taken as the final blood pressure. (2) Measurement method of ABI: Nicolet vasoguard + channel blood vessel tester was used, and special personnel was assigned to detect it. The ABI of both sides was detected, and the lower was taken as the final value. (3) 3 ml of peripheral venous blood in fasting decubitus position was taken into a centrifuge after standing for 1 h at normal temperature, plasma was taken after centrifugation, and it was stored at -70°C for Ang II detection. Plasma Ang II was determined by radioimmunoassay. (4) 5 ml of fasting peripheral venous blood was taken and placed in the coagulation-promoting tube, centrifuged at 4000 r/min for 5 min, the upper serum was taken for examination, and serum VEGF was measured with enzyme-linked immunosorbent assay. (5) 2 ml of fasting peripheral venous blood was taken, and LDL, HDL, TG, TC, and UA were detected by AU5800 automatic biochemical analyzer (model: 5821, no. DSH-001).

3.5. Statistical Analysis. The statistical software IBM SPSS28.0 has been utilized for data processing. All measured data were expressed as mean ± standard deviation ($x \pm s$). T -test was used for the comparison of data conforming to normal distribution and homogeneity of variance, and analysis of variance was used for the comparison among multiple groups. Nonparametric test was used for data not conforming to normal distribution. The count data were expressed by frequency and composition ratio (n (%)). We have utilized the X^2 test, a binary logistic regression model for correlation analysis; the ROC curves for the diagnostic value of the detection index and the AUC of ROC is compared by Medcalc software. The P values ($P < 0.05$) were statistically considerable.

4. Results

4.1. Subject Demographics and Study Variables. In the 60 cases in the observation group, around 42 were males, and 18 females with an average age of 60.57 ± 6.16 years were found. The shortest disease period was of 1 year while the longest of 28 years with an average duration of 5.47 ± 6.00 years. There were 13 cases located in the left lower limb, 26 in the right lower limb, and 21 in both lower limbs. According to the Fontaine stage, there were 14, 7, and 39 cases in stages II, III, and IV, respectively. Of the 30 cases in the control group, there were 11 males and 19 females with an average age of 58.07 ± 9.38 years.

As compared to the control group, a higher proportion of males with a history of smoking as well as diabetes were found in the observation group and also the levels of diastolic blood pressure, TC, Ang II (Figure 1), and VEGF (Figure 2) were higher while the HDL level was lower. These variations among the two groups were statistically considerable with P values ($P < 0.01$). In comparison to the control group, the proportion of hypertension history and LDL level in the observation group was higher; also, these differences between the two groups were statistically considerable with P values ($P < 0.05$). We have not found any statistically considerable differences in age, systolic blood pressure, TG, and UA between the two groups ($P > 0.05$) (Table 1).

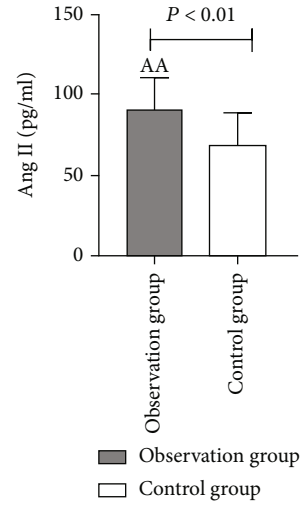

Figure 1: Comparison of Ang II levels between the two groups.

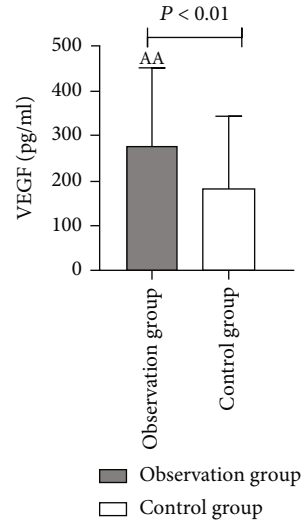

Figure 2: Comparison of VEGF levels between the two groups.

4.2. Comparisons within Stratified Subgroups of Cases. A total of sixty ASO patients were stratified according to gender, age, duration, and site of disease, diabetes and hypertension history, Fontaine stage, and ABI risk grade; and the changes in Ang II and VEGF levels were observed. We have found the following results for Ang II and VEGF comparison with different parameters.

4.3. Comparison of Ang II and VEGF Levels between Different Genders of ASO Patients. The level of Ang II was found higher in males than females for 60 cases of ASO, and the difference between the two groups was statistically significant ($t = -2.542$, $P = 0.019$). The VEGF level was also found higher in males than females but without any statistically considerable difference between the two groups ($Z = -0.355$, $P = 0.723$) (Table 2 and Figures 3 and 4).

Table 1: Clinical data from the observation group compared to the control group.

	Observation group ($n = 60$)	Control group ($n = 30$)	P value
Gender (%)			
Male	42 (70.00)	11 (36.67)	0.002
Female	18 (30.00)	19 (63.33)	
Smoking history (%)			
Yes	27 (45.00)	3 (10.00)	0.001
No	33 (55.00)	27 (90.00)	
History of diabetes (%)			
Yes	36 (60.00)	5 (16.67)	≤0.001
No	24 (40.00)	25 (83.33)	
History of hypertension (%)			
Yes	35 (58.33)	9 (30.00)	0.011
No	25 (41.67)	21 (70.00)	
Blood pressure (mmHg)			
Systolic blood pressure	141.80 ± 19.29	136.33 ± 20.20	0.215
Diastolic blood pressure	88.10 ± 10.25^{aa}	80.30 ± 12.60	0.004
Age (years)	60.57 ± 6.16	58.07 ± 9.38	0.171
LDL (mmol/L)	3.03 ± 0.93^{a}	2.62 ± 0.86	0.040
HDL (mmol/L)	0.94 ± 0.22^{aa}	1.18 ± 0.34	≤0.001
TG (mmol/L)	1.77 ± 0.77	1.16 ± 0.43	0.764
TC (mmol/L)	4.83 ± 1.10^{aa}	4.12 ± 1.04	0.004
UA (μmol/L)	326.08 ± 98.41	347.33 ± 81.46	0.311
Ang II (pg/ml)	90.66 ± 19.69^{aa}	68.80 ± 20.02	≤0.001
VEGF (pg/ml)	277.7 ± 171.60^{aa}	182.08 ± 162.40	≤0.001

Note: compared with the control group, $^{a}P < 0.05$, and $^{aa}P < 0.01$.

Table 2: Comparison of Ang II and VEGF levels between different genders of ASO patients.

Group	n	Ang II (pg/ml)	VEGF (pg/ml)
Male	42	101.98 ± 25.22^{b}	278.22 ± 175.80
Female	18	85.81 ± 14.63	276.51 ± 166.32
T value/Z value		-2.542	-0.355
P value		0.019	0.723

Note: compared with females, $^{b}P < 0.05$.

4.4. Comparison of Ang II and VEGF Levels in ASO Patients at Different Ages. 60 patients with ASO were divided into groups according to the age interval of 10 years. There were 3 patients aged 41 to 50 years, 23 patients aged 51 to 60 years, 31 patients aged 61 to 70 years, and 3 patients aged 71 to 80 years. We have found that, with an increase in age, the levels of Ang II and VEGF also increased in ASO patients, and the difference was statistically significant as analyzed by the Kruskal-Wallis H test ($P < 0.01$). Further, the level of Ang II in the 61-70 years old age group was significantly higher than that in the 41-50 years old group ($P < 0.01$), and there was not any statistically considerable difference between the other two groups ($P > 0.05$). Also, the VEGF level in the 71-80 years old group was found higher than that of the 41-50 years old group ($P < 0.01$) while there was not any statistically considerable difference between the other two groups ($P > 0.05$) (Table 3 and Figures 5 and 6).

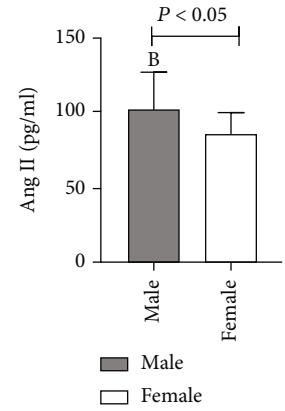

Figure 3: Comparison of Ang II levels in ASO patients with different genders.

4.5. Comparison of Ang II as well as VEGF Levels among Patients with ASO at Different Sites. Sixty patients with ASO were divided into three groups according to the different disease sites including 13, 26, and 21 cases at the left

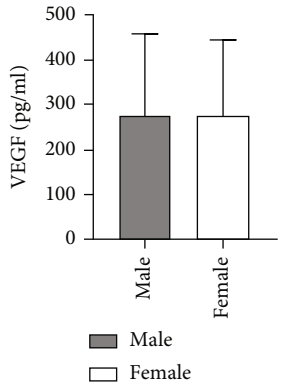

Figure 4: Comparison of VEGF levels in ASO patients of different genders.

Table 3: Comparison of Ang II and VEGF levels in ASO patients at different ages.

Group	n	Ang II (pg/ml)	VEGF (pg/ml)
41~50 years	3	68.36 ± 3.92	243.52 ± 38.78
51~60 years	23	85.18 ± 20.98	251.34 ± 174.94
61~70 years	31	91.76 ± 18.25^{cc}	256.09 ± 90.97
71~80 years	3	97.58 ± 19.28	282.45 ± 158.58^{cc}
P value		0.006	0.001

Note: compared with the 41-50-year-old group, $^{cc}P < 0.01$.

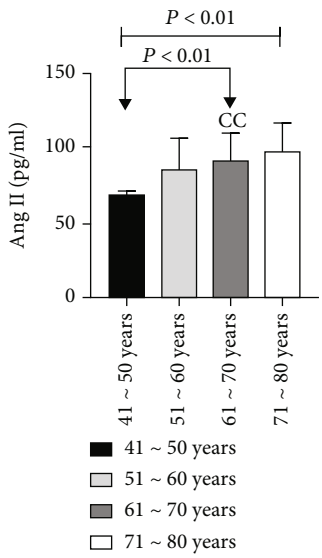

Figure 5: Comparison of Ang II levels among ASO patients of different ages.

lower limb, right lower limb, and both lower limbs, respectively. Kruskal-Wallis H test showed that there was not any statistically considerable difference for Ang II as well as VEGF levels among these groups ($P > 0.05$) (Table 4 and Figures 7 and 8).

4.6. Comparison of Ang II as well as VEGF Levels among ASO Patients with Different Disease Durations. We grouped 60

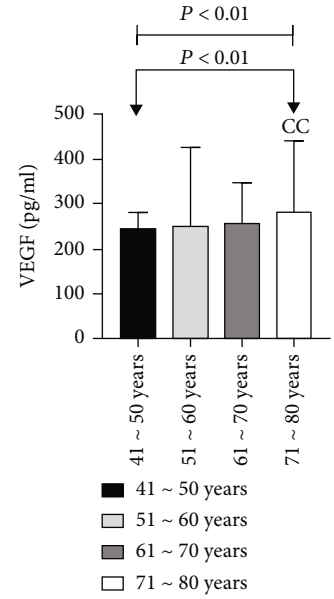

Figure 6: Comparison of VEGF levels in ASO patients of different ages.

Table 4: Comparison of Ang II as well as VEGF levels among patients with ASO at different sites.

Group	n	Ang II (pg/ml)	VEGF (pg/ml)
Left lower limb	13	84.65 ± 19.02	242.34 ± 124.67
Right lower limb	26	89.13 ± 19.40	226.22 ± 152.74
Lower limbs	21	90.19 ± 20.11	267.15 ± 183.91
P value		0.426	0.549

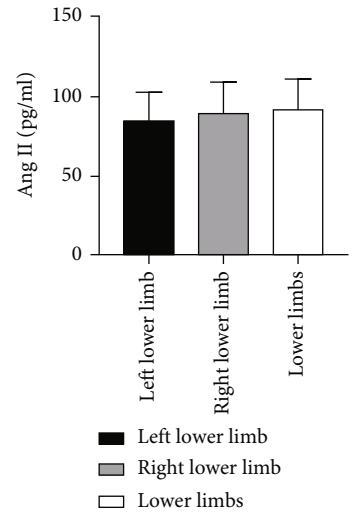

Figure 7: Comparison of Ang II levels among different sites of ASO patients.

patients with ASO according to the disease duration [26], where 29 patients had a duration of disease ≤ 1 year, 4 cases with 1 year < duration ≤ 3 years, 18 cases with 3 years < duration ≤ 10 years, and 9 cases with disease duration > 10

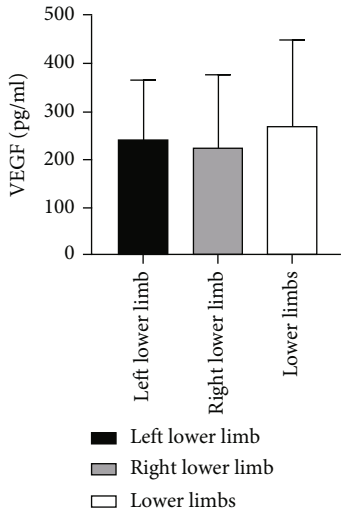

Figure 8: Comparison of VEGF levels in ASO patients with different disease sites.

years. The Kruskal-Wallis H test showed that there was not any statistically considerable difference for Ang II as well as VEGF levels among these groups ($P > 0.05$) (Table 5 and Figures 9 and 10).

4.7. Comparison of Ang II as well as VEGF Levels among Patients of ASO with or without a Smoking History. The level of Ang II in ASO patients with smoking history was higher than that in patients without smoking history, and there was not any statistically considerable difference between the two groups ($Z = -0.333$, $P = 0.739$). Also, higher VEGF levels were found among patients of ASO with smoking history in comparison to patients without smoking history with no statistically considerable difference between the two groups ($Z = -0.287$, $P = 0.774$) (Table 6 and Figures 11 and 12).

4.8. Comparison of Ang II as well as VEGF Levels among ASO Patients with or without a History of Diabetes. A higher level of Ang II was found in patients of ASO with a history of diabetes in comparison to those without any diabetes history. There was not any statistically considerable difference between the two groups ($Z = -0.096$, $P = 0.923$). Also, a higher VEGF level was observed for ASO patients with a history of diabetes in comparison to those without any diabetes history. There was not any statistically considerable difference between the two groups ($Z = -0.836$, $P = 0.403$) (see Table 7 and Figures 13 and 14).

4.9. Comparison of Ang II as well as VEGF Levels among ASO Patients with or without Hypertension. A higher level of Ang II was observed for ASO patients with hypertension history in comparison to those without hypertension, and there was not any statistically considerable difference between the two groups ($Z = -0.952$, $P = 0.341$). Also, a higher VEGF level was found for ASO patients with a hypertension history in comparison to those without a history of hypertension. There was not any statistically considerable difference between the two groups ($Z = -0.247$, $P = 0.805$) (Table 8 and Figures 15 and 16).

Table 5: Comparison of Ang II as well as VEGF levels among ASO patients with different disease durations.

Group	N	Ang II (pg/ml)	VEGF (pg/ml)
The duration of disease ≤ 1 year	29	86.25 ± 14.83	238.91 ± 155.20
1 year < duration ≤ 3 years	4	83.02 ± 14.28	334.99 ± 258.89
3 years < duration ≤ 10 years	18	88.61 ± 24.64	236.52 ± 114.25
Duration > 10 years	9	98.30 ± 21.99	235.21 ± 100.08
P value		0.222	0.912

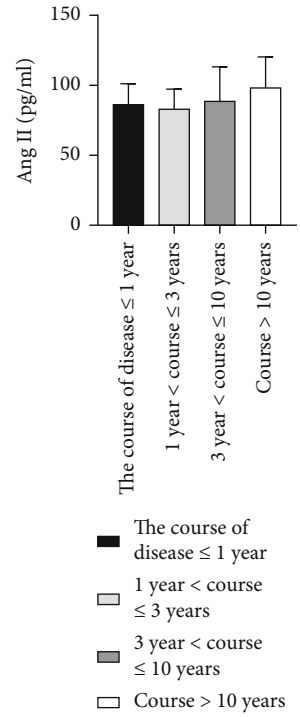

Figure 9: Comparison of Ang II levels in ASO patients with different disease duration groups.

4.10. Comparison of Ang II as well as VEGF Levels among ASO Patients with Different Fontaine Stages. In 60 patients with ASO, the Ang II, as well as VEGF levels among different Fontaine stages, was statistically significant as analyzed by the Kruskal-Wallis H test ($P < 0.01$). Among them, a higher level of Ang II and VEGF was observed for patients with Fontaine III in comparison to patients with Fontaine II with a statistically considerable difference among these groups ($P < 0.05$). Also, significantly higher levels of Ang II and VEGF were observed for patients with Fontaine IV in comparison to patients with Fontaine II with a statistically considerable difference among these ($P < 0.01$). Further, significantly higher levels of Ang II and VEGF were found in

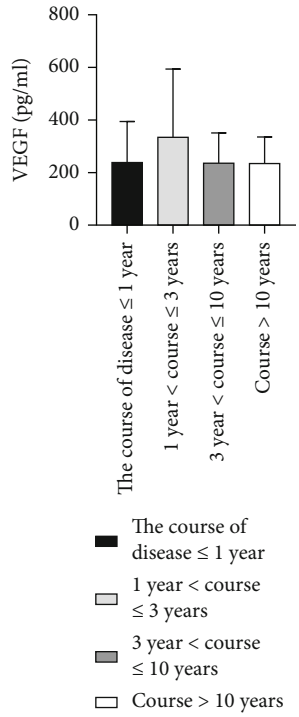

Figure 10: Comparison of VEGF levels in ASO patients with different disease duration groups.

Table 6: Comparison of Ang II as well as VEGF levels among ASO patients with or without a smoking history.

Group	*n*	Ang II (pg/ml)	VEGF (pg/ml)
Smoking history	21	88.94 ± 18.63	252.49 ± 183.46
No smoking history	39	87.83 ± 21.07	228.34 ± 94.56
Z value		-0.333	-0.287
P value		0.739	0.774

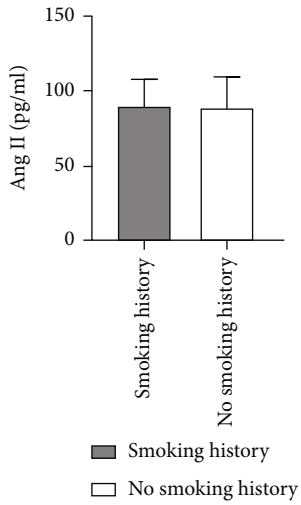

Figure 11: Comparison of Ang II level between ASO patients with and without smoking history.

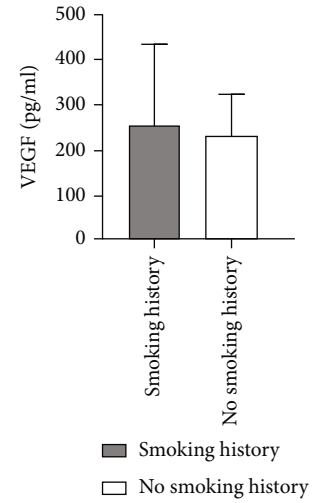

Figure 12: Comparison of VEGF levels between ASO patients with and without smoking history.

Table 7: Comparison of Ang II as well as VEGF levels among ASO patients with or without diabetes history.

Group	*n*	Ang II (pg/ml)	VEGF (pg/ml)
Diabetes	31	89.07 ± 19.24	273.03 ± 197.49
Nondiabetes	29	87.96 ± 19.80	213.05 ± 92.91
Z value		-0.096	-0.836
P value		0.923	0.403

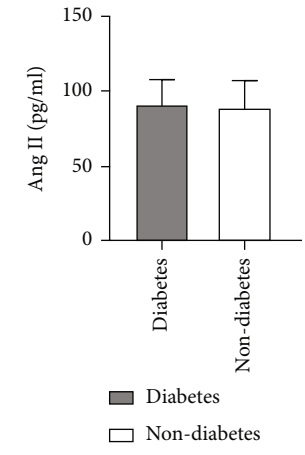

Figure 13: Comparison of Ang II level between ASO patients with and without diabetes history.

the Fontaine IV group in comparison to the Fontaine III group ($P < 0.05$) (Table 9 and Figures 17 and 18).

4.11. Comparison of Ang II as well as VEGF Levels among ASO Patients at Different ABI Risk Levels. According to the ABI of patients, the risk grade was divided [27]: the low-risk group ($0.7 \leq \text{ABI} < 0.9$, $n = 13$), the medium-risk group ($0.4 \leq \text{ABI} < 0.7$, $n = 41$), and the high-risk group ($\text{ABI} < 0.4$, $n = 6$). The levels of Ang II in 60 ASO patients

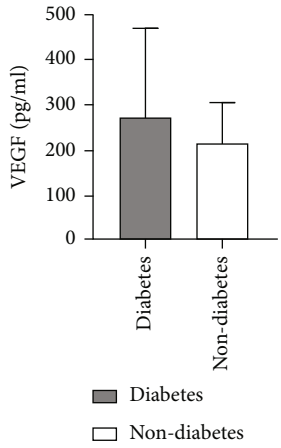

Figure 14: Comparison of VEGF levels between ASO patients with and without diabetes history.

Table 8: Comparison of Ang II as well as VEGF levels among ASO patients with or without hypertension.

Group	n	Ang II (pg/ml)	VEGF (pg/ml)
Hypertension	35	90.42 ± 19.45	259.10 ± 188.27
Nonhypertension	25	85.93 ± 19.29	222.95 ± 100.32
Z value		-0.952	-0.247
P value		0.341	0.805

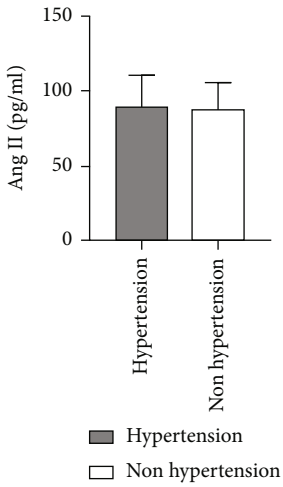

Figure 15: Comparison of Ang II level between ASO patients with and without hypertension history.

with different risk grades were not statistically significant ($P = 0.147$) as analyzed by ANOVA. Also, there was not any statistically considerable difference in VEGF levels among 60 ASO patients with different risk grades as analyzed by the Kruskal-Wallis H test ($P = 0.487$) (Table 10 and Figures 19 and 20).

4.12. Logistic Regression Analysis of Ang II, VEGF, and ASO. The correlation between Ang II, VEGF, and ASO was statistically analyzed. Taking ASO patients as dependent variables

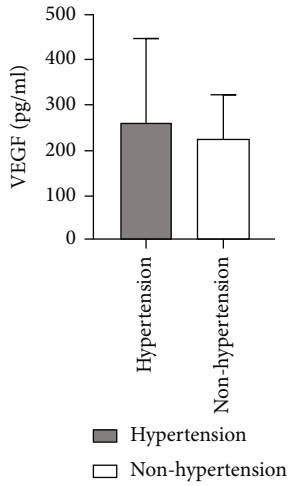

Figure 16: Comparison of VEGF levels between ASO patients with and without hypertension history.

Table 9: Comparison of Ang II as well as VEGF levels among ASO patients at different clinical stages.

Group	n	Ang II (pg/ml)	VEGF (pg/ml)
Fontaine phase II	14	85.39 ± 17.00	189.21 ± 106.46
Fontaine phase III	7	87.72 ± 14.32^{d}	249.68 ± 109.87^{d}
Fontaine phase IV	39	107.81 ± 29.98^{dde}	260.92 ± 177.04^{dde}
P value		0.007	0.001

Note: compared with Fontaine phase II, $^{d}P < 0.05$, and $^{dd}P < 0.01$. Compared with Fontaine III, $^{e}P < 0.05$.

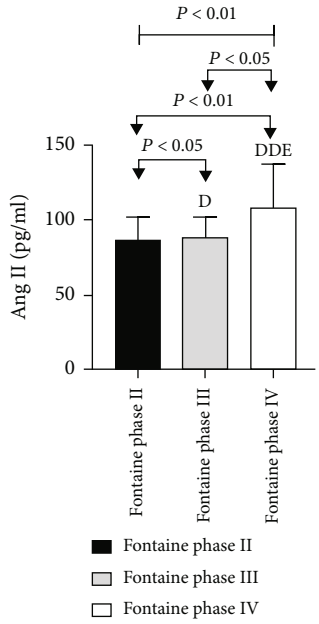

Figure 17: Comparison of Ang II levels in ASO patients with different clinical stages.

while Ang II and VEGF as independent variables, a binary logistic regression analysis was conducted. The results showed that Ang II (partial regression coefficient = 0.038,

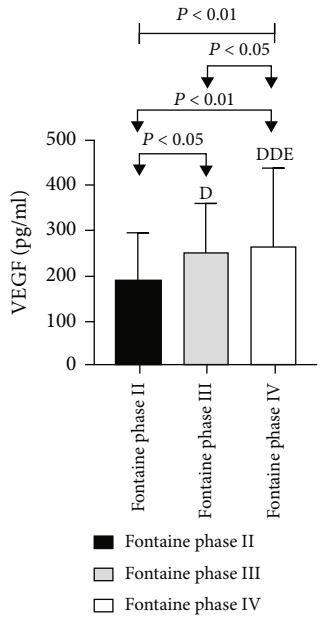

Figure 18: Comparison of VEGF levels in ASO patients with different clinical stages.

Table 10: Comparison of Ang II as well as VEGF levels among ASO patients with different risk grades.

Group	N	Ang II (pg/ml)	VEGF (pg/ml)
Low risk ($0.7 \leq$ ABI ≤ 0.9)	13	96.47 ± 22.11	200.83 ± 96.06
Medium risk ($0.4 \leq$ ABI < 0.7)	41	85.25 ± 15.32	263.95 ± 176.87
High risk (ABI < 0.4)	6	93.98 ± 30.00	201.57 ± 102.29
P value		0.147	0.487

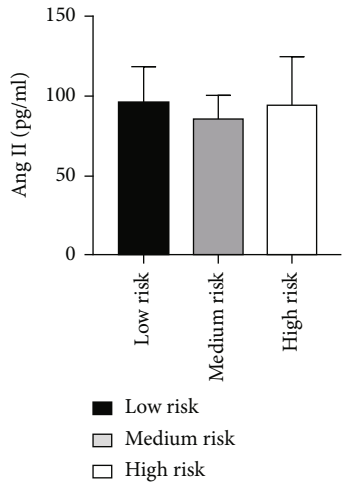

Figure 19: Comparison of Ang II levels among ASO patients with different risk grades.

OR = 1.216, 95% confidence interval (CI): 0.997-1.343, P value = 0.006) and VEGF (partial regression coefficient = 0.059, OR = 1.744, 95% CI: 1.076-1.115, $P = 0.017$) were positively correlated with ASO. These results indicate that Ang II and VEGF could be regarded as risk factors for ASO (Table 11).

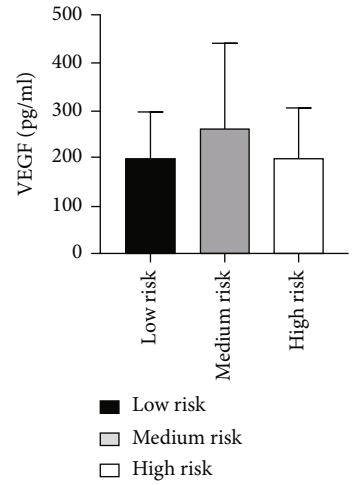

Figure 20: Comparison of VEGF levels in ASO patients with different risk grades.

4.13. Receiver Operating Curve Analysis. The results from this study reveal that the AUC of Ang II and VEGF in diagnosing ASO was 0.764 (good) and 0.854 (very good), respectively, indicating their value as moderate in diagnosing ASO. On other hand, the AUC of the combined diagnosis of Ang II and VEGF was 0.901 (excellent), indicating that the combined diagnosis of Ang II and VEGF has a higher diagnostic value for ASO. Medcalc software was used to compare the AUC of Ang II, VEGF, and their combined diagnosis. We observed a statistically considerable difference between the two groups ($P < 0.05$). Among them, the AUC of Ang II and VEGF combined diagnosis was the highest, followed by VEGF and then Ang II with the lowest value (Tables 12 and 13 and Figure 21).

5. Discussion

Atherosclerosis (AS) is the pathological basis of ASO [5], and its pathogenesis is very complex and involves a variety of theories. Among these, the theory of chronic inflammation plays a crucial role in AS pathogenesis and has received widespread attention in the medical community [7]. As a chronic inflammatory disease, AS has the characteristics of classic inflammatory proliferation, degeneration, and exudation. Previous studies mentioned the occurrence and development of AS to be closely related to chronic inflammatory reactions [28–31]. Ang II can promote inflammatory response by inducing the aggregation of a variety of inflammatory cytokines [32]. High level of angiotensin II is one of the typical features of atherosclerosis patients. A large number of studies have confirmed that angiotensin II can effectively activate the Notch1 signaling pathway in a variety of cells. This study also confirmed the effective activation of Notch1 signaling pathway [33], and the overexpression of Notch1 receptor and ligand can stimulate the accumulated

Table 11: Correlation analysis of Ang II, VEGF, and ASO.

Factor	r	SE	Wald value	P	OR	95% CI
Ang II	0.038	0.068	6.823	0.006	1.216	0.997-1.343
VEGF	0.059	0.015	5.248	0.017	1.744	1.076-1.115

Table 12: Area under ROC curve.

Factor	AUC	SE	P	95% CI
Ang II	0.764	0.065	≤0.001	0.663-0.847
VEGF	0.854	0.039	≤0.001	0.764-0.920
Ang II and VEGF	0.901	0.034	≤0.001	0.835-0.967

Table 13: Comparison of area under ROC curve of each index.

Factor	AUC	SE	Z values	P	95% CI
Ang II vs. VEGF	0.090	0.072	1.257	0.020	0.651-0.859
Ang II vs. Ang II + VEGF	0.137	0.051	2.675	0.007	0.710-0.952
VEGF vs. Ang II + VEGF	0.047	0.027	1.725	0.028	0.820-0.954

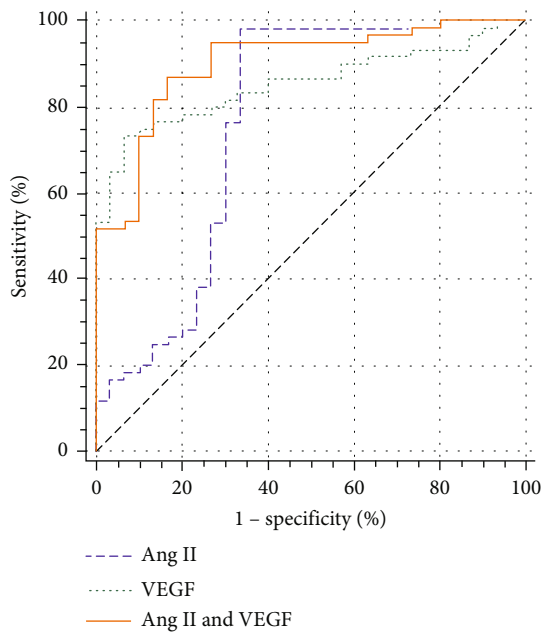

Figure 21: Area under the ROC curve.

Table 14: Main experimental reagent.

The name of the reagent	Source of reagents
Ang II	Shenzhen New Industry Biomedical Engineering Co., Ltd.
VEGF	Beijing Jianping Jinxing Biotechnology Co., Ltd.

Table 15: Main software product information.

The name of the software	Source software
IBMSPAA28.0	IBM company
Medcalc	Beijing Huanzhong Ruechi Technology Co., Ltd.

macrophages to show an M1-type transformation and release a large number of proinflammatory mediators such as IL-1β and TNF-α. Induce and enhance the inflammatory response of the body, and downregulate the Th2 inflammatory cytokines that inhibit the inflammatory response, such as IL-6, to further promote the inflammatory response [34]. Also, as reported in a previous study, intraplaque angiogenesis plays a critical role in developing AS. VEGF is an important proangiogenic factor found to be involved in regulating and inducing angiogenesis among plaques [35]. Dunmore et al. [36] found that VEGF overexpression existed in unstable plaques, and its content was significantly positively correlated with plaque instability, suggesting that the mismatch between VEGF overexpression and other related factors in plaques may be an important reason for the immaturity of new blood vessels. In addition, changes in the structure or function of VSMCs are the main pathological basis of AS [37, 38] where VSMC proliferation is closely linked to AS development. Ang II is a powerful promoter of VSMC phenotype transformation and plays an important role in inducing VSMC proliferation and migration as well as the progression of AS plaque formation [39, 40]. Dong et al. [41] found that Ang II promoted the secretion of endothelin 1 by vascular endothelial cells, which in turn promoted the production of Ang II by vascular endothelial cells, and the two cooperated to promote the proliferation of VSMC. The possible mechanism was that Ang II, as an autocrine growth factor, could directly induce the mRNA expression of c-myc and fos, thus causing the proliferation of VSMC. Wang et al. [42] also found that Ang II could promote abnormal proliferation of VSMC in rats with spontaneous hypertension, and the AT1R blocker captopril could inhibit the proliferation. In addition, studies have found that VEGF and its receptor are closely related to the proliferation of VSMCs [23]. Therefore, Ang II and VEGF can stimulate an inflammatory response, induce angiogenesis in plaques, and participate in VSMC proliferation and migration with the possibility of promoting the occurrence and development of AS. In another study, Zhou et al. [43] found that the effect of Ang II on AS may be independent of its effect on blood pressure, which is basically consistent with the conclusions of relevant animal studies. It was pointed out that Ang II may also be crucially associated with human AS. In recent studies, CRP has been shown to be directly involved in the formation of AS plaques. During an inflammatory reaction of AS tube wall, Peng and coworkers found that Ang II could induce the production of CRP in VSMCs [44]. Recent studies have also confirmed [45] that Ang II can induce the expression of CRP in macrophages through a variety of signaling

pathways, thereby playing a proinflammatory role. Simultaneously, studies have confirmed [20] that if the expression of VEGF and its receptor in AS plaques is significantly increased; then, it indicates new blood vessel formation in AS plaques, depicting a crucial association of VEGF with AS.

In this study, the level of Ang II in ASO patients was considerably higher in comparison to the control group ($P < 0.01$), which indicates an increase in Ang II level being related to ASO. The mechanism for ASO induction on increasing Ang II level may be linked to induction of inflammatory reaction and the stimulation of VSMC proliferation. Ang II can promote inflammatory response by inducing a variety of inflammatory cytokines to aggregate and activate NF-κB [22]. Excessive Ang II secretion stimulates an abnormal proliferation of VSMCs in blood vessels, activates relevant signaling pathways, promotes the abnormal elevation of inflammatory factors such as interleukin-6 (IL-6) and nitric oxide (NO), causes damage to blood vessels, and then promotes the occurrence of AS [46]. The binary logistic regression analysis showed Ang II to be a risk factor for ASO. The AUC of Ang II was 0.764 (good), which indicates that Ang II has a moderate diagnostic value for ASO, with a sensitivity of 98.3% and a specificity of 66.7%. It can also be seen that Ang II is an effective index to evaluate the severity of ASO disease while having a certain reference value for the diagnosis of ASO. Simultaneously, the results of this study reveal that the VEGF level of ASO patients was considerably higher in comparison to the control group ($P < 0.01$), indicating that the increase in VEGF level is related to ASO. The mechanism by which the elevated VEGF level promotes the occurrence of ASO may be related to the induction of angiogenesis in AS plaques and the promotion of inflammatory response [22]. Among them, VEGF and its tyrosine kinase receptor pathway make endothelial cells proliferate and migrate, increase vascular permeability, and participate in regulating and inducing angiogenesis. However, in the initial stage, the increase in VEGF level stimulates the abnormal proliferation of vascular endothelial cells, resulting in immature neovascularization [20]. Studies have shown that immature and pathological neovascularization mostly exists in AS unstable plaques [47]. Binary logistic regression analysis showed that Ang II and VEGF were risk factors for ASO. The AUCs of Ang II and VEGF in the diagnosis of ASO were 0.764 (good) and 0.854 (very good), respectively, indicating their moderate diagnostic value for ASO. They have a certain correlation with the occurrence and development of ASO and also reflect the severity of ASO to a certain extent. The AUC was compared with Medcalc software, and it was found that the AUC of Ang II and VEGF together in the diagnosis of ASO was 0.901 (excellent), which was higher than the AUC of these two indicators alone. This clearly indicates that the combined detection of the two indicators is more valuable in the diagnosis of ASO.

In conclusion, Ang II and VEGF were correlated with the occurrence and development of ASO. At the same time, the AUC analysis demonstrates that Ang II and VEGF were highly discriminative of ASO. However, the limitations of the study, due to time constraints, a small sample size, and only established cases, have been analyzed. Hence, a more rigorous, multicenter, larger sample, double-blind study needs to be designed for further analysis.

Data Availability

The data presented in the study may be made available from the corresponding author upon reasonable request.

Conflicts of Interest

The authors declare no conflicts of interest.

Acknowledgments

This work was supported by a grant from Tai'an Science and Technology Development Fund (2021NS201).

References

[1] K. Zhang, W. Song, D. Li et al., "The association between polymorphism of CARD8 rs2043211 and susceptibility to arteriosclerosis obliterans in Chinese Han male population," *Cellular Physiology and Biochemistry*, vol. 41, no. 1, pp. 173–180, 2017.

[2] H. Yufen, L. Ming, and Z. Lili, *Practical Peripheral Vascular Diseases*, Jincheng Press, Beijing, 1st edition, 2005.

[3] L. M. Wiltz-James and J. Foley, "Hospital discharge teaching for patients with peripheral vascular disease," *Critical Care Nursing Clinics of North America*, vol. 31, no. 1, pp. 91–95, 2019.

[4] B. Zhou, J. She, Y. Wang, and X. Ma, "Venous thrombosis and arteriosclerosis obliterans of lower extremities in a very severe patient with 2019 novel coronavirus disease: a case report," *Journal of Thrombosis and Thrombolysis*, vol. 50, no. 1, pp. 229–232, 2020.

[5] G. K. Hansson, "Inflammation, atherosclerosis, and coronary artery disease," *The New England Journal of Medicine*, vol. 352, no. 16, pp. 1685–1695, 2005.

[6] M. Bäck, A. Yurdagul Jr., I. Tabas, K. Öörni, and P. T. Kovanen, "Inflammation and its resolution in atherosclerosis: mediators and therapeutic opportunities," *Nature Reviews Cardiology*, vol. 16, no. 7, pp. 389–406, 2019.

[7] X. Dai, D. Zhang, C. Wang, Z. Wu, and C. Liang, "The pivotal role of thymus in atherosclerosis mediated by immune and inflammatory response," *International Journal of Medical Sciences*, vol. 15, no. 13, pp. 1555–1563, 2018.

[8] L. Qingquan and D. Xinqing, "Relationship between angiotensin II and coronary heart disease," *Fujian Journal of Medicine*, vol. 34, no. 6, pp. 141-142, 2012.

[9] A. V. Poznyak, D. Bharadwaj, G. Prasad, A. V. Grechko, M. A. Sazonova, and A. N. Orekhov, "Renin-angiotensin system in pathogenesis of atherosclerosis and treatment of CVD," *International Journal of Molecular Sciences*, vol. 22, no. 13, p. 6702, 2021.

[10] X. Xiao, C. Zhang, X. Ma et al., "Angiotensin-(1-7) counteracts angiotensin II-induced dysfunction in cerebral endothelial cells via modulating Nox2/ROS and PI3K/NO pathways," *Experimental Cell Research*, vol. 336, no. 1, pp. 58–65, 2015.

[11] D. Weiss, D. Sorescu, and W. R. Taylor, "Angiotensin II and atherosclerosis," *The American Journal of Cardiology*, vol. 87, no. 8A, pp. 25C–32C, 2001.

[12] G. H. Gibbons, R. E. Pratt, and V. J. Dzau, "Vascular smooth muscle cell hypertrophy vs. hyperplasia. Autocrine transforming growth factor-beta 1 expression determines growth response to angiotensin II," *The Journal of Clinical Investigation*, vol. 90, no. 2, pp. 456–461, 1992.

[13] R. Inatome, S. Yanagi, T. Takano, and H. Yamamura, "A critical role for Syk in endothelial cell proliferation and migration," *Biochemical and Biophysical Research Communications*, vol. 286, no. 1, pp. 195–199, 2001.

[14] C. J. Seow, S. C. Chue, and W. S. Wong, "Piceatannol, a Syk-selective tyrosine kinase inhibitor, attenuated antigen challenge of guinea pig airways in vitro," *European Journal of Pharmacology*, vol. 443, no. 1-3, pp. 189–196, 2002.

[15] N. Ferrara and W. J. Henzel, "Reprint of "Pituitary follicular cells secrete a novel heparin-binding growth factor specific for vascular endothelial cells"," *Biochemical and Biophysical Research Communications*, vol. 425, no. 3, pp. 540–547, 2012.

[16] A. Hoeben, B. Landuyt, M. S. Highley, H. Wildiers, A. T. van Oosterom, and E. A. de Bruijn, "Vascular endothelial growth factor and angiogenesis," *Pharmacological Reviews*, vol. 56, no. 4, pp. 549–580, 2004.

[17] H. Študentová, J. Indráková, P. Petrová et al., "Risk factors of atherosclerosis during systemic therapy targeting vascular endothelial growth factor," *Oncology Letters*, vol. 11, no. 2, pp. 939–944, 2016.

[18] Y. Shimizu, K. Arima, Y. Noguchi et al., "Vascular endothelial growth factor (VEGF) polymorphism rs3025039 and atherosclerosis among older with hypertension," *Scientific Reports*, vol. 12, no. 1, p. 5564, 2022.

[19] L. Figueira and J. C. González, "Effect of resveratrol on seric vascular endothelial growth factor concentrations during atherosclerosis," *Clínica e Investigación en Arteriosclerosis*, vol. 30, no. 5, pp. 209–216, 2018.

[20] J. Pelisek, G. Well, C. Reeps et al., "Neovascularization and angiogenic factors in advanced human carotid artery stenosis," *Circulation Journal*, vol. 76, no. 5, pp. 1274–1282, 2012.

[21] Y. X. Chen, Y. Nakashima, K. Tanaka, S. Shiraishi, K. Nakagawa, and K. Sueishi, "Immunohistochemical expression of vascular endothelial growth factor/vascular permeability factor in atherosclerotic intimas of human coronary arteries," *Arteriosclerosis, Thrombosis, and Vascular Biology*, vol. 19, no. 1, pp. 131–139, 1999.

[22] S. Chao and Z. Yunxiang, "Expression and clinical significance of vascular endothelial cell growth factor and homocysteine in patients with lower extremity arteriosclerosis obliterans," *Medical Theory and Practice*, vol. 35, no. 2, pp. 309–311, 2022.

[23] A. H. Dorafshar, N. Angle, M. Bryer-Ash et al., "Vascular endothelial growth factor inhibits mitogen-induced vascular smooth muscle cell proliferation1, 2," *The Journal of Surgical Research*, vol. 114, no. 2, pp. 179–186, 2003.

[24] Vascular Surgery Group, Surgery Society of Chinese Medical Association, "Guidelines for diagnosis and treatment of arteriosclerosis obliterans of lower extremity," *Chinese Journal of Vascular Surgery (Electronic Edition)*, vol. 7, no. 3, pp. 145–151, 2015.

[25] L. Norgren, W. R. Hiatt, J. A. Dormandy, M. R. Nehler, K. A. Harris, and F. G. R. Fowkes, "Inter-society consensus for the management of peripheral arterial disease (TASC II)," *Journal of Vascular Surgery*, vol. 45, no. 1, pp. S5–67, 2007.

[26] W. Zhankun, *Correlation between lipoprotein phospholipase A2, common femoral artery intima-media thickness and traditional Chinese medicine syndrome type of occlusive arteriosclerosis obliterans*, Shandong University of Chinese Medicine, 2020.

[27] X. Shuai, C. Jianqiu, and L. Yankui, "The value of plasma β2-mg and HCY in the risk classification and prognosis assessment of lower extremity atherosclerosis," *Chinese Journal of General Surgery*, vol. 21, no. 6, pp. 675–681, 2012.

[28] Y. Zhu, X. Xian, Z. Wang et al., "Research progress on the relationship between atherosclerosis and inflammation," *Biomolecules*, vol. 8, no. 3, p. 80, 2018.

[29] X. Zhang, Z. Ren, and Z. Jiang, "EndMT-derived mesenchymal stem cells: a new therapeutic target to atherosclerosis treatment," *Molecular and Cellular Biochemistry*, vol. 2022, pp. 1–11, 2022.

[30] Z. Y. Liang, C. W. Qian, T. H. Lan, Q. H. Zeng, W. H. Lu, and W. Jiang, "Regulatory T cells: a new target of Chinese medicine in treatment of atherosclerosis," *Chinese Journal of Integrative Medicine*, vol. 27, no. 11, pp. 867–873, 2021.

[31] N. Ruparelia and R. Choudhury, "Inflammation and atherosclerosis: what is on the horizon?," *Heart*, vol. 106, no. 1, pp. 80–85, 2020.

[32] X. Zhang, J. Yang, X. Yu, S. Cheng, H. Gan, and Y. Xia, "Angiotensin II-induced early and late inflammatory responses through NOXs and MAPK pathways," *Inflammation*, vol. 40, no. 1, pp. 154–165, 2017.

[33] J. R. Wu, J. L. Yeh, S. F. Liou, Z. K. Dai, B. N. Wu, and J. H. Hsu, "Gamma-secretase inhibitor prevents proliferation and migration of ductus arteriosus smooth muscle cells through the Notch3-HES1/2/5 pathway," *International Journal of Biological Sciences*, vol. 12, no. 9, pp. 1063–1073, 2016.

[34] S. W. Maalouf, C. L. Smith, and J. L. Pate, "Changes in microRNA expression during maturation of the bovine corpus luteum: regulation of luteal cell proliferation and function by microRNA-34a," *Biology of Reproduction*, vol. 94, no. 3, p. 71, 2016.

[35] K. Nakagawa, Y. X. Chen, H. Ishibashi et al., "Angiogenesis and its regulation: roles of vascular endothelial cell growth factor," *Seminars in Thrombosis and Hemostasis*, vol. 26, no. 1, pp. 061–066, 2000.

[36] B. J. Dunmore, M. J. McCarthy, A. R. Naylor, and N. P. J. Brindle, "Carotid plaque instability and ischemic symptoms are linked to immaturity of microvessels within plaques," *Journal of Vascular Surgery*, vol. 45, no. 1, pp. 155–159, 2007.

[37] A. Frismantiene, M. Philippova, P. Erne, and T. J. Resink, "Smooth muscle cell-driven vascular diseases and molecular mechanisms of VSMC plasticity," *Cellular Signalling*, vol. 52, pp. 48–64, 2018.

[38] Y. Chen, L. Liang, C. Wu et al., "Epigenetic control of vascular smooth muscle cell function in atherosclerosis: a role for DNA methylation," *DNA and Cell Biology*, vol. 41, no. 9, pp. 824–837, 2022.

[39] N. Shi and S. Y. Chen, "Mechanisms simultaneously regulate smooth muscle proliferation and differentiation," *Journal of Biomedical Research*, vol. 28, no. 1, pp. 40–46, 2014.

[40] E. R. Pfaltzgraff and D. M. Bader, "Heterogeneity in vascular smooth muscle cell embryonic origin in relation to adult structure, physiology, and disease," *Developmental Dynamics*, vol. 244, no. 3, pp. 410–416, 2015.

[41] D. Xiaoyan, Z. Guiqing, X. Mingming et al., "Effect of Captopril on endothelin and angiotensin ? in rabbits with atherosclerosis and its correlation with proto-oncogenes c-myc and c-fos," *Chinese Journal of Arteriosclerosis*, vol. 3, pp. 217–220, 2002.

[42] W. Xiangyu, W. Jiaobao, J. Xueqing, W. Huajun, and X. Changsheng, "Relationship between abnormal proliferation of aortic smooth muscle cells and endogenous renin-angiotensin system in spontaneously hypertensive rats," *Chinese Journal of Arteriosclerosis*, vol. 3, pp. 212–216, 1997.

[43] Z. Jingxiong, H. Chunling, C. Xiaoyu et al., "Association between angiotensin ? and atherosclerosis in type 2 diabetes mellitus," *Chinese Journal of Gerontology*, vol. 34, no. 24, pp. 6905–6907, 2014.

[44] N. Peng, J. T. Liu, D. F. Gao, R. Lin, and R. Li, "Angiotensin II-induced C-reactive protein generation: inflammatory role of vascular smooth muscle cells in atherosclerosis," *Atherosclerosis*, vol. 193, no. 2, pp. 292–298, 2007.

[45] M. Li, J. Liu, C. Han, B. Wang, X. Pang, and J. Mao, "Angiotensin II induces the expression of c-reactive protein via MAPK-dependent signal pathway in U937 macrophages," *Cellular Physiology and Biochemistry*, vol. 27, no. 1, pp. 63–70, 2011.

[46] L. Dongdong, L. Shaokui, G. Xinyu, W. Xiaomei, and W. Cuirong, "Resveratrol inhibits angiotensin ?/TLR4/NF-KB in regulating inflammation and oxidative stress injury of rat vascular smooth muscle cells," *Chinese Journal of Evidence-based Cardiovascular Medicine*, vol. 11, no. 12, pp. 1461–1467, 2019.

[47] C. Yiyao, *Study on the pathology, morphology and related cellular mechanism of carotid atherosclerotic plaque*, Peking Union Medical College, 2019.

Hindawi
Disease Markers
Volume 2022, Article ID 4259067, 14 pages
https://doi.org/10.1155/2022/4259067

Research Article

Analysis of Cytokine Levels in Meibum and Clinical Correlations with Meibomian Gland Dysfunction

Wenting Liu,[1,2,3] **Tong Lin**,[1,2] **and Lan Gong**[1,2]

[1]*Department of Ophthalmology and Vision Science, The Eye, Ear, Nose and Throat Hospital of Fudan University, Shanghai 200031, China*
[2]*NHC Key Laboratory of Myopia, Laboratory of Myopia, Chinese Academy of Medical Sciences, Fudan University, Shanghai 200031, China*
[3]*Department of Ophthalmology, Huadong Hospital of Fudan University, Shanghai, China*

Correspondence should be addressed to Lan Gong; 13501798683@139.com

Wenting Liu and Tong Lin contributed equally to this work.

Received 1 July 2022; Revised 3 September 2022; Accepted 11 October 2022; Published 23 November 2022

Academic Editor: Qi-Chen Yang

Objectives. This study is aimed at investigating the difference of meibum chemokines in MGD subjects with different degrees of MGD and the correlations of meibum chemokines with ocular surface parameters. *Methods*. Twenty MGD subjects (MQ score > 8) and twenty MGD subjects (MQ score ≤ 8) were enrolled to examine ocular surface parameters, including meibomian gland function (MGE, MQ meibograde, and lid margin), tear stability (NIKBUT, FBUT, and LLT), tear secretion (SIT and TMH), OSDI questionnaire, and CFS. These subjects also obtained meibum samples, and then meibum chemokines (MIG, IFN-γ, IL-8, IP-10, and MCP-1) were examined and analyzed the correlations with ocular surface parameters. *Results*. MIG, IP-10, and MCP-1 were found clearly elevated in MGD subjects with higher MQ score than that in MGD subjects with low MQ score (MIG: $p = 0.038$, IP-10: $p = 0.019$, MCP-1: $p = 0.040$). The meibomian function was found mostly positively correlated with level of MIG (MGE: $r = 0.600$, $p < 0.001$; MQ: $r = 0.579$, $p < 0.001$) and IP-10 (MGE: $r = 0.719$, $p < 0.001$; MQ: $r = 0.601$, $p < 0.001$). The tear stability was found negatively correlated with the level of MIG (NIKBUT: $r = -0.438$, $p = 0.005$; LLT: $r = -0.464$, $p = 0.003$) and MCP-1 (NIKBUT: $r = -0.425$, $p = 0.006$; LLT: $r = -0.761$, $p < 0.001$). The OSDI was positively correlated with IL-8, IFN-γ, and MIG. *Conclusion*. Chemokines in meibum were significantly evaluated in MGD subjects suffering from severe meibomian gland quality. These findings indicate that chemokines play roles in the pathogenesis of MGD, and molecules targeted by chemokines may develop as novel agents for MGD therapy, perhaps through inhibiting inflammation in meibomian glands and microvascular in the eyelid margin.

1. Introduction

Meibomian gland dysfunction (MGD), a chronic abnormality of the meibomian glands, remarkably affects tear film stability and leads to various ocular surface disease problems [1]. The global prevalence of MGD was reported to range from 10 to 20%, while the prevalence of MGD in the Eastern Asian even achieved more than 50% [2]. In ophthalmology clinics, MGD is one of the most common disorders routinely, so it can be considered as a public health problem [3]. Normal meibomian glands can secrete clear oil meibum, which serve as a mixture of lipids via orifices as the outermost layer of the tear film [4]. The abnormal meibum which MGD patients produce becomes more stagnant than the normal meibum, which can lead to terminal meibomian gland duct obstruction and evaporative dry eye [1]. Although there are different pathogenic mechanisms responsible for DED owing to MGD, a common consensus is that the involvement of inflammation as an integral part of MGD and DED [5]. The malfunction of the meibomian gland leads to exacerbating of the

meibum, and abnormal meibum further derangements of the ocular surface and triggers more inflammatory cytokine expression [6]. The vicious circle, named as "dry eye inflammatory vicious cycle", forms between dry eye and inflammation [7], and abundant evidences identified that chronic inflammation on the ocular surface is located at the core pathogenesis of MGD [8].

In the DEWS II report, the etiology of MGD was described to be terminal duct obstruction impairing ocular surface homeostasis and leading to apparent inflammation and tear hyperosmolarity [9, 10]. Inflammation is an extremely complex process, and the chemotaxis process is a pivotal step in the promotion and regulation of the inflammatory response. Chemokine family, the most important factors among the chemotaxis process, is a group of low molecular weight proteins (between 8 and12 kDa) which can promote immune cell migration to act on the immune chemotaxis effect [11]. There are two large chemokine families, the C-X-C motif ligand (CXCL) and the C-C motif ligand (CCL) chemokine families, both of which can induce T cell infiltration and regulate autoimmune inflammation [12]. Once these chemokines are bound to the ligands, they can lead to tissue damage and clinical manifestations through polarizing the migration of specific immune cells and amplifying the inflammatory response.

Manuscripts focusing on tear inflammation in MGD are steadily increasing [13, 14], but there are rare reports concentrating on meibum chemokine examination in MGD patients. Considering that the core pathogenesis of MGD is located in the meibum secreted by the meibomian gland [1, 6], directly study on the inflammation cytokines in meibum has more explicit clinical value than inflammation cytokines in tears. The aim of the current study was to investigate the levels of different chemokines in meibum in MGD subjects. Furthermore, the correlations between meibum chemokines with ocular surface parameters were analyzed to seek possible meibum biomarkers for potential therapeutic agents in MGD.

2. Materials and Methods

2.1. Participants. This study was conducted in accordance with the tenets of the Declaration of Helsinki and was approved by the Institutional Review Board (IRB) of the Eye, Ear, Nose, and Throat (EENT) Hospital of Fudan University. The clinical trial was registered in the Chinese Clinical Trial Registry on June 2019. The registration number is ChiCTR-1900023732. Forty patients who experienced MGD were recruited from the EENT hospital from September 2019 to February 2020. According to the consensus of The International Workshop on Meibomian Gland Dysfunction, MGD was confirmed by meibomian gland function examination by the same ophthalmology [1, 15].

The inclusion criteria for MGD based on DEWS II are as follows: OSDI score > 12.5 points, FBUT < 10 s, and the presence of lid margin abnormalities, orifice abnormalities, and meibum abnormalities [1, 15]. These MGD patients aged above 18 years old, who voluntarily participated in the experiment. Subjects with immune related dry eye such as Sjogren's syndrome were excluded. Furthermore, subjects with certain ocular diseases (acute ocular inflammation, obvious scar or keratinization in the palpebral margin) or receiving physiotherapy for blepharitis (intense pulsed light, baby shampoo, and demodex blepharitis treatment) in the last 3 months may confound the study results; thus, they were excluded from the study. Subjects were also excluded if they had a related ocular surgery, including cataract surgery, trichiasis surgery, lachrymal duct obstruction, or refractive surgery in the past 3 months. After the procedure and potential consequences of the study were explained elaborately, informed consent was obtained from all subjects before the experiment.

Firstly, OSDI questionnaire was collected to evaluate the symptoms of MGD subjects. Subsequently, ocular parameters including tear meniscus height (TMH), noninvasive tear break-up time (NIKBUT), lipid layer thickness (LLT), incomplete blink rate (%), fluorescein tear film break-up time (FBUT), corneal fluorescein staining (CFS), Schirmer I test (SIT), meibomian gland expressibility (MGE), meibomian gland quality (MQ), lid margin, and meibograde. Finally, the meibum sample was collected and stored for further examination. Based on MQ examination, subjects with mild to severe abnormal meibum quality (ranging from cloudy with granular particulates to toothpaste-like particulates) were included into the MQ > 8 group, while subjects with slight abnormal meibum quality (ranging from clear oil to cloudy oil) were included into MQ ≤ 8 group.

2.2. Ocular Surface Parameters and OSDI

2.2.1. OSDI. The OSDI questionnaire, containing a 12-item questionnaire with a scale of 0-100, has been designed to rapidly evaluate different ocular discomfort symptoms (soreness, light sensitiveness, and blurred vision). The OSDI questionnaire provides a rapid assessment of vision-related dyspraxia (difficulty reading, driving, operating a computer, and watching TV). There is a positive correlation between OSDI scores and the severity of ocular discomfort, with higher scores representing greater ocular discomfort [16].

2.2.2. TMH and NIKBUT. TMH and NIKBUT were measured by an OCULUS Keratograph 5M (Wetzlar, Germany) equipped with modified TF-scan software. The procedure was repeated three times following the instructions of OCULUS Keratograph 5M by the same ophthalmology in a dark room. TMH was manually gauged at the central point of the lower lid margin on the images. Then, all participants were required to naturally blink twice, and then keep their eyes open as much time as possible until the next blink, the duration is defined as NIKBUT [17].

2.2.3. LLT and Incomplete Blink Rate. LLT and incomplete blink rate were detected noninvasively by the LipiView® instrument (TearScience, Morrisville, NC, United States). All participants were instructed to blink naturally to record a 15 s video of the tear film interference pattern and analyze the LLT incomplete blink rate (%). The procedure was repeated twice times for each eye.

2.2.4. FBUT. A fluorescein strip (Jingming) moistened with preservative-free saline gently touched the central lower lid

margin. After participants blinked several times to ensure adequate coating of the complete cornea, they were required to rapidly open the eyes, and this point was recorded as the starting point (time = 0 sec). FBUT was defined as the interval between the starting point and the first black spot appearing in the stained team film with a cobalt blue filter and slit lamp microscope. The test was repeated three times and the average FBUT was calculated [16].

2.2.5. CFS. The steps of corneal staining were similar to those for the assessment of the FBUT. The whole cornea was divided into five zones (central, superior, temporal, nasal, and inferior). Corneal epithelial injury was graded on a scale from 0 to 3: 0 if no epithelial injury; 1, <30 if corneal punctate stain; 2, >30 if corneal punctate stain but not fusion; and 3, if fusion of corneal staining or ulcer. The total CFS score ranged from 0 to 15.

2.2.6. SIT. A sterile dry strip (Jingming®) was inserted into the lateral canthus of the lower eyelid away from the cornea for 5 min. The wetted length of the strip absorbed with tears was recorded as sitting to assess tear secretion. Potential SIT range is from 0 to 30 mm.

2.2.7. Meibomian Gland Function. Meibomian gland function was evaluated using MGE score, MQ score, and lid margin score. The assessments were produced under slit lamp to grade MGE score, MQ score, and lid margin score. Five glands of the middle third of the upper lid were digitally pressed by MG evaluator (MGE-1000; TearScience), and the MGE was graded as 0-3: grade 0 if all five glands are expressible; grade 1, if 3-4 glands are expressible; grade 2, if 1-2 glands are expressible; and grade 3, if no glands are expressible [18]. Based on the phases of meibum, MQ was graded as follows: grade 0 if clear, grade 1 if cloudy, grade 2 if cloudy with granular particulates, and grade 3 if thick, like toothpaste-like particulates. Each of the eight glands of the lower eyelid was graded on a scale from 0 to 3. The scores of the eight glands were summarized (range: 0–24) [19]. According to the anomalous of the lid margin, lid margin score was graded as 0-4: grade 0 if absent of abnormal, and if present for any of the following parameters is recorded as 1: plugged meibomian gland orifices, vascular congestion, irregularity of the lid margin, and partly expression of the mucocutaneous borderline [20]. Combined with the upper and lower eyelid margins, the total score ranges from 0 to 8.

2.2.8. Meibograde. Meibographies of the upper and lower eyelids were captured by the OCULUS Keratograph 5M (Wetzlar, Germany), and the meibomian gland dropout rate was analyzed qualitatively by ImageJ software (National Institutes of Health, USA). Meibograde of each eyelid was scored based on the meibomian gland dropout rate: 0 if meibomian gland area of loss = 0%, 1 if dropout rate less than 1/3 of the meibomian gland, 2 if dropout rate ranges from 1/3 to 2/3 of the meibomian gland, and 3 if dropout rate was over 2/3 of the meibomian gland. Meibogrades of the upper and lower eyelid were summed to a grade as 0-6 for each eye [21].

2.3. Meibum Inflammation Cytokines

2.3.1. Meibum Samples Collection. A disposable 2.2 μL collector (Seinda, Guangdong, China) was applied to obtain meibum samples at the orifice of the central meibomian glands of the upper and lower eyelid margin with meibomian massage simultaneously. The meibum samples were transferred into little microtubes immediately and then stored at -80°C for further assays.

2.3.2. Assays for Inflammation Cytokines. MILLIPLEX MAP High Sensitivity T Cell Magnetic Bead Panel (Merck EMD Millipore, Billerica, MA, United States) for monokine induced by IFN-γ (MIG), interferon-gamma (IFN-γ), interleukin (IL)-8, interferon-inducible protein-10 (IP-10), and monocyte chemotactic protein-1 (MCP-1) was used according to the manufacturer's instructions. Luminex liquid suspension chip detection was performed using Huaying Biotechnologies (Shanghai, China). Briefly, meibum samples were incubated in microbead-embedded 96-well plates overnight at 4°C and subsequently incubated with the detection antibody for 1 h at room temperature at the next day. Next, Streptavidin-Phycoerythrin was added into each well of the plate and incubated for 30 min at room temperature, and the values were detected by a Luminex 200 system (Luminex Corporation, Austin, TX, United States).

2.4. Statistical Analyses. Data were analyzed using SPSS v.17.0 software (SPSS Inc.). Categorical data between the two groups were evaluated for statistical significance using the chi-square test. Continuous variables were presented as the mean ± standard deviation. The normal distribution test was performed to check whether the numerical variables were normally distributed. To compare the ocular parameters and levels of chemokine concentration, an independent sample t-test was used. The correlations between the ocular parameters and levels of chemokine concentration were performed using the Pearson rank correlation test. The results are indicated as p values, where $p < 0.05$ was considered to indicate a statistically significant difference.

3. Results

3.1. Demographic Data and Clinical Characteristics. Twenty MGD subjects whose MQ scores were above 8 with a mean age of 35.30 ± 9.71 years (14 females, 6 males) were enrolled and compared with twenty MGD subjects whose MQ scores were less than 8 (mean age: 34.35 ± 5.76 years; 13 females, 7 males). No significant differences in terms of sex ($c2 = 0.109$, $p = 0.744$) and age ($p = 0.709$) were found between the two groups. The demographic data and ocular surface parameters in MGD subjects with MQ > 8 and MGD with MQ ≤ 8 were listed in Table 1.

The meibomian gland function was comprehensively evaluated by MGE, MQ, meibograde, and lid margin. By comparing the meibomian gland function-related markers, subjects with more MQ scores showed more severe clinical manifestations than subjects with low MQ score (MGE: $^{***}p < 0.001$, MQ: $^{***}p < 0.001$, meibograde: $^{***}p < 0.001$, lid margin: $^{***}p < 0.001$; Table 1). NIKBUT, FBUT, and

Table 1: Demographic data and clinical characteristics of MQ > 8 and MQ ≤ 8. (Mean ± SD).

	MQ > 8 ($n = 20$)	MQ ≤ 8 ($n = 20$)	p value
Age (years)	35.30 ± 9.71	34.35 ± 5.76	0.709
F/M	14/6	13/7	0.744
MGE score	1.50 ± 0.51	0.75 ± 0.72	**<0.001**
MQ score	16.80 ± 3.14	5.80 ± 2.59	**<0.001**
Meibograde score	4.00 ± 1.45	1.75 ± 0.55	**<0.001**
Lid margin score	1.90 ± 0.64	0.65 ± 0.67	**<0.001**
NIKBUT (s)	5.657 ± 0.96	6.982 ± 1.20	**<0.001**
FBUT(s)	4.725 ± 0.98	5.875 ± 0.83	**<0.001**
LLT (nm)	57.05 ± 9.29	64.90 ± 7.77	**0.006**
CFS score	1.10 ± 1.17	0.90 ± 0.97	0.558
OSDI score	45.09 ± 15.92	34.63 ± 13.70	**0.032**
SIT (mm/5 minutes)	12.50 ± 3.98	10.15 ± 4.44	0.086
TMH (mm)	0.211 ± 0.05	0.181 ± 0.03	**0.029**
Incomplete blink rate (%)	51.50 ± 22.31	44.50 ± 22.12	0.325

MGE: meibomian gland expressibility; MQ: meibomian gland quality; NIKBUT: noninvasive keratograph, tear film break-up time; FBUT: fluorescein break-up time; LLT: lipid layer thickness; OSDI: Ocular Surface Disease Index; SIT: Schirmer TMH, tear meniscus height; CFS: fluorescein staining score. Significant differences between MQ > 8 and MQ ≤ 8 values. The bold values mean significant results. $^{*}p < 0.05$, $^{**}p < 0.01$, $^{***}p < 0.001$.

LLT are the major indexes of tear film stability. The values of the NIKBUT, FBUT, and LLT in MGD subjects with high MQ scores were significantly lower than those in MGD subjects with low MQ score (NIKBUT: $^{***}p < 0.001$, FBUT: $^{***}p < 0.001$, LLT: $^{**}p = 0.006$; Table 1). The OSDI score in MQ > 8 subjects was mildly higher than that in subjects MQ ≤ 8 ($^{*}p = 0.032$). Tear secretion was assessed by SIT and TMH, and we found TMH and SIT was slightly higher in MQ > 8 subjects than that in subjects MQ ≤ 8. TMH showed a significant difference between the two group subjects ($^{*}p = 0.029$), while no significant difference in SIT was found ($^{*}p = 0.086$). The CFS and incomplete blink rate showed no significant differences between MGD subjects with high MQ scores and with low MQ scores.

3.2. Meibum Inflammation Cytokines. Five inflammatory cytokines (MIG, IFN-γ, IL-8, IP-10, and MCP-1) were examined and analyzed in meibum samples in both group subjects. Based on inflammatory cytokines results, MIG, IP-10, and MCP-1 were found clearly elevated in MGD subjects with high MQ score than that in MGD subjects with low MQ score (MIG: $^{*}p = 0.038$, IP-10: $^{*}p = 0.019$, MCP-1: $^{*}p = 0.040$; Table 2). No significant differences of IFN-γ and IL-8 levels were found in meibum inflammation cytokines between the two group subjects (IFN-γ: $p = 0.095$, IL-8: $p = 0.173$; Table 2).

3.3. The Correlation between Meibum Cytokines and Ocular Surface Parameters. The meibum cytokines were identified to be significantly affecting meibomian gland function and tear film stability (Figure 1). The MGE was found positively correlated with the level of MIG ($r = 0.600$, $^{***}p < 0.001$), IL-8 ($r = 0.465$, $^{**}p = 0.002$), and IP-10 ($r = 0.719$, $^{***}p < 0.001$) (Figure 1(a)). The MQ was found positively correlated with the level of MIG ($r = 0.579$, $^{***}p < 0.001$), IFN-γ ($r = 0.321$, $^{*}p = 0.044$), IL-8 ($r = 0.444$, $^{**}p = 0.004$), and IP-10 ($r = 0.601$, $^{***}p < 0.001$) (Figure 1(b)). The lid margin was found positively correlated with the level of MIG ($r = 0.471$, $^{**}p = 0.002$), IP-10 ($r = 0.569$, $^{***}p < 0.001$), and MCP-1 ($r = 0.496$, $^{***}p < 0.001$) (Figure 1(c)). The meibograde was found positively correlated with the level of MIG ($r = 0.471$, $^{**}p = 0.002$), IFN-γ ($r = 0.489$, $^{**}p = 0.001$), IP-10 ($r = 0.325$, $^{*}p = 0.041$), and MCP-1 ($r = 0.520$, $^{**}p = 0.001$) (Figure 1(d)).

Moreover, meibum chemokines seriously affected the stability of the tear film. The NIKBUT was found negatively correlated with the level of MIG ($r = -0.438$, $^{**}p = 0.005$), IL-8 ($r = -0.339$, $^{*}p = 0.032$), and MCP-1 ($r = -0.425$, $^{**}p = 0.006$) (Figure 1(e)). All five cytokines were found negatively correlated with FBUT (MIG: $r = -0.590$, $^{***}p < 0.001$, IFN-γ: $r = -0.399$, $^{*}p = 0.011$, IL-8: $r = -0.421$, $^{**}p = 0.007$, IP-10: $r = -0.388$, $^{*}p = 0.013$, and MCP-1: r = -0.394, $^{*}p = 0.012$) (Figure 1(f)). The LLT was found negatively correlated with the level of MIG ($r = -0.464$, $^{**}p = 0.003$), IFN-γ ($r = -0.463$, $^{**}p = 0.003$), and MCP-1 ($r = -0.716$, $^{***}p < 0.001$) (Figure 1(g)). However, no significant correlation was found between CFS and five meibum cytokines.

In tear secretion and OSDI, the concentrations of meibum cytokines were also found partially correlated with these parameters. The OSDI was positively correlated with the level of MIG ($r = 0.561$, $^{***}p < 0.001$), IFN-γ ($r = 0.321$, $^{*}p = 0.043$), and IL-8 ($r = 0.641$, $^{***}p < 0.001$) (Figure 1(i)). MIG was positively correlated with TMH ($r = 0.324$, $^{*}p = 0.041$; Figure 1(j)), while no significant correlation was found between SIT and five meibum cytokines (Figure 1(k)).

Table 2: Comparison of meibum inflammation cytokines between MQ > 8 and MQ ≤ 8 (Mean ± SD).

	MQ > 8 ($n = 20$)	MQ ≤ 8 ($n = 20$)	p value
MIG (pg/mL)	768.40 ± 376.92	550.35 ± 251.40	**0.038**
IFN-γ (pg/mL)	150.46 ± 31.43	136.33 ± 19.43	0.095
IL-8 (pg/mL)	135.48 ± 50.17	112.97 ± 52.30	0.173
IP-10 (pg/mL)	2472.16 ± 356.81	2159.75 ± 446.96	**0.019**
MCP-1 (pg/mL)	101.82 ± 41.33	73.27 ± 43.74	**0.040**

MIG: monokine induced by IFN-γ; IFN-γ: interferon-gamma, IL-8: interleukin (IL)-8; IP-10: interferon-inducible protein-10; and MCP-1: monocyte chemotactic protein-1. Significant differences in inflammation cytokines between MQ > 8 and MQ ≤ 8 values. The bold values mean significant results. $^{*}p < 0.05$, $^{**}p < 0.01$, $^{***}p < 0.001$.

4. Discussion

MGD is a chronic disease with a high level of prevalence among the human population and creates long-term damage to the ocular surface [3]. In consideration of the importance of inflammation in MGD, exploration and identification of

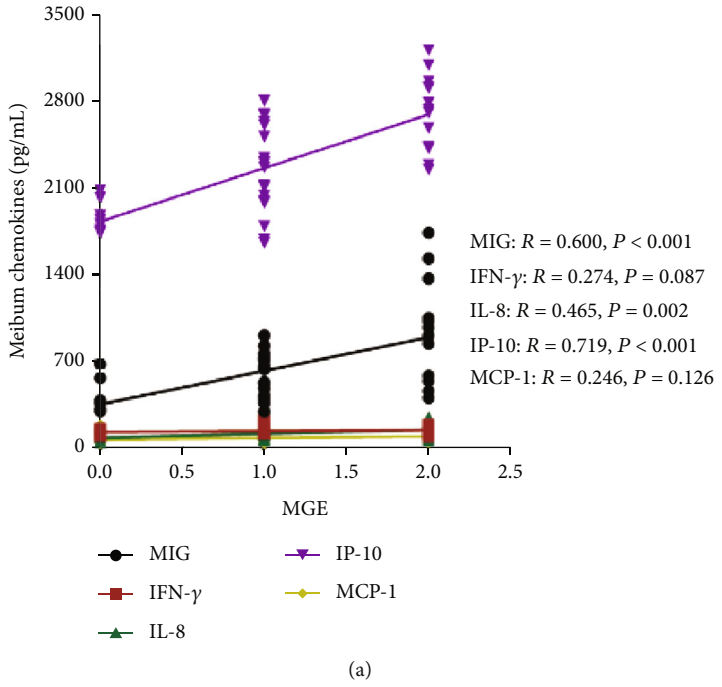

(a)

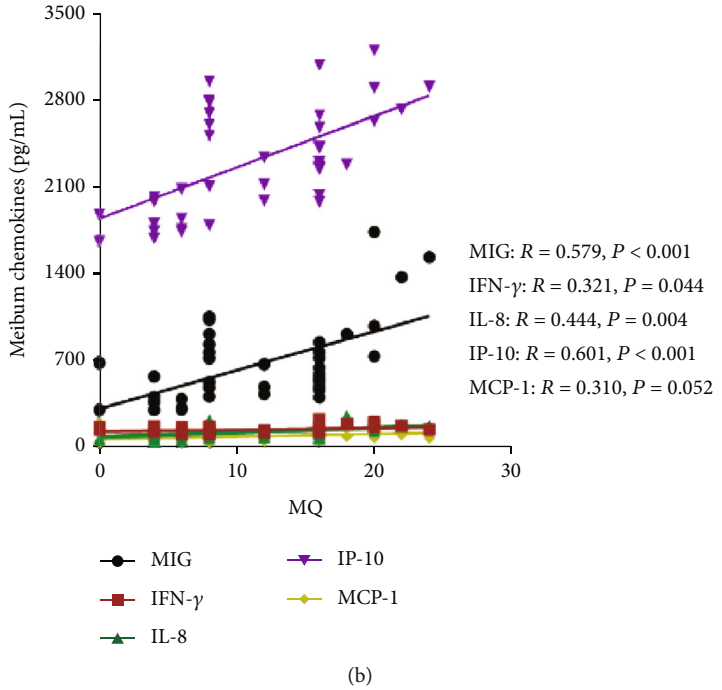

(b)

Figure 1: Continued.

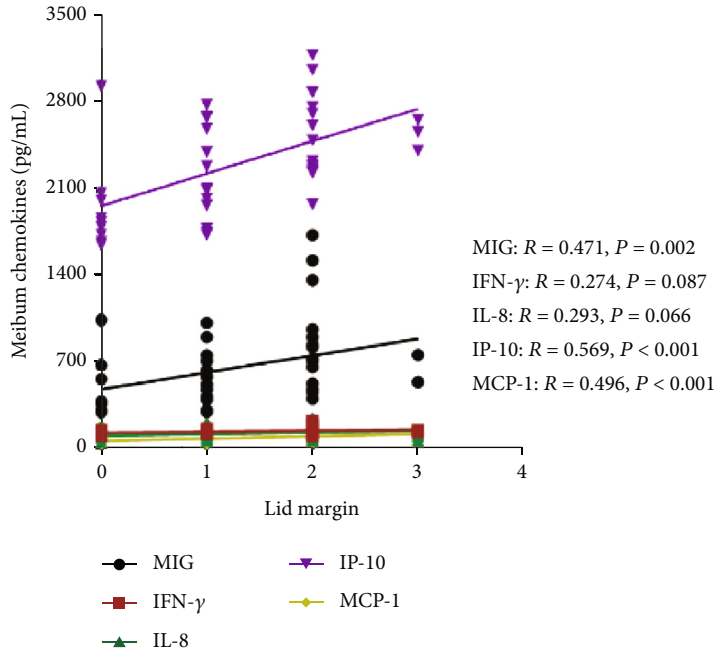

(c)

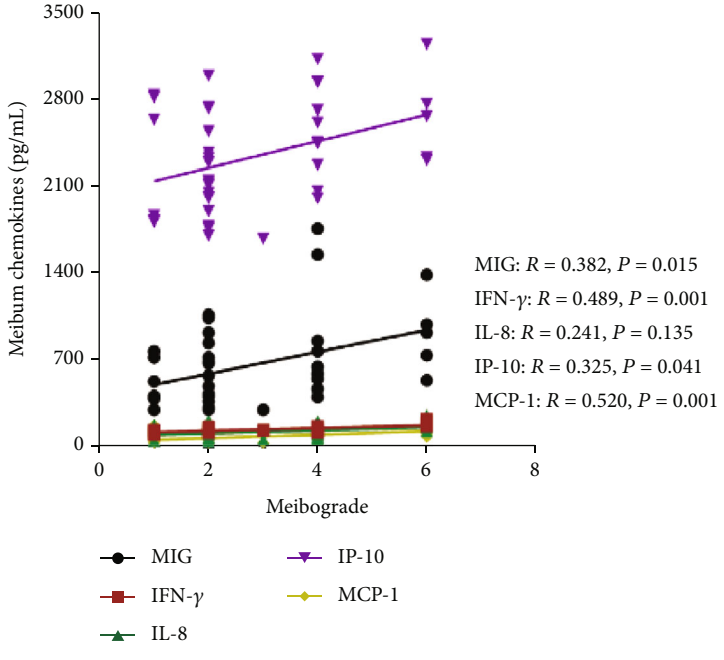

(d)

Figure 1: Continued.

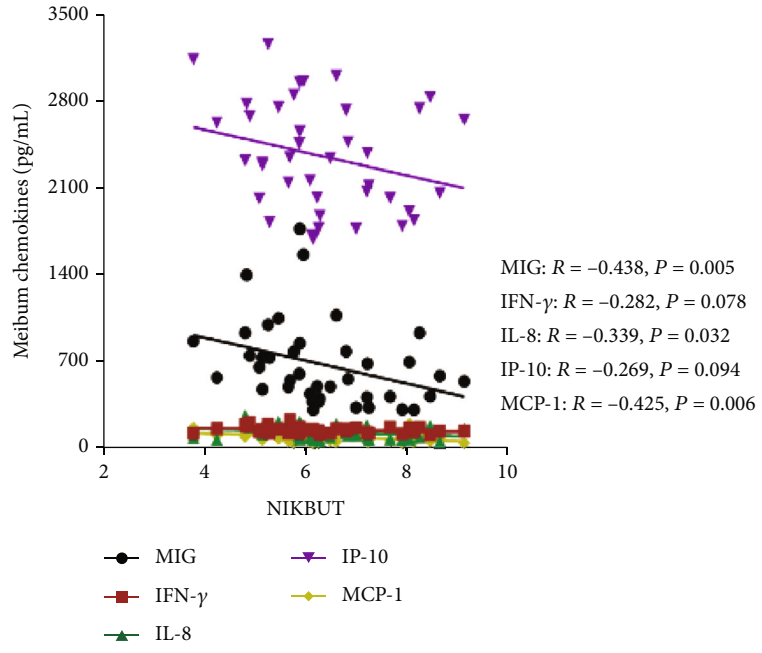

(e)

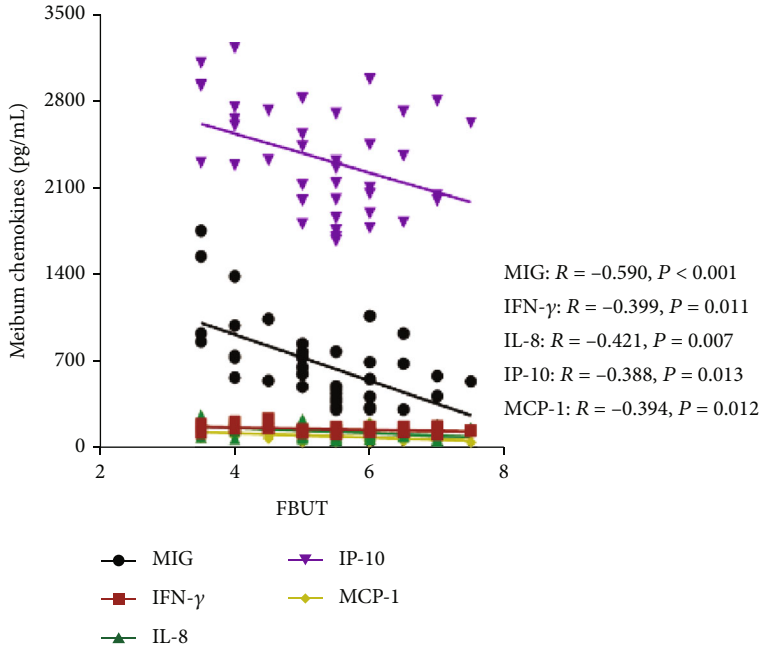

(f)

Figure 1: Continued.

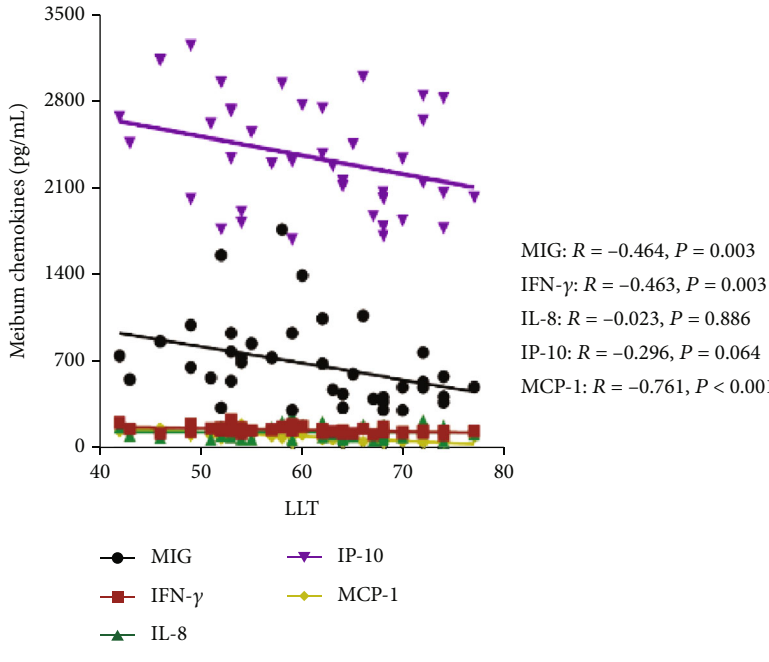

(g)

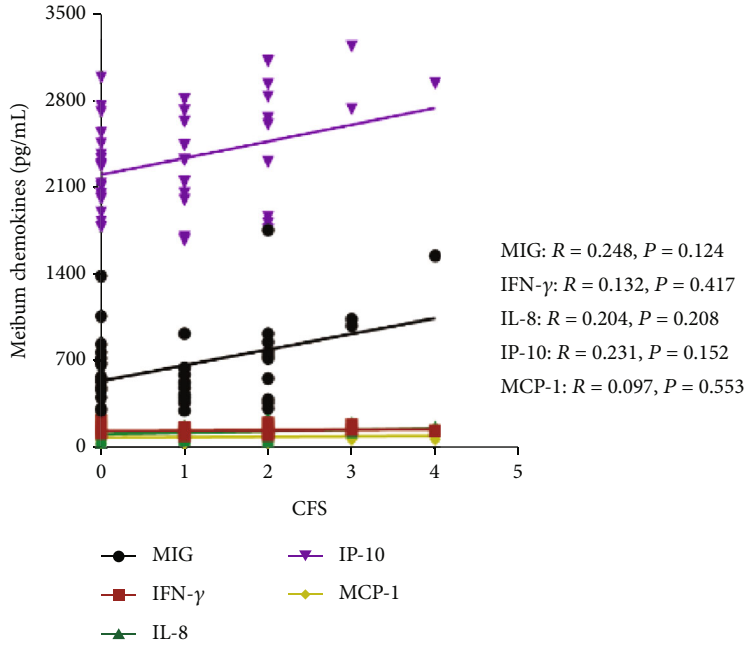

(h)

Figure 1: Continued.

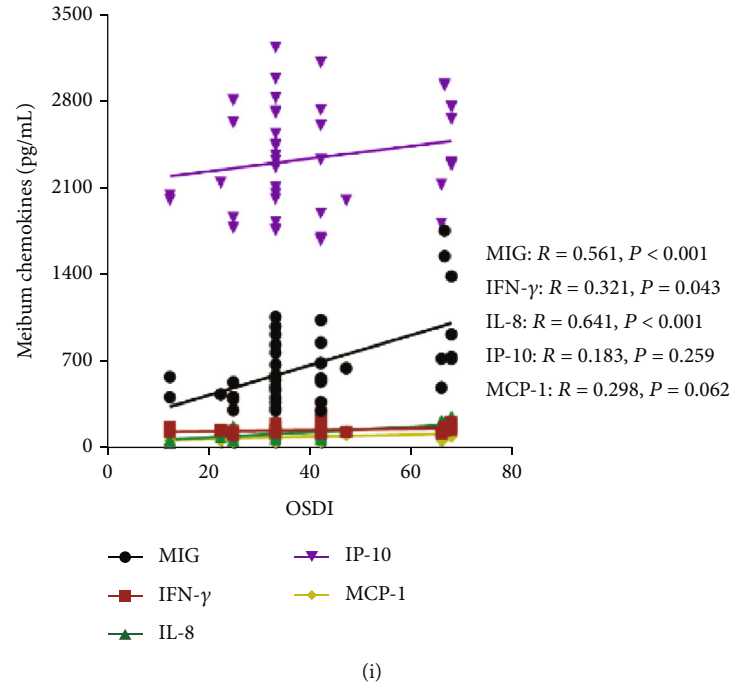

(i)

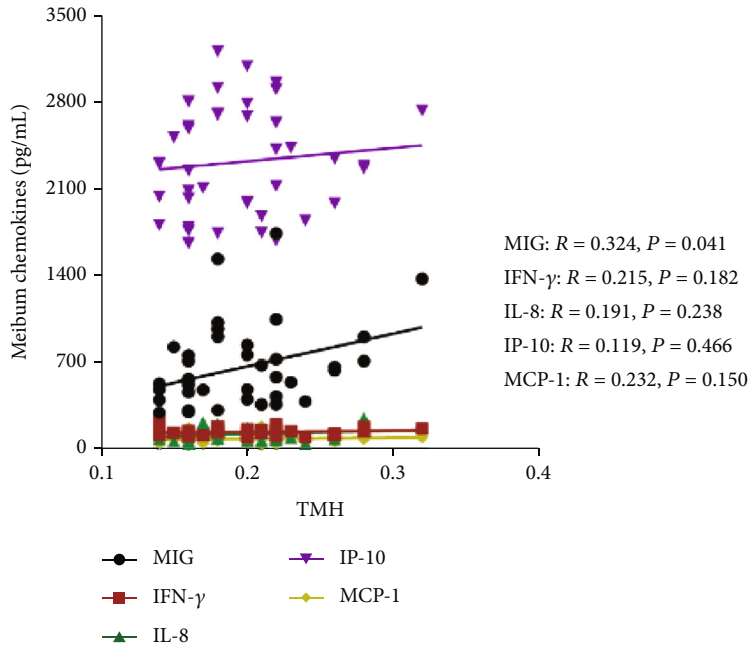

(j)

Figure 1: Continued.

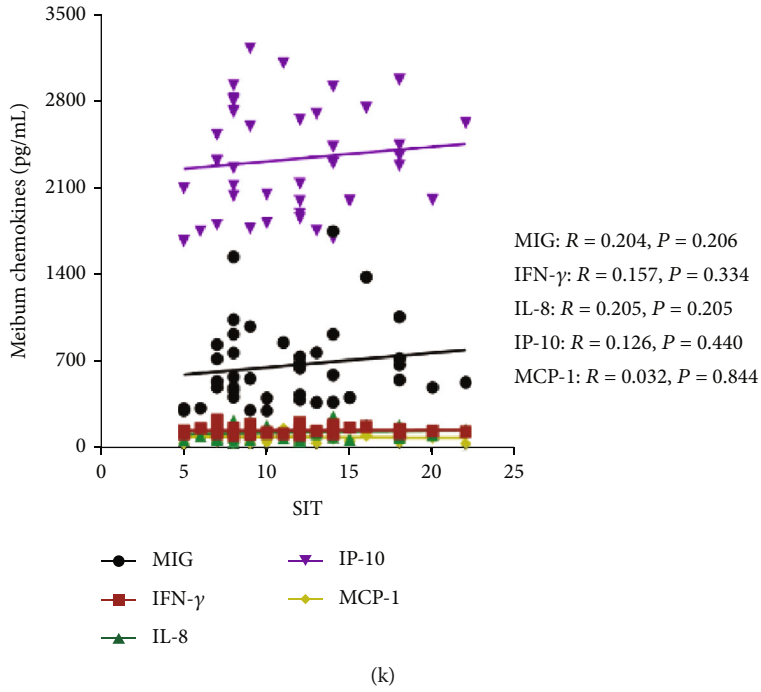

(k)

Figure 1: Correlation between ocular surface parameters and meibum inflammatory cytokines. (a) MGE score. The level of MIG ($r = 0.600$, $^{*}p = 0.015$), IL-8 ($r = 0.465$, $^{**}p = 0.002$), and IP-10 ($r = 0.719$, $^{***}p < 0.001$) is positively correlated with the MGE score. No significant correlations were found between MGE and other inflammatory cytokines (all $p > 0.05$). (b) MQ score. The level of MIG ($r = 0.579$, $^{***}p < 0.001$), IFN-γ ($r = 0.321$, $^{*}p = 0.044$), IL-8 (r = 0.444, $^{**}p = 0.004$), and IP-10 ($r = 0.601$, $^{***}p < 0.001$) is positively correlated with the MQ score. No significant correlations were found between MQ and MCP-1 ($p > 0.05$). (c) Lid margin score. The level of MIG ($r = 0.471$, $^{**}p = 0.002$), IP-10 ($r = 0.569$, $^{***}p < 0.001$), and MCP-1 ($r = 0.469$, $^{***}p < 0.001$) is positively correlated with the lid margin score. No significant correlations were found between lid margin and other inflammatory cytokines (all $p > 0.05$). (d) Meibograde score. The level of MIG ($r = 0.382$, $^{*}p = 0.015$), IFN-γ ($r = 0.489$, $^{**}p = 0.001$), and MCP-1 ($r = 0.520$, $^{**}p = 0.001$) is positively correlated with the meibograde score. No significant correlations were found between meibograde score and other inflammatory cytokines (all $p > 0.05$). (e) NIKBUT. The level of MIG ($r = -0.438$, $^{**}p = 0.005$), IL-8 ($r = -0.339$, $^{*}p = 0.032$), and MCP-1 ($r = -0.425$, $^{**}p = 0.008$) is negatively correlated with the NIKBUT. No significant correlations were found between NIKBUT and other inflammatory cytokine (all $p > 0.05$). (f) FBUT. The level of MIG ($r = -0.590$, $^{***}p < 0.001$), IFN-γ ($r = -0.399$, $^{*}p = 0.011$), IL-8 (r = -0.421, $^{**}p = 0.007$), IP-10 ($r = -0.388$, $^{*}p = 0.013$), and MCP-1 ($r = -0.394$, $^{*}p = 0.012$) is negatively correlated with the FBUT. (g) LLT. The level of MIG ($r = -0.464$, $^{**}p = 0.003$), IFN-γ ($r = -0.463$, $^{*}p = 0.044$), and MCP-1 ($r = -0.761$, $^{***}p < 0.001$) is negatively correlated with the LLT. No significant correlations were found between LLT and other inflammatory cytokines (all $p > 0.05$). (h) CFS score. No significant correlations were found between CFS scores and each inflammatory cytokine (all $p > 0.05$). (i) OSDI score. The level of MIG ($r = 0.561$, $^{***}p < 0.001$), IFN-γ ($r = 0.321$, $^{*}p = 0.043$), and IL-8 ($r = 0.641$, $^{***}p < 0.001$) is positively correlated with the OSDI. No significant correlations were found between OSDI and other inflammatory cytokines (all $p > 0.05$). (j) TMH. The level of MIG ($r = 0.324$, $^{*}p = 0.041$) is positively correlated with the TMH. No significant correlations were found between TMH and other inflammatory cytokines (all $p > 0.05$). (k) SIT. No significant correlations were found between SIT and each inflammatory cytokine (all $p > 0.05$). Significant differences between the correlations with meibum inflammatory cytokines and ocular surface parameters. The bold values mean significant results. $^{*}p < 0.05$, $^{**}p < 0.01$, $^{***}p < 0.001$.

the potential inflammatory cytokines that are specifically involved in the pathogenesis of MGD has a large significance. Once a particular cytokine in meibum was found to be tightly related to the severity of the disease, then the inhibitor or agonist targeted to the particular cytokine could be developed as a potential therapeutic agent of MGD. This is the original purpose of our research, and some meaningful data were obtained.

In the current study, the majority of ocular parameters in MQ > 8 group exhibited more serious clinical characteristics, and they were statistically significant in contrast to MQ < 8 group. About meibum inflammation cytokines, the levels of 3 meibum inflammation cytokines (MIG, IP-10, and MCP-1) of the 5 inflammatory cytokines we examined were largely elevated in MGD patients with worse meibum quality. Integrated with these two parts these results, a conclusion can be drawn that the increase of meibum inflammatory cytokines accompanied with more serious disease degree. A previous study [22] showed that increased levels of various inflammatory cytokines in tears (IL-6, IL-8, TNF-α, and IFN-γ) were found in MGD patients than normal people, and these inflammatory cytokines were also associated with meibomian gland function and tear stability. Another report [23] investigated the tear inflammation cytokines between normal subjects and MGD patients, and it was observed that the amount of inflammation cytokines (such as TNF-α, IL-1β, IL-6, IL-8, IL-12p70, and IFN-γ) was significant elevated in the tear of MGD patients, so

inflammation may serve as the core characteristic in MGD patients. These reports verified our conclusion that worse meibomian gland function was closely associated with a higher level of tear inflammation cytokines. Thus, an inseparable relationship between the abnormalities of the meibomian glands is in association with ocular surface inflammation [9].

The 3 cytokines found robustly elevated in meibum are all classified to the chemokine family. MIG and IP-10 were included in CXCL family, while MCP-1 was included in CCL family. MIG/CXCL9 and IP-10/CXCL-10, also named "interferon-inducible CXC chemokine receptor 3 ligands", are ELR-negative CXC chemokines induced by IFN-γ or other stimuli during infection or inflammation in several immune cell [24]. Several studies [25, 26] have demonstrated that they can effectively activate and recruit T lymphocytes to the target organ in vivo to exert immune chemotaxis function. In the current study, the increases in MIG and IP-10 levels were found positively correlated with worse meibomian gland function, while they were negatively correlated with tear stability. Combined the robust immunomodulatory effect of CXCL family (MIG/CXCL-9 and IP-10/CXCL-10) [27–29] with the highly expression of these two chemokines in MGD patients, we speculated that MIG and IP-10 play a critical role in the pathogenesis of MGD.

According to relevant studies [30], CXC chemokines were pointed out to be associated with neovascularization, and CXC chemokines which lack of ELR (MIG/CXCL-9, IP10/CXCL-10) are potent inhibitors of angiogenesis and microvascular. The antiangiogenesis effect of MIG and IP10 have been applied and certified in the treatment of various diseases [31, 32]. Neovascularization and microvascular in lid margin can be found among many MGD patients [6, 33], so the treatment targeted on neovascularization and microvascular (IPL) in lid margin has been proved to be effective in MGD patients [34]. Hence, we speculated that the increase of MIG and IP-10 in meibum treatment may potentially achieve the therapeutic effect on MGD by downregulating angiogenesis cytokines to inhibit neovascularization and microvascular in lid margin. Based on the transitional inflammatory and obvious neovascularization responses in MGD, systemic and topical treatment which can combine anti-inflammation with antiangiogenesis should be accepted in regular strategies to maintain the normal function of meibomian glands, and especially novel molecular targeted on MIG and/or IP-10 may have great prospects in clinical.

MCP-1, also named as CCL-2, is an inflammatory cytokine that is specific for monocyte chemotactic proteins and can bind to NF-κB nuclear factor DNA to induce different immune cell migration to the designated tissue and trigger downstream signals to exert immune regulation functions [35, 36]. Our study has identified that MCP-1 was closely related with NIKBUT and FBUT, while not correlated with MGE and MQ. Compared to CCL chemokine family, we inferred that CXCL chemokines should be focused as the core pathogenesis of MGD. Based on the transitional expression of CXCL chemokines in meibum in MGD subjects, topical anti-CXCL-inflammation treatment have more potential to develop as novel strategies in the treatment of MGD.

Furthermore, there was no significant difference in the levels of IFN-γ and IL-8 between the two groups, but relationships were found between partially ocular parameters with these two cytokines in meibum. IL-8, also named as CXCL-8, is the most well-known molecule in the CXCL chemokine family, which has great attractive chemotactic effects on neutrophils, lymphocytes and basophils [37]. In contrast to normal people, IL-8 was found significantly elevated in tears in all kinds of dry eye patients, not just limited to MGD. Therefore, IL-8 may be positioned as the critical pathogenesis of various types of dry eye, and it strongly affects ocular discomfort symptoms [23, 38]. IL-8, as a vital member of the CXCL family, was confirmed to be related with MGE and MQ, thus the key role of CXCL family in maintaining normal meibomian gland function was confirmed once more. IFN-γ, the only member of type II interferon, is mainly secreted by natural killer cells (NK) and natural killer T cells (NKT) cells in the process of innate immunity and is also secreted by CD4 Th1 and CD8 cytotoxic T cells in the process of antigen-specific immunity [39]. Similar to IL-8, IFN-γ has also been proved to be significant elevated in most kinds of dry eye [23, 40]. OSDI, the only index to assess the subjective symptoms of dry eye, was found closely related to the levels of IL-8 and IFN-γ. Therefore, a combination therapy including anti-CXCL with anti-IL-8/anti-IFN-γ agent can simultaneously alleviate the ocular parameters and mitigate the discomfortable symptoms in MGD, to yield twice the result with half the effort.

Since the tear microenvironment is affected by various aspects, including tear quantity secreted by the lacrimal gland, meibum produced by the meibomian gland, and mucins secreted by the corneal and conjunctival epithelium [9], thus, the examination of the tear samples cannot be directly extrapolated to evaluate the function of meibomian gland. Meibum, as a noninvasive and convenient sample to obtain from meibomian glands directly, is the best carrier to reveal the microenvironment of meibomian glands. Therefore, the data obtained from meibum may be more accurate than the tear samples in the study of MGD. It is worth noting that meibum samples from MGD subjects were collected to more directly investigate the inflammation of meibomian glands, and we found that the expression of meibum inflammatory cytokines, especially chemokines (MIG, IP-10, and MCP-1) increased with the aggravation of MGD disease and can be detected as sensitive biomarkers in pre-evaluation the extent of MGD.

Due to the limitation of the small number of subjects, the inadequate number of inflammatory cytokines was also a deficiency in the current study. Furthermore, inflammatory cytokines have only been detected by Luminex chip without rechecked by ELISA assay, which is a shortcoming of the current study. Thus, further studies should be conducted with a larger number of participants examined with more analysis of meibum inflammatory cytokines using both Luminex chip and ELISA assay, to explicit illustrate more novel crucial cytokine biomarkers of MGD patients with strong evidence.

To the best of our knowledge, this study is the first to identify the chemokines in meibum samples, and we found that they were closely correlated with meibomian function and tear film instability. As the most direct and available carrier of meibomian gland secretion, the meibum sample is clearly more ideal for exploring the microenvironment of the meibomian glands than the tear sample. The current study provides a solid foundation for the technical support of meibum inflammatory cytokines in further meibomian gland inflammation research. Moreover, to prove that chemokines, especially CXCL family, play an important role in the pathogenesis of MGD, it can be well applied in developing novel therapeutic agents for MGD in clinical.

Abbreviations

CFS: Corneal fluorescein staining
IPL: Intense pulsed light
MCP-1: Monocyte chemotactic protein-1
MGD: Meibomian gland dysfunction
MGE: Meibomian gland expressibility
MIG: Monokine induced by IFN-γ
MQ: Meibomian gland quality
OSDI: Ocular surface disease index
TMH: Tear meniscus height
NIKBUT: Noninvasive tear break-up time
FBUT: Fluorescein tear film break-up time
FL: Fluorescein staining
IFN-γ: Interferon-gamma
IL-8: Interleukin-8
IP-10: Interferon-inducible protein-10
LLT: Lipid layer thickness
SIT: Schirmer I test
TMH: Tear meniscus height.

Data Availability

The datasets used and/or analyzed during the present study are available from the corresponding author on a reasonable request.

Ethical Approval

The present study was strictly performed on the basis of the Declaration of Helsinki for clinical and was approved by the Ethics Committee of the EENT Hospital of Fudan University (Shanghai, China). After all details and potential benefits and risks were explicit and explained, written informed consents were obtained from all participants prior to the examination and treatment.

Conflicts of Interest

The authors declare that the research was conducted in the absence of any commercial or financial relationships that could be construed as a potential conflict of interest. Any product that may be evaluated in this article, or a claim that may be made by its manufacturer, is not guaranteed or endorsed by the publisher.

Authors' Contributions

LG participated in the project design and revision of the manuscript. WL was responsible for the enrolment and follow-up of the patients and participated in performing the statistical analysis. WL also drafted the manuscript. Both authors confirm the authenticity of the raw data and read and approved the final manuscript. Wenting Liu and Tong Lin contributed equally to this work.

Acknowledgments

This study was financially supported by the National Natural Science Foundation of China (Grant No. 82000855 to LT), Shanghai Sailing Program (Grant No. 19YF1405800 to LT), and the Shanghai Rising Stars of Medical Talents Youth Development Program (Youth Medical Talents Specialist Program to LT). The authors would like to thank Huaying Biotechnologies for providing tear inflammation cytokines examination.

References

[1] J. D. Nelson, J. Shimazaki, J. M. Benitez-del-Castillo et al., "The international workshop on meibomian gland dysfunction: report of the definition and classification subcommittee," *Investigative Ophthalmology & Visual Science*, vol. 52, no. 4, pp. 1930–1937, 2011.

[2] F. Stapleton, M. Alves, V. Y. Bunya et al., "TFOS DEWS II epidemiology report," *The Ocular Surface*, vol. 15, no. 3, pp. 334–365, 2017.

[3] J. P. Craig, J. D. Nelson, D. T. Azar et al., "TFOS DEWS II report executive summary," *The Ocular Surface*, vol. 15, no. 4, pp. 802–812, 2017.

[4] N. Nicolaides, J. K. Kaitaranta, T. N. Rawdah, J. I. Macy, Boswell FM 3rd, and R. E. Smith, "Meibomian gland studies: comparison of steer and human lipids," *Investigative Ophthalmology & Visual Science*, vol. 20, no. 4, pp. 522–536, 1981.

[5] Y. Wei and P. A. Asbell, "The core mechanism of dry eye disease is inflammation," *Eye & Contact Lens*, vol. 40, no. 4, pp. 248–256, 2014.

[6] G. Geerling, J. Tauber, C. Baudouin et al., "The international workshop on meibomian gland dysfunction: report of the subcommittee on management and treatment of meibomian gland dysfunction," *Investigative Ophthalmology & Visual Science*, vol. 52, no. 4, pp. 2050–2064, 2011.

[7] S. C. Pflugfelder and C. S. de Paiva, "The pathophysiology of dry eye disease: what we know and future directions for research," *Ophthalmology*, vol. 124, no. 11, pp. S4–S13, 2017.

[8] H. Lee, B. Chung, K. S. Kim, K. Y. Seo, B. J. Choi, and T. I. Kim, "Effects of topical loteprednol etabonate on tear cytokines and clinical outcomes in moderate and severe meibomian gland dysfunction: randomized clinical trial," *American Journal of Ophthalmology*, vol. 158, no. 6, pp. 1172–1183.e1, 2014.

[9] M. D. P. Willcox, P. Argueso, G. A. Georgiev et al., "TFOS DEWS II tear film report," *The Ocular Surface*, vol. 15, no. 3, pp. 366–403, 2017.

[10] A. J. Bron, C. S. de Paiva, S. K. Chauhan et al., "TFOS DEWS II pathophysiology report," *The Ocular Surface*, vol. 15, no. 3, pp. 438–510, 2017.

[11] M. Muller, S. Carter, M. J. Hofer, and I. L. Campbell, "Review: The chemokine receptor CXCR3 and its ligands CXCL9, CXCL10 and CXCL11 in neuroimmunity - a tale of conflict and conundrum," *Neuropathology and Applied Neurobiology*, vol. 36, no. 5, pp. 368–387, 2010.

[12] J. W. Griffith, C. L. Sokol, and A. D. Luster, "Chemokines and chemokine receptors: positioning cells for host defense and immunity," *Annual Review of Immunology*, vol. 32, no. 1, pp. 659–702, 2014.

[13] Y. Wei, N. Gadaria-Rathod, S. Epstein, and P. Asbell, "Tear cytokine profile as a noninvasive biomarker of inflammation for ocular surface diseases: standard operating procedures," *Investigative Ophthalmology & Visual Science*, vol. 54, no. 13, pp. 8327–8336, 2013.

[14] R. Liu, B. Rong, P. Tu et al., "Analysis of cytokine levels in tears and clinical correlations after intense pulsed light treating meibomian gland dysfunction," *American Journal of Ophthalmology*, vol. 183, pp. 81–90, 2017.

[15] A. Tomlinson, A. J. Bron, D. R. Korb et al., "The international workshop on meibomian gland dysfunction: report of the diagnosis subcommittee," *Investigative Ophthalmology & Visual Science*, vol. 52, no. 4, pp. 2006–2049, 2011.

[16] W. Liu and L. Gong, "Anti-demodectic effects of okra eyelid patch in demodexblepharitis compared with tea tree oil," *Experimental and Therapeutic Medicine*, vol. 21, no. 4, p. 338, 2021.

[17] S. Zhao, N. Song, and L. Gong, "Changes of dry eye related markers and tear inflammatory cytokines after upper blepharoplasty," *Frontiers in Medicine*, vol. 8, article 763611, 2021.

[18] S. Y. Lee, K. Lee, C. K. Park et al., "Meibomian gland dropout rate as a method to assess meibomian gland morphologic changes during use of preservative-containing or preservative-free topical prostaglandin analogues," *PLoS One*, vol. 14, no. 6, article e0218886, 2019.

[19] K. Y. Seo, S. M. Kang, D. Y. Ha, H. S. Chin, and J. W. Jung, "Long-term effects of intense pulsed light treatment on the ocular surface in patients with rosacea-associated meibomian gland dysfunction," *Contact Lens & Anterior Eye*, vol. 41, no. 5, pp. 430–435, 2018.

[20] K. K. Nichols, G. N. Foulks, A. J. Bron et al., "The international workshop on meibomian gland dysfunction: executive summary," *Investigative Ophthalmology & Visual Science*, vol. 52, no. 4, pp. 1922–1929, 2011.

[21] S. Zhao, J. Duan, J. Zhang, and L. Gong, "Evaluation of Meibomian gland function after therapy of eyelid tumors at palpebral margin with super pulse CO2 laser," *Disease Markers*, vol. 2022, Article ID 8705436, 6 pages, 2022.

[22] H. Lam, L. Bleiden, C. S. de Paiva, W. Farley, M. E. Stern, and S. C. Pflugfelder, "Tear cytokine profiles in dysfunctional tear syndrome," *American Journal of Ophthalmology*, vol. 147, no. 2, pp. 198–205.e1, 2009.

[23] H. Zhao, Q. Li, M. Ye, and J. Yu, "Tear Luminex analysis in dry eye patients," *Medical Science Monitor*, vol. 24, pp. 7595–7602, 2018.

[24] A. D. Luster, "Chemokines — Chemotactic Cytokines That Mediate Inflammation," *The New England Journal of Medicine*, vol. 338, no. 7, pp. 436–445, 1998.

[25] J. R. Groom and A. D. Luster, "CXCR3 ligands: redundant, collaborative and antagonistic functions," *Immunology and Cell Biology*, vol. 89, no. 2, pp. 207–215, 2011.

[26] K. Van Raemdonck, P. E. Van den Steen, S. Liekens, J. Van Damme, and S. Struyf, "CXCR3 ligands in disease and therapy," *Cytokine & Growth Factor Reviews*, vol. 26, no. 3, pp. 311–327, 2015.

[27] W. P. Kuan, L. S. Tam, C. K. Wong et al., "CXCL 9 and CXCL 10 as sensitive markers of disease activity in patients with rheumatoid arthritis," *The Journal of Rheumatology*, vol. 37, no. 2, pp. 257–264, 2010.

[28] J. M. Rosenblum, N. Shimoda, A. D. Schenk et al., "CXC chemokine ligand (CXCL) 9 and CXCL10 are antagonistic costimulation molecules during the priming of alloreactive T cell effectors," *Journal of Immunology*, vol. 184, no. 7, pp. 3450–3460, 2010.

[29] A. Antonelli, S. M. Ferrari, D. Giuggioli, E. Ferrannini, C. Ferri, and P. Fallahi, "Chemokine (C-X-C motif) ligand (CXCL)10 in autoimmune diseases," *Autoimmunity Reviews*, vol. 13, no. 3, pp. 272–280, 2014.

[30] R. M. Strieter, M. D. Burdick, B. N. Gomperts, J. A. Belperio, and M. P. Keane, "CXC chemokines in angiogenesis," *Cytokine & Growth Factor Reviews*, vol. 16, no. 6, pp. 593–609, 2005.

[31] Q. Shen, X. Fan, M. Jiang, Z. Ye, Y. Zhou, and W. S. Tan, "Inhibiting expression of Cxcl9 promotes angiogenesis in MSCs-HUVECs co-culture," *Archives of Biochemistry and Biophysics*, vol. 675, article 108108, 2019.

[32] J. S. Carew, C. M. Espitia, W. Zhao, M. M. Mita, A. C. Mita, and S. T. Nawrocki, "Oncolytic reovirus inhibits angiogenesis through induction of CXCL10/IP-10 and abrogation of HIF activity in soft tissue sarcomas," *Oncotarget*, vol. 8, no. 49, pp. 86769–86783, 2017.

[33] E. Knop, N. Knop, T. Millar, H. Obata, and D. A. Sullivan, "The international workshop on meibomian gland dysfunction: report of the subcommittee on anatomy, physiology, and pathophysiology of the meibomian gland," *Investigative Ophthalmology & Visual Science*, vol. 52, no. 4, pp. 1938–1978, 2011.

[34] S. Cote, A. C. Zhang, V. Ahmadzai et al., "Intense pulsed light (IPL) therapy for the treatment of meibomian gland dysfunction," *Cochrane Database of Systematic Reviews*, vol. 3, article CD013559, 2020.

[35] X. Bai, Z. Qi, G. Song et al., "Effects of monocyte chemotactic Protein-1 and nuclear factor of kappa B pathway in rejection of cardiac allograft in rat," *Transplantation Proceedings*, vol. 47, no. 6, pp. 2010–2016, 2015.

[36] G. Ghoniem, B. Farhan, D. Csuka, and F. Zaldivar, "Potential role of monocyte chemoattractant Protein-1 in monitoring disease progression and response to treatment in overactive bladder patients," *International Neurourology Journal*, vol. 24, no. 4, pp. 341–348, 2020.

[37] R. C. Russo, C. C. Garcia, M. M. Teixeira, and F. A. Amaral, "The CXCL8/IL-8 chemokine family and its receptors in inflammatory diseases," *Expert Review of Clinical Immunology*, vol. 10, no. 5, pp. 593–619, 2014.

[38] C. Zhang, H. Ding, H. He et al., "Comparison of early changes in ocular surface markers and tear inflammatory mediators after femtosecond lenticule extraction and FS-LASIK," *International Journal of Ophthalmology*, vol. 14, no. 2, pp. 283–291, 2021.

[39] H. Lee, K. Min, E. K. Kim, and T. I. Kim, "Minocycline controls clinical outcomes and inflammatory cytokines in moderate and severe meibomian gland dysfunction," *American Journal of Ophthalmology*, vol. 154, no. 6, pp. 949–957.e1, 2012.

[40] T. G. Coursey, R. Bohat, F. L. Barbosa, S. C. Pflugfelder, and C. S. de Paiva, "Desiccating stress-induced chemokine expression in the epithelium is dependent on upregulation of NKG2D/RAE-1 and release of IFN-γ in experimental dry eye," *Journal of Immunology*, vol. 193, no. 10, pp. 5264–5272, 2014.

Hindawi
Disease Markers
Volume 2022, Article ID 1730501, 9 pages
https://doi.org/10.1155/2022/1730501

Research Article

Hypermixed Convolutional Neural Network for Retinal Vein Occlusion Classification

Guanghua Zhang,[1,2] **Bin Sun**,[3] **Zhaoxia Zhang**,[3] **Shiyu Wu**,[4] **Guangping Zhuo**,[4] **Huifang Rong**,[1] **Yunfang Liu**,[5] **and Weihua Yang**[6]

[1]*Department of Intelligence and Automation, Taiyuan University, Taiyuan 030000, China*
[2]*Graphics and Imaging Laboratory, University of Girona, Spain*
[3]*Shanxi Eye Hospital, Taiyuan 030002, China*
[4]*Department of Computer, Taiyuan Normal University, Jinzhong 030619, China*
[5]*The First Affiliated Hospital of Huzhou University, Huzhou 313000, China*
[6]*Shenzhen Eye Hospital, Jinan University, Shenzhen 518040, China*

Correspondence should be addressed to Yunfang Liu; panlele0701@139.com and Weihua Yang; benben0606@139.com

Received 30 August 2022; Accepted 30 September 2022; Published 11 November 2022

Academic Editor: Yi Shao

Retinal vein occlusion (RVO) is one of the most common retinal vascular diseases leading to vision loss if not diagnosed and treated in time. RVO can be classified into two types: CRVO (blockage of the main retinal veins) and BRVO (blockage of one of the smaller branch veins). Automated diagnosis of RVO can improve clinical workflow and optimize treatment strategies. However, to the best of our knowledge, there are few reported methods for automated identification of different RVO types. In this study, we propose a new hypermixed convolutional neural network (CNN) model, namely, the VGG-CAM network, that can classify the two types of RVOs based on retinal fundus images and detect lesion areas using an unsupervised learning method. The image data used in this study is collected and labeled by three senior ophthalmologists in Shanxi Eye Hospital, China. The proposed network is validated to accurately classify RVO diseases and detect lesions. It can potentially assist in further investigating the association between RVO and brain vascular diseases and evaluating the optimal treatments for RVO.

1. Introduction

Early changes in the retina are influenced by many factors, such as unfavorable environmental factors, including aging, a high-carbohydrate diet, and a sedentary lifestyle [1], and systemic diseases, including hyperglycemia [2], hyperlipidemia [3], and hypertension [4]. Retinal blood vessels are the only blood vessels available for noninvasive imaging in the human body. The pathological changes in retinal blood vessels occur much earlier than clinical symptomatic lesions. Therefore, retinal images have been widely used to detect early signs of systemic vascular diseases. In recent years, with an increase in the elderly population and the acceleration of the aging society in China, the fundus diseases of the elderly occur more frequently. Impaired vision can significantly impact an older person's quality of life and ability to live independently [5].

Retinal vessels are important structures of our eyes [6], and their detection and analysis are of great significance for the study of ocular diseases. Patients with retinal diseases may exhibit serious complications that cause severe visual impairment owing to a lack of awareness of retinal diseases and limited medical resources [7]. Retinal vein occlusion (RVO) [8] is one of the important eye diseases considered a risk factor for cardiovascular mortality and stroke in aging people [9]. Its typical symptoms include exudate [10], capillary nonperfusion [11], collateral formation [12], microaneurysm [13], sclerosed veins [14], and telangiectatic vessels [15]. Ischemic RVO is usually complicated by macular edema (ME) [16] and retinal and iris neovascularization

[17], resulting in significant visual loss. RVO is classified into central and branch RVO (CRVO and BRVO). CRVO involves superficial or deep retinal hemorrhages (HEs) [18] that are scattered around the vein near the lamina cribrosa [19], and BRVO involves hemorrhages occurring within the occluded venule from the retinal sector to the blood supply sector, which is caused by arterial compression onto veins [20] (see Figure 1). RVO is the second most common retinal vascular eye disease after diabetic retinopathy (DR) [21]. If RVO is not treated in a timely manner, it can lead to serious complications that cause severe visual impairment [22, 23]. So far, the number of patients with RVO has increased [24], but our understanding of its pathogenesis, our ability to modify the final visual outcome, and the availability of treatments to effectively intervene in the progression of the disorder are all relatively limited [25].

Diagnosing ophthalmological diseases through deep learning models [26] has been used broadly in recent years [27]. A convolutional neural network (CNN) is one of the most famous deep learning architectures designed in 1989 [28]. Krizhevsky et al. [29] trained a large CNN architecture with eight layers and millions of parameters using a large ImageNet data set containing 1 million training images. In the field of ophthalmology, Litjens et al. [27] used a CNN to automatically segment macular edema based on OCT images. Google used a CNN network to automate the classification of diabetic retinopathy [30] and obtained the experimental results of 99% referral accuracy by training more than 100,000 data sets. The technology has been approved by the FDA as an official medical product. CNN is good at extracting feature information of different colors, spaces, and edges of images by using convolution modules of different scales and integrating all features into higher-order abstract features of images through continuous nonlinear transformation combinations. High-order abstract features and basic features are used together in the final learning process. CNN is almost a conventional method for medical image analysis, including color fundus images (CFIs) [27]. It is better in configuring spatial information by taking images as input. The achievements of CNN in autodiagnosis on different medical aspects can be found in [27], and it has been proved to surpass humans in some cases. So far, a hierarchical CNN architecture capable of distinguishing between normal CFIs and BRVO CFIs has been proposed by Zhang et al. [31] and developed by Zhao et al. [32]. Over the past several years, many modified and deeper CNN architectures have been proposed, which are not only used in the medical imaging domain but also widely applied in other domains [33].

Our study proposed an advanced model that can classify all normal, CRVO, and BRVO CFIs and detect the visible hemorrhage areas. It will help ophthalmologists realize computer-aided diagnosis in pathological analysis [34] to alleviate their pressure and discover and treat RVO as early as possible [35]. We will illustrate the methods employed in our model in the next chapter, followed by experimental results and final remarks in the third and fourth chapters, respectively.

2. Materials and Methods

When dealing with medical images, the structural and configuration information between adjacent pixels is a great source for analysis. A CNN that combines convolutional layers, pooling layers, and fully connected layers is more capable of extracting this type of information from 2D or 3D images. Convolutional layers apply a convolution operation by processing images only in receptive fields and adapting the weights gradually during the learning process. Pooling layers are usually followed by convolutional layers to reduce the dimensions of their output. Fully connected layers flatten data from previous layers to one dimension. A simple CNN framework is shown in Figure 2.

In this study, we also use the same data sets to conduct the control experiments on Resnet-34 [37], Inception-V3 [38], and MobileNet [39] models. Resnet [40] is the champion of the ImageNet large-scale visual recognition challenge (ILSVRC) in 2015. Resnet-34 [37] model is mainly composed of residual blocks, through which a deep network can be built and residual learning can be carried out in the feature extraction process. The Inception model is a deep CNN architecture proposed by Szegedy et al. [41] in ILSVRC 2014. The asymmetric multiconvolution kernel structure of the Inception-V3 [38] model performs the splitting operation on the larger convolution. Convolution kernels with different sizes are adopted so that receptive fields of different sizes can exist. The calculation efficiency of model parameters is improved, and the overfitting of the model is reduced. The MobileNet [39] model was proposed by a Google team [42] in 2017 and consists of a series of basic deep separable convolution (DSC) units. The model has a high precision and involves a small number of parameters and calculations.

2.1. Model Architecture. The study introduces a new CNN framework to classify RVO types and detect lesions. It is known as the VGG-CAM network, which utilizes a modified VGG19 network, general average pooling (GAP), class activation mapping (CAM), and CAM attention.

VGG19 [43] is a CNN architecture introduced by Simonyan and Zisserman. They used small receptive fields (3×3 matrix) to detect features from different positions of images and added the number of convolutional layers to increase the reception area for these receptive fields. Our VGG-CAM network reduces the number of fully connected layers in the original VGG19 networks from three to one and replaces them with a GAP layer. In the feature extraction stage, the auxiliary classifier and CAM attention layer are introduced to further enhance the model's activation weight for the lesion area. An additional CAM layer is connected with the GAP layer for lesion detection. SoftMax is applied as an activation function for the final fully connected layer, which predicts probabilities of different classes that the CFI can be labeled. The 24-layer framework of the VGG-CAM network is shown in Figure 3.

In the VGG-CAM network, the GAP layer preserves more information from input images [44], which helps detect lesion areas in the input image. Compared with average pooling, GAP only outputs one parameter from each

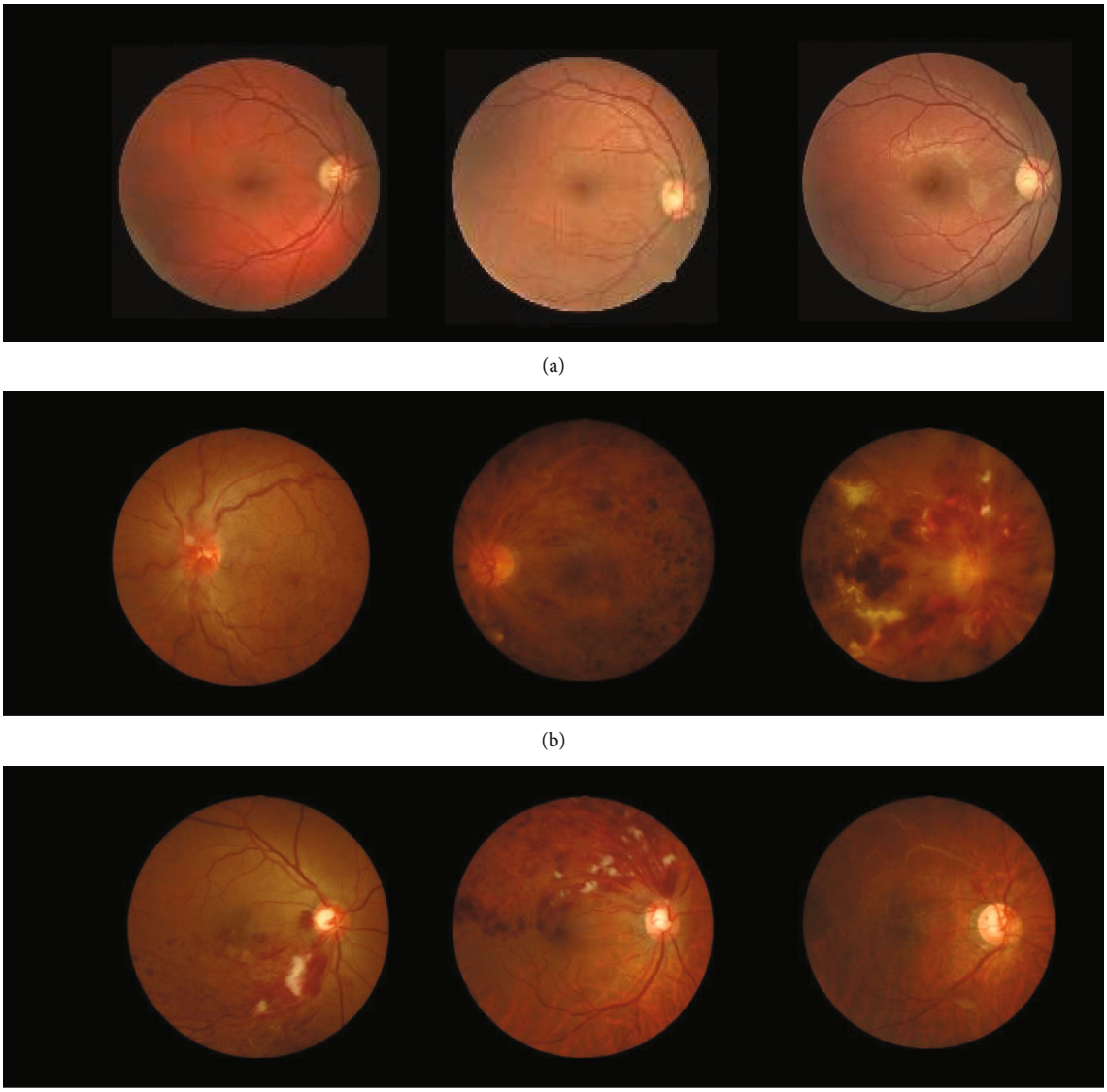

(a)

(b)

(c)

Figure 1: (a) Normal retina images, (b) CRVO retina images, and (c) BRVO retina images.

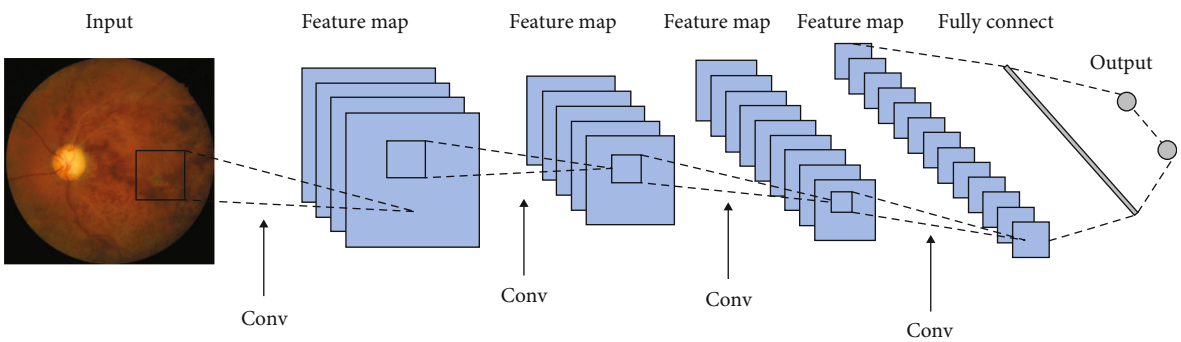

Figure 2: A simple CNN framework containing input, convolutional, pooling (subsampling), and fully connected layers (Heung-II, [36]).

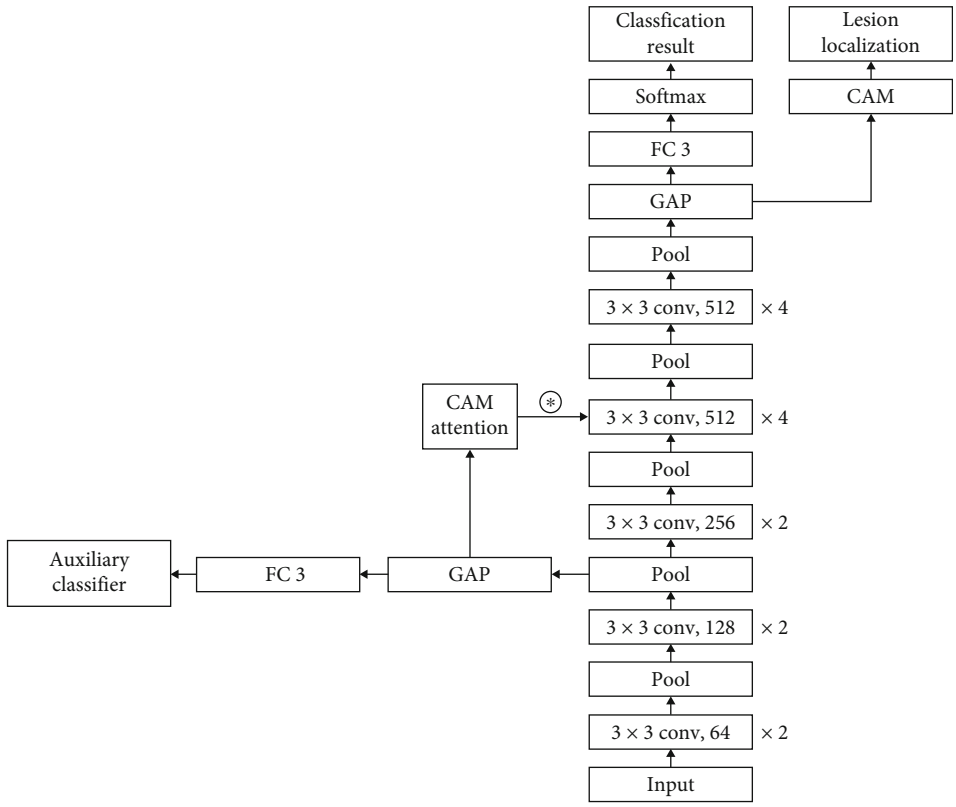

Figure 3: Framework of VGG-CAM model for RVO classification and lesion detection.

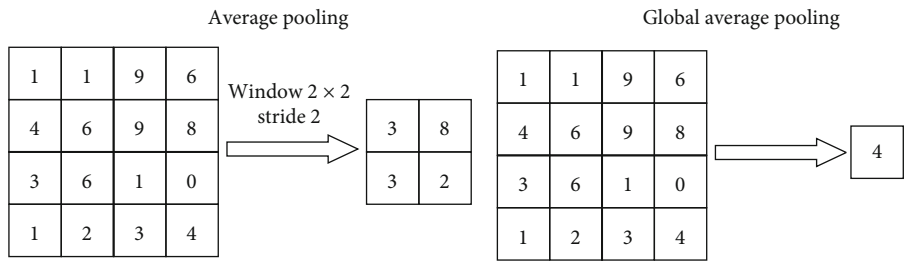

Figure 4: Examples of average pooling and GAP.

receptive field (see Figure 4). Compared with the former, it uses less time to optimize the network. Lin et al. proved that the reduction of parameters in GAP has no effect on the accuracy of final networks [44].

The CAM layer's computation is as follows:

$$\mathrm{CAM} = \sum_{i=0}^{C} \omega_i * F_i, \tag{1}$$

where C represents the number of channels in the feature map of the previous GAP layer. For each feature channel, the CAM layer augments products of weights ω_i from the fully connected layer and feature maps F_i before the GAP layer, as seen in Figure 5.

The CAM layer first uses Equation (1) to compute the class activation image of the original CFIs. It then applies bilinear interpolation to turn the class activation image into the size of the original image, followed by a threshold segmentation to detect the lesion location.

In the feature extraction stage, some useless information often affects the final classification accuracy; further, the extraction of key pathological features is the key to classification. The attention mechanism can guide the model to independently select the lesion area to be noticed. The feature weights are generated by introducing the auxiliary classifier and CAM attention layer after the sixth pooling layer. The feature weight is introduced into the feature map of the 10th layer to improve the model's attention and learning of the lesion area and further improve the final classification effect and the accuracy of lesion detection.

2.2. Image Preprocessing. Input images were mainly preprocessed by contrast limited adaptive histogram equalization

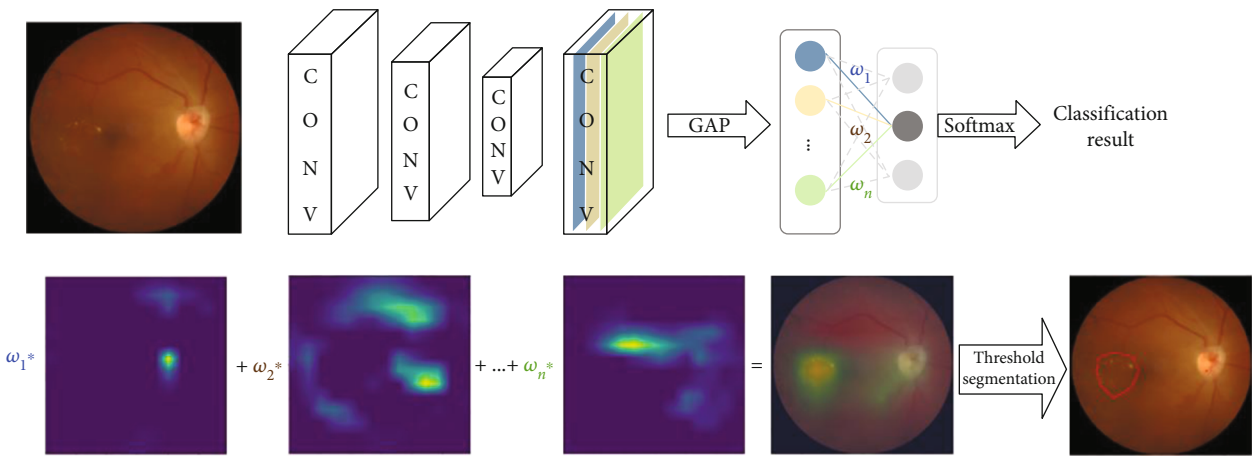

Figure 5: RVO lesion detection by CAM.

(CLAHE) to increase contrast in original images [45]. Flipping, twisting, and zooming were used as well to increase the variety in our image database, which improves the model's ability to recognize various RVO images. Figure 6 presents the differences between original and preprocessed input images.

2.3. Model Initialization

2.3.1. Transfer Learning. Transfer learning [46] applies pretrained weights on a network from another problem as the initial weights for the same network in a different problem. In the problem of image processing, the shallow network of a neural network is mainly responsible for the feature extraction of shallow elements in an image, such as points, edges, and other such elements. Universal pretrained weights can reduce the network's learning time on a different problem [47]. The VGG-CAM model used pretrained weights from ImageNet as initial weights, which was trained by over a million images containing over 1,000 labeled images (https://www.image-net.org/).

2.3.2. Stage-Wise Training. Stage-wise training [48] assigns priority to features of images. It separates the entire learning process into several sublearning processes, and the ability to extract different levels of image features is achieved through different learning processes. It allows information from the images to be processed gradually in the model [49]. In the earliest stage (the first eight layers in our model), the network accessed only a subset of the image, especially its coarse-scale features. Following stage II (8th to 13th layers) and stage III (13th to 18th layers), finer information was extracted from the image, and the feedback was used to evolve the previous stages for a better prediction. Stage III is the only prior for feature learning of the final stage (the fully connected layer).

2.3.3. Environment. Operating system: Ubuntu 18.04 LTS; language: Python 3.6.8, Keras; GPU: GTX1080ti; CPU: Intel i7; Memory: Kingston DDR4 16 G.

3. Results and Discussion

3.1. Evaluation Metrics. In this experiment, the ability to identify unsupervised lesions was tested first, and then, the classification performance of the VGG-CAM model was tested in terms of sensitivity (Se), specificity (Sp), and Kappa. The calculation formulas of each index are shown below.

$$\mathrm{Se} = \frac{\mathrm{TP}}{\mathrm{FN} + \mathrm{TP}}, \tag{2}$$

$$\mathrm{Sp} = \frac{\mathrm{TN}}{\mathrm{FP} + \mathrm{TN}}, \tag{3}$$

$$\mathrm{Kappa} = \frac{P_0 - P_e}{1 - P_e}. \tag{4}$$

In Equations (2) and (3), TP indicates that the positive class is predicted as the positive class number, TN indicates that the negative class is predicted as the negative class number, FN indicates that the negative class is predicted as the positive class number, and FP indicates that the negative class is predicted as the positive class number.

In Equation (4), P_0 represents the sum of the number of samples correctly classified for each class divided by the total number of samples, that is, the overall classification accuracy. Assume that the real number of samples of each class is $a_1, a_2, \cdots, a_n$, respectively, the predicted number of samples of each class is $b_1, b_2, \cdots, b_n$, respectively, and the total number of samples is n; then, P_e is expressed as

$$P_e = \frac{a_1 \times b_1 + a_2 \times b_2 + \cdots + a_n \times b_n}{n \times n}. \tag{5}$$

3.2. Lesion Detection. Figure 7 presents examples of a detected lesion in BRVO and CRVO CFIs. For BRVO CFIs, the VGG-CAM network is sufficiently capable of identifying exudate, sclerosed veins, and hemorrhages. However, the network only highlights parts of a hemorrhage when the hemorrhage area is large. As for CRVO that has hemorrhage spreading all over the retina, the VGG-CAM network only

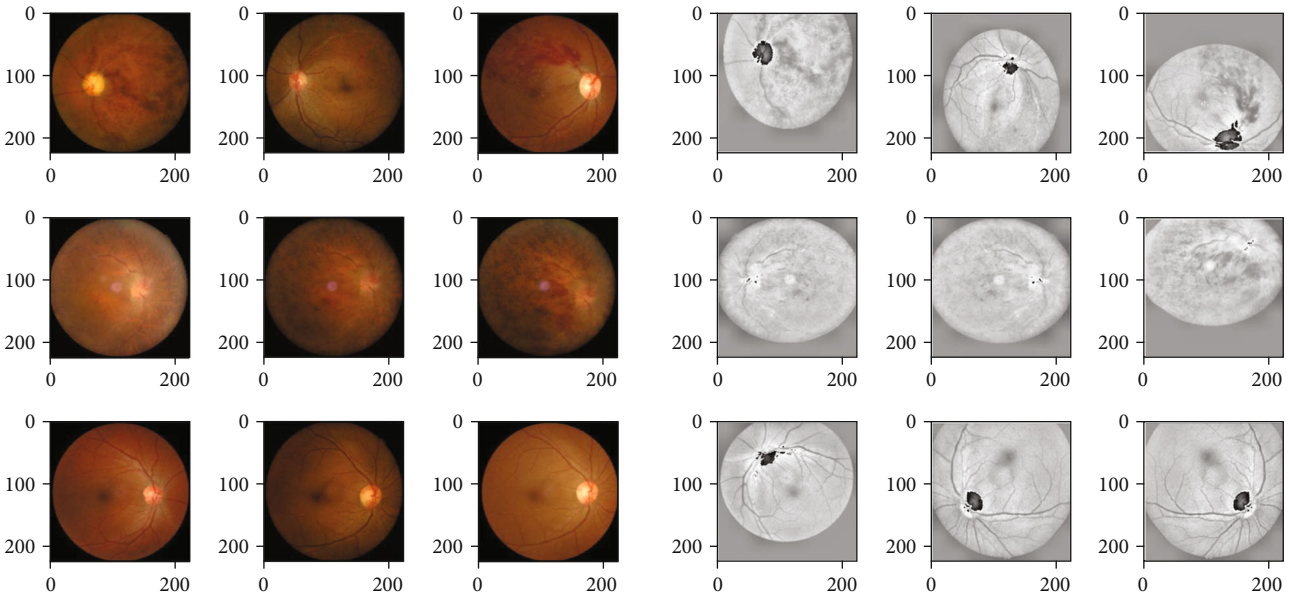

Figure 6: Input images before and after preprocessing.

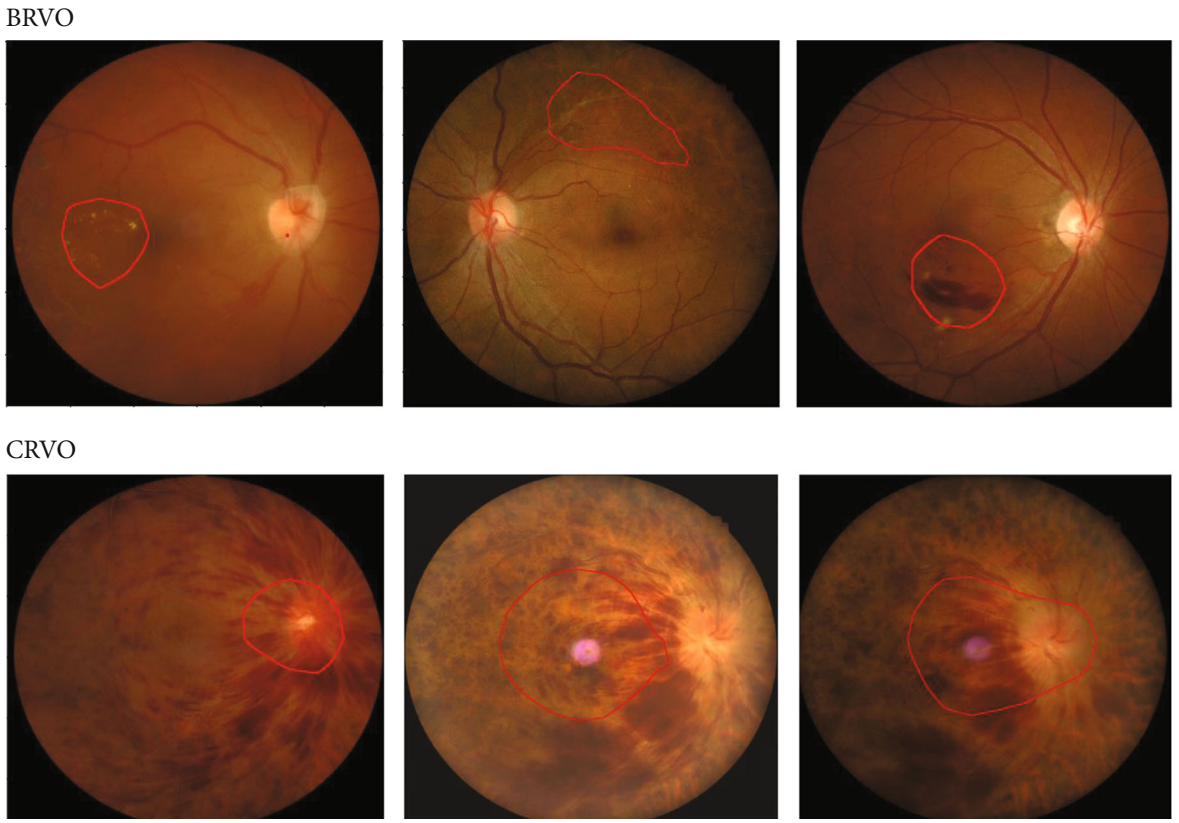

Figure 7: Lesion detection by VGG-CAM network on problematic areas of BRVO and CRVO.

indicates the central area of hemorrhage, namely, lamina cribrosa.

3.3. RVO Classification. The performance of the VGG-CAM network on the validation set is shown in Figure 8 and Table 1. Model scores of the VGG-CAM network (see Table 1) show that the model has a high sensitivity and specificity in classifying BRVO, CRVO, and normal CFIs. When distinguishing between RVO and normal CFIs, the model has only one misclassified image. When distinguishing

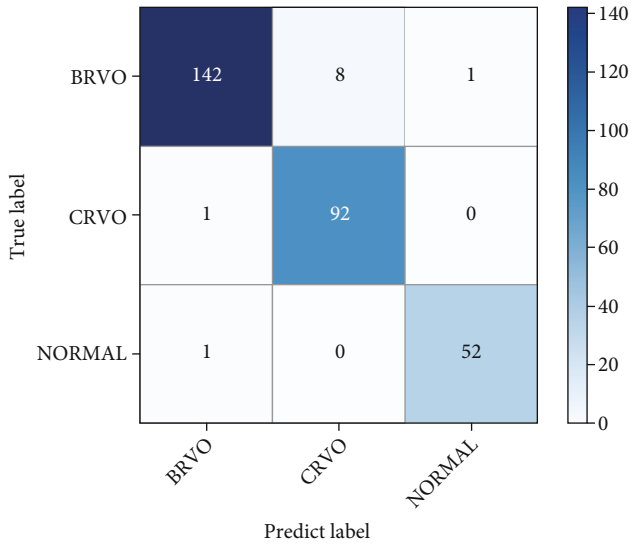

Figure 8: Confusion matrix of VGG-CAM network on validation set.

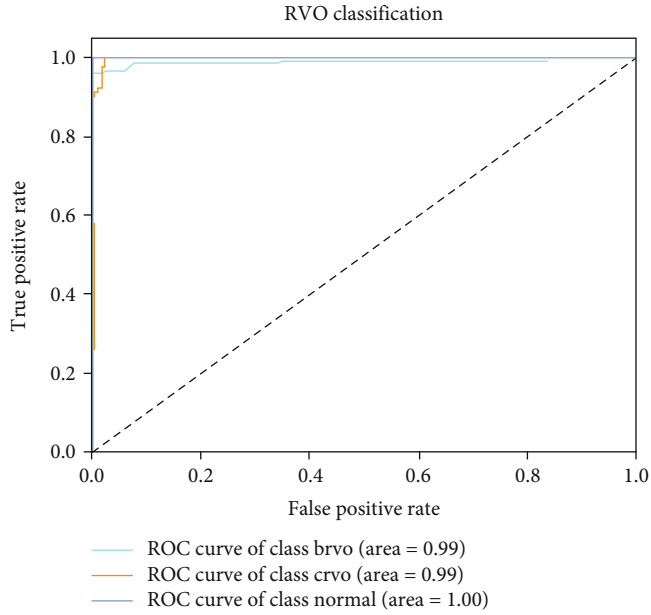

Figure 9: ROC curve of VGG-CAM network performance on RVO classification.

Table 1: VGG-CAM network model scores on RVO classification.

Prediction	Sensitivity	Specificity	Kappa	Number of CFIs
BRVO	0.94	0.99	0.97	151
CRVO	0.99	0.96	0.88	93
Normal	0.98	0.99	0.98	53

Table 2: Comparison of the results of various methods on RVO classification.

Model	Sensitivity	Specificity
Resnet-34	0.92	0.92
Inception-V3	0.90	0.91
MobileNet	0.89	0.90
VGG-CAM without CAM attention	0.95	0.94
VGG-CAM attention	0.97	0.96

between BRVO and CRVO CFIs, it mislabeled eight CRVO images as BRVO. However, the sensitivity and specificity of classifying the three labels are above 94%, and the specificity is above 96%. The results of BRVO and normal CFIs are over 97% in the Kappa coefficient, but the results of CRVO CFIs are only 88%.

From the experimental results in Table 2, it can be seen that the sensitivity and specificity of the model after adding CAM and CAM attention layers are significantly improved when compared with the current classification models with better effects. From the results with CAM attention and without CAM attention, it can be seen that the CAM attention layer enables the model to more effectively extract lesion areas to enhance the final classification effect.

The following ROC curve (see Figure 9) plots the false positive rate (FPR) against the true position rate (TPR). The closer the curve is to (0,1), the more sensitive and accurate the model is. It shows that the area of all curves in the VGG-CAM model reaches 0.99, where the area under the curve of the normal label (1.00) indicates the model is capable of distinguishing between normal CFIs and RVO CFIs. The curves of the BRVO and CRVO labels have an area of 0.99, which indicates a slight probability of mislabeling between each other.

4. Conclusions

This study proposes a hybrid CNN, VGG-CAM, for RVO classification and lesion detection. The CAM attention layer was introduced to enhance the model's attention to the lesion area, and the network parameters learned from the ultralarge data set were used for the initialization of this network by migration learning. Stage training was used to reduce the training time of the model and improve the parameter optimization ability. Further, based on unsupervised learning method, the global average pooling and class activation methods were also used for lesion detection. The experimental results showed that the proposed model can accurately classify BRVO, CRVO, and normal fundus images, detect the lesion areas, and give the prediction results and clinical basis for the resulting judgment.

However, BRVO did not perform as well as CRVO and normal CFIs in sensitivity. For CRVO, the current lesion detection branches cannot achieve a high-precision prediction. This proposed model was only used for the preliminary study of fundus images in the field of view with a 55-degree lens. We concluded that the samples lacked diversity under the specific shooting field of the equipment. In future works, we will improve the model performance with image data from different medical devices and different fields of view

and further improve the lesion detection accuracy of the model through a supervised learning method.

Data Availability

The underlying data used to support the findings of this study are available from the corresponding author upon request.

Conflicts of Interest

The authors declare that there is no conflict of interest regarding the publication of this paper.

Authors' Contributions

Guanghua Zhang, Bin Sun, and Zhaoxia Zhang contributed to the work equally and should be regarded as co-first authors.

Acknowledgments

This work was supported by the Research Funds of Shanxi Transformation and Comprehensive Reform Demonstration Zone (Grant No. 2018KJCX04), the Fund for Shanxi "1331 Project", and the Key Research and Development Program of Shanxi Province (Grant No. 201903D311009). The work was also partially sponsored by the Scientific Innovation Plan of Universities in Shanxi Province (Grant No. 2021L575), the Innovation and Entrepreneurship Training Program for College Students (Grant No. 202111242006X), the Shanxi Scholarship Council of China (Grant No. 2020-149), the Shenzhen Fund for Guangdong Provincial High-level Clinical Key Specialties (SZGSP014), the Sanming Project of Medicine in Shenzhen (SZSM202011015), and the Shenzhen Science and Technology Planning Project (KCXFZ20211020163813019).

References

[1] J. Yang, X. Dong, Y. Hu et al., "Fully automatic arteriovenous segmentation in retinal images via topology-aware generative adversarial networks," *Interdisciplinary Sciences, Computational Life Sciences*, vol. 12, no. 3, 2020.

[2] B. Horton William, A. Jahn Linda, M. Hartline Lee, W. Aylor Kevin, T. Patrie James, and E. J. Barrett, "Hyperglycemia does not inhibit Insulin's effects on microvascular perfusion in healthy humans: a randomized crossover study," *American Journal of Physiology Endocrinology and Metabolism*, vol. 319, no. 4, pp. E753–E762, 2020.

[3] W. Shiming and B. Xianyi, "Hyperlipidemia, blood lipid level, and the risk of glaucoma: a meta-analysis," *Investigative Ophthalmology & Visual Science*, vol. 60, no. 4, p. 1028, 2019.

[4] D. Jiajun, Z. Guoning, Y. Yanhong, L. Miao, and H. Yao, "Blood pressure and hypertension prevalence among oldest-old in China for 16 year: based on CLHLS," *BMC Geriatrics*, vol. 19, no. 1, 2019.

[5] M. Perry, "Eye disease in older adults: risk factors and treatments," *Journal of Community Nursing*, vol. 34, no. 3, 2020.

[6] J. Xu, J. Shen, C. Wan, Q. Jiang, Z. Yan, and W. Yang, "A few-shot learning-based retinal vessel segmentation method for assisting in the central serous chorioretinopathy laser surgery," *Frontiers in Medicine*, vol. 9, article 821565, 2022.

[7] J. Zhao, Y. Lu, Y. Qian, Y. Luo, and W. Yang, "Emerging trends and research foci in artificial intelligence for retinal diseases: bibliometric and Visualization study," *Journal of Medical Internet Research*, vol. 24, no. 6, article e37532, 2022.

[8] N. Luke, J. Talks Stephen, A. Winfried, T. Katherine, and S. Sobha, "Retinal vein occlusion (RVO) guideline: executive summary," *Eye*, vol. 36, no. 5, pp. 909–912, 2022.

[9] S. Cugati, J. J. Wang, E. Rochtchina, and P. Mitchell, "Ten-year incidence of retinal vein occlusion in an older population," *Archives of Ophthalmology*, vol. 124, no. 5, pp. 726–732, 2006.

[10] M. P. Sindhu, "Exudate extraction from fundus images using machine learning," *International Journal of Biomedical and Clinical Engineering*, vol. 11, no. 1, pp. 1–16, 2022.

[11] Y. S. Goker, C. U. Atılgan, K. Tekin et al., "Association between disorganization of the retinal inner layers and capillary non-perfusion area in patients with retinal vein occlusion," *Arquivos Brasileiros de Oftalmologia*, vol. 83, pp. 497–504, 2020.

[12] S. Alqadri, M. M. Adil, M. Watanabe, and A. I. Qureshi, "Patterns of collateral formation in basilar artery steno-occlusive diseases," *Journal of Vascular and Interventional Neurology*, vol. 6, no. 2, pp. 9–13, 2013.

[13] R. Murugan and P. Roy, "MicroNet: microaneurysm detection in retinal fundus images using convolutional neural network," *Soft Computing*, vol. 26, no. 3, pp. 1057–1066, 2022.

[14] E. A. Hamed, H. A. Elwakeel, H. A. Eldin, Y. M. BedierElkiran, and M. F. Kamel, "Chemical and mechanochemical catheter-directed sclerotherapy in varicose vein ablation," *The Egyptian Journal of Surgery*, vol. 40, no. 1, pp. 90–98, 2021.

[15] M. Suzani and A. T. Moore, "Coats disease: fluorescein angiography guided management," *Acta Ophthalmologica*, vol. 90, 2012.

[16] T. Wu, L. Liting, Z. Tianer, and W. Xuesen, "Deep learning-based risk classification and auxiliary diagnosis of macular edema," *Intelligence-Based Medicine*, vol. 6, article 100053, 2022.

[17] S. R. Singh, D. C. Parameswarappa, V. Govindahari, M. Lupidi, and J. Chhablani, "Clinical and angiographic characterization of choroidal neovascularization in diabetic retinopathy," *European Journal of Ophthalmology*, vol. 31, no. 2, pp. 584–591, 2021.

[18] J. Shilpa and P. T. Karule, "Haemorrhages detection using geometrical techniques," *Computer Methods in Biomechanics and Biomedical Engineering: Imaging & Visualization*, vol. 8, no. 4, pp. 436–445, 2020.

[19] G. T. Frangieh, W. R. Green, E. Barraquer-Somers, and D. Finkelstein, "Histopathologic study of nine branch retinal vein occlusions," *Archives of Ophthalmology*, vol. 100, no. 7, pp. 1132–1140, 1982.

[20] W. R. Green, C. C. Chan, G. M. Hutchins, and J. M. Terry, "Central retinal vein occlusion: a prospective histopathologic study of 29 eyes in 28 cases," *Retina*, vol. 1, no. 1, pp. 27–55, 1981.

[21] P. Song, Y. Xu, M. Zha, Y. Zhang, and I. Rudan, "Global epidemiology of retinal vein occlusion: a systematic review and meta-analysis of prevalence, incidence, and risk factors," *Journal of Global Health*, vol. 9, no. 1, article 010427, 2019.

[22] M. Laouri, E. Chen, M. Looman, and M. Gallagher, "The burden of disease of retinal vein occlusion: review of the literature," *Eye*, vol. 25, no. 8, pp. 981–988, 2011.

[23] S. Sivaprasad, W. M. Amoaku, P. Hykin, and RVO Guideline Group, "The Royal College of Ophthalmologists guidelines on retinal vein occlusions: executive summary," *Eye*, vol. 29, no. 12, pp. 1633–1638, 2015.

[24] M. Sun, X. F. Hao, L. K. Xie, Q. Jin, S. H. Wang, and J. Xu, "Methods for making animal models of retinal vein occlusion," *International Eye Research*, vol. 2, no. 3, pp. 164–169, 2021.

[25] I. L. McAllister, "Central retinal vein occlusion: a review," *Clinical & Experimental Ophthalmology*, vol. 40, no. 1, pp. 48–58, 2012.

[26] S. Suthaharan, "Machine Learning Models and Algorithms for Big Data Classification," in *Integrated Series in Information Systems*, pp. 289–307, Springer, New York, NY USA, 2016.

[27] G. Litjens, T. Kooi, B. E. Bejnordi et al., "A survey on deep learning in medical image analysis," *Medical Image Analysis*, vol. 42, pp. 60–88, 2017.

[28] Y. LeCun, B. Boser, J. S. Denker et al., "Backpropagation applied to handwritten zip code recognition," *Neural Computation*, vol. 1, no. 4, pp. 541–551, 1989.

[29] A. Krizhevsky, I. Sutskever, and G. E. Hinton, "Imagenet classification with deep convolutional neural networks," *Communications of the ACM*, vol. 60, pp. 84–90, 2017.

[30] M. Voets, K. Møllersen, and L. A. Bongo, "Replication study: development and validation of deep learning algorithm for detection of diabetic retinopathy in retinal fundus photographs," 2018, arXiv preprint arXiv:1803.04337.

[31] H. Zhang, Z. Chen, Z. Chi, and H. Fu, "Hierarchical local binary pattern for branch retinal vein occlusion recognition with fluorescein angiography images," *Electronics Letters*, vol. 50, no. 25, pp. 1902–1904, 2014.

[32] R. Zhao, Z. Chen, and Z. Chi, "Convolutional neural networks for branch retinal vein occlusion recognition," in *Proceeding of the 2015 IEEE International Conference on Information and Automation*, pp. 1633–1636, Lijiang, China, 2015.

[33] E. Zahra, B. Ali, and W. Siddique, "Medical image segmentation using a U-Net type of architecture," 2020, arXiv preprint arXiv:2005.05218.

[34] C. Wan, X. Zhou, Q. You et al., "Retinal image enhancement using cycle-constraint adversarial network," *Frontiers in Medicine*, vol. 8, article 793726, 2022.

[35] Q. Chen, W. H. Yu, S. Lin et al., "Artificial intelligence can assist with diagnosing retinal vein occlusion," *International Journal of Ophthalmology*, vol. 14, no. 12, pp. 1895–1902, 2021.

[36] S. Heung-II, *Deep Learning for Medical Analysis*, K. Zhou, Ed., Elsevier Inc, 2017.

[37] P. Li, N. Yi, C. Ding, L. I. Sheng, and H. Min, "Research on classification diagnosis model of psoriasis based on deep residual," *Digital Chinese Medicine*, vol. 4, no. 2, pp. 92–101, 2021.

[38] C. Jianfang, Y. Minmin, J. Yiming, T. Xiaodong, and Z. Zibang, "Application of a modified Inception-v3 model in the dynasty-based classification of ancient murals," *EURASIP Journal on Advances in Signal Processing*, vol. 2021, no. 1, 2021.

[39] A. Michele, V. Colin, and D. D. Santika, "MobileNet Convolutional Neural Networks and Support Vector Machines for Palmprint Recognition," *Procedia Computer Science*, vol. 157, pp. 110–117, 2019.

[40] M. Sharma, B. Jain, C. Kargeti, V. Gupta, and D. Gupta, "Detection and diagnosis of skin diseases using residual neural networks (RESNET)," *International Journal of Image and Graphics*, vol. 21, no. 5, 2021.

[41] C. Szegedy, V. Vanhoucke, S. Ioffe, J. Shlens, and Z. Wojna, "Rethinking the inception architecture for computer vision," in *2016 IEEE Conference on Computer Vision and Pattern Recognition*, pp. 2818–2826, Las Vegas, NV, USA, 2016.

[42] A. G. Howard, M. Zhu, B. Chen et al., "MobileNets: efficient convolutional neural networks for mobile vision applications," *Computer Vision and Pattern Recognition*, vol. 1, pp. 1–9, 2017.

[43] K. Simonyan and A. Zisserman, "Very deep convolutional networks for large-scale image recognition," 2014, arXiv preprint arXiv: 1409.1556.

[44] M. Lin, Q. Chen, and S. Yan, "Network in network," 2013, arXiv preprint arXiv:1312.4400.

[45] A. M. Reza, "Realization of the contrast limited adaptive histogram equalization (CLAHE) for real-time image enhancement," *Journal of Vlsi Signal Processing Systems for Signal, Image and Video Technology*, vol. 38, no. 1, pp. 35–44, 2004.

[46] J. Yosinski, J. Clune, Y. Bengio, and H. Lipson, "How transferable are features in deep neural networks?," *Advances in Neural Information Processing Systems*, vol. 27, pp. 3320–3328, 2014.

[47] S. J. Pan and Q. Yang, "A survey on transfer learning," *IEEE Transactions on Knowledge and Data Engineering*, vol. 22, no. 10, pp. 1345–1359, 2010.

[48] C.-Y. Tai, W. Meng-Ru, Y.-W. Chu, and S.-Y. Chu, "GraphSW: a training protocol based on stage-wise training for GNN-based recommender model," 2019, arXiv preprint arXiv:1908.05611.

[49] E. Barshan and P. Fieguth, "Stage-wise training: an improved feature learning strategy for deep models," *Feature Extraction: Modern Questions and Challenges*, vol. 44, pp. 49–59, 2015.

Hindawi
Disease Markers
Volume 2022, Article ID 6066291, 7 pages
https://doi.org/10.1155/2022/6066291

Research Article

The Role of Pulmonary Function Test for Pulmonary Arterial Hypertension in Patients with Connective Tissue Disease

Jiangbiao Xiong, Jianbin Li, Yiping Huang, Fan Yang, and Rui Wu

The First Affiliated Hospital of Nanchang University, Nanchang 330006, China

Correspondence should be addressed to Rui Wu; tcmclinic@163.com

Received 23 June 2022; Revised 10 August 2022; Accepted 1 September 2022; Published 29 September 2022

Academic Editor: Qi-Chen Yang

Objective: The study aimed to investigate the value of pulmonary function test (PFT) in evaluating and predicting pulmonary arterial hypertension (PAH) in patients with connective tissue disease (CTD). *Methods*: This was a prospective observational study recruiting patients diagnosed with CTD-PAH. Patients with interstitial lung disease and pulmonary hypertension induced by other causes were not eligible for enrollment. All patients were assessed for PAH every 1–3 months. A patient was considered to have clinical improvement if the grade of risk stratification declined or at least two parameters improved during follow-up, otherwise no improvement. *Results*: A total of 31 patients with CTD-PAH were recruited in this study. Nearly 70% of patients had declined forced vital capacity (FVC), 60% had declined total lung capacity and maximum expiratory flow at 50% of vital capacity, and 95% had normal or mild decline in forced expiratory volume in 1 second (FEV1)/FVC. A decline in diffusing capacity of the lung for carbon monoxide (DLCO) was present in 96% of patients, and 60% were moderate to severe. Furthermore, 50% of patients had an FVC/DLCO ratio of less than 1.4. Univariate analysis showed that FEV1/FVC, DLCO, and FVC/DLCO were associated with disease prognosis. After adjusting for age as a confounding factor, multivariate logistic regression analysis revealed that DLCO was an independent predictive factor for the prognosis of CTD-PAH. *Conclusion*: The pulmonary function of patients with CTD-PAH is abnormal in parameters such as lung volume, small airway, and gas exchange. PFT can reveal complex pathophysiological changes in the lungs of CTD-PAH patients and predict prognosis.

1. Introduction

Pulmonary hypertension (PH) refers to a pathophysiological syndrome of right heart failure caused by a variety of etiologies that cause pulmonary vascular bed involvement to progressively increase pulmonary circulatory resistance [1]. Among many causes of PH, connective tissue disease-associated pulmonary arterial hypertension (CTD-PAH) accounts for about 25% [2]. PAH is one of the serious complications of CTDs [3]. Compared with idiopathic pulmonary arterial hypertension (IPAH), patients with CTD-PAH have a worse prognosis [4]. Early identification, regular assessment, and targeted treatment are important strategies to improve the prognosis of PAH [5, 6]. Right heart catheterization (RHC) is the gold standard for the diagnosis of PAH, but it is not suitable for the screening and evaluation of PAH because of its invasiveness and complicated operation [7]. Echocardiography is usually used clinically as the primary screening method for PAH, but there are certain differences compared with the results of RHC [8–11]. In PAH, pulmonary vascular endothelial proliferation, thickening of the vascular wall, and reduction of pulmonary vascular bed can lead to a decrease in diffusing capacity of the lung for carbon monoxide (DLCO), and the decline in DLCO is related to the severity of PAH [12, 13]. It is generally believed that PAH does not have ventilatory disorders [14]. Therefore, pulmonary function test (PFT) is recommended as a simple and easy auxiliary screening method

for PAH [15]. However, some studies have found that peripheral small airway obstruction is common in all types of PH, including CTD-PAH [16–18]. The higher the World Health Organization functional class (WHO FC), the more serious the peripheral small airway obstruction [18]. In addition, there are studies showing that PAH has restrictive ventilation difficulties [19]. Although many studies believe that the decline of DLCO can be used as a clue for screening PAH, Mukerjee, George, and Knight believe that DLCO lacks sensitivity and specificity in systemic sclerosis (SSc)-associated PAH [20]. This study aimed to investigate the value of PFT in evaluating and predicting CTD-PAH.

2. Materials and Methods

2.1. Subjects and Study Design. This was a prospective observational study recruiting patients diagnosed with CTD-PAH at the First Affiliated Hospital of Nanchang University from January 2021 to July 2021. All enrolled patients met international diagnostic or classification criteria for different types of CTD [21, 22]. The diagnostic criteria for PAH were as follows: mean pulmonary arterial pressure (mPAP) >20 mmHg, pulmonary artery wedge pressure (PAWP) <15 mmHg, pulmonary vascular resistance (PVR) > 3 Wood units, measured by RHC, or systolic pulmonary arterial pressure (sPAP) ≥40 mmHg by transthoracic echocardiography [23]. Patients with interstitial lung disease (ILD) and PH induced by other causes, such as IPAH, congenital heart disease, chronic obstructive pulmonary disease, and pulmonary thromboembolism, were not eligible for enrollment. The study conformed to the principles of the Declaration of Helsinki and was approved by the Ethics Committee of the First Affiliated Hospital of Nanchang University. Written informed consent was obtained from all individual participants.

All patients were assessed for PAH every 1–3 months by including N-terminal prohormone of brain natriuretic peptide (NT-proBNP), PFT, echocardiography, 6-minute walking distance (6MWD), WHO FC, and risk stratification according to the 2015 European Society of Cardiology (ESC)/European Respiratory Society (ERS) Guidelines for the diagnosis and treatment of PH [24] and were followed up for 6 months. A patient was considered to have clinical improvement if the grade of risk stratification declined or at least two parameters improved during follow-up, otherwise no improvement.

2.2. PFT. The MasterScreen PFT System (Jaeger, Baglia, Germany) was used to measure the pulmonary function of patients. Parameters including forced vital capacity (FVC), forced expiratory volume in 1 second (FEV1), maximum expiratory flow at 50% of vital capacity (MEF50), total lung capacity (TLC), and DLCO were tested. The data were expressed as the percentage of the measured value to the predicted value, and the percentage <80% was considered abnormal.

2.3. Statistical Analysis. For statistical analysis, the SPSS version 22.0 (IBM, Armonk, NY, USA) and GraphPad Prism 9 (GraphPad Software, San Diego, CA, USA) were used. Continuous variables were expressed as the mean ± standard deviation for normally distributed data or the median [interquartile range (IQR)] for nonnormally distributed data. Categorical variables were described as a number and a percentage of the total. To compare the differences between two groups, we used the independent samples *t*-test or Mann–Whitney *U* test for continuous variables and the chi-square test or Fisher's exact test for categorical variables. A one-way analysis of variance (ANOVA) was employed to compare differences among three groups. Logistic regression analysis was used to analyze the predictive value of pulmonary function parameters for the prognosis of CTD-PAH.

Table 1: Baseline clinical characteristics of patients with CTD-PAH.

Characteristics	Value
Total number	31
SLE	22 (76.3%)
SSc	9 (23.7%)
Age (years)	42.32 ± 13.82
Female	30 (96.8%)
NT-proBNP (ng/L)	966.16 ± 906.13
Stabilization of CTD	21 (67.7%)
sPAP (mmHg)	47.84 ± 9.56
RAA (cm^2)	18.52 ± 2.51
RVBD (cm)	3.59 ± 1.42
RAP (mmHg)	9.03 ± 3.69
TAPSE (mm)	16.17 ± 3.24
6MWD (m)	381.26 ± 69.42
WHO FC	
I	6 (19.4%)
II	13 (41.9%)
III	9 (29.0%)
IV	3 (9.7%)
Risk stratification	
Low risk	8 (25.8%)
Intermediate risk	15 (48.4%)
High risk	8 (25.8%)
FVC (%)	78.56 ± 15.76
FEV1/FVC (%)	83.00 ± 10.65
MEF50 (%)	70.27 ± 31.29
TLC (%)	80.97 ± 13.44
DLCO (%)	56.84 ± 17.39
FVC/DLCO	1.52 ± 0.72

SLE: systemic lupus erythematosus; SSc: systemic sclerosis; CTD: connective tissue disease; NT-proBNP: N-terminal prohormone of brain natriuretic peptide; sPAP: systolic pulmonary arterial pressure; RAA: right atrial area; RVBD: right ventricular basal diameter; RAP: right atrial pressure; TAPSE: tricuspid annular plane systolic excursion; 6MWD: 6-minute walking distance; WHO FC: World Health Organization functional class; FVC: forced vital capacity; FEV1: forced expiratory volume in 1 second; MEF50: maximum expiratory flow at 50% of vital capacity; TLC: total lung capacity; DLCO: diffusing capacity of the lung for carbon monoxide.

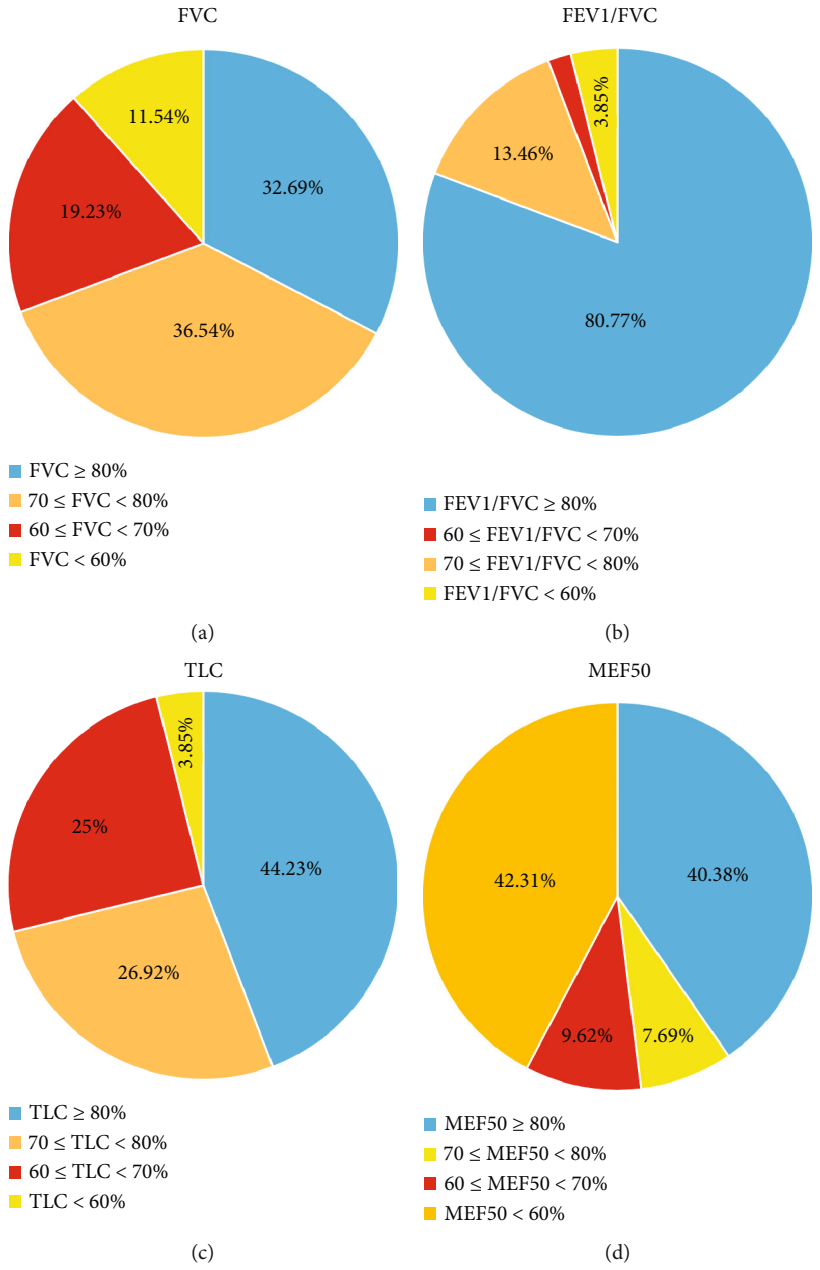

Figure 1: Continued.

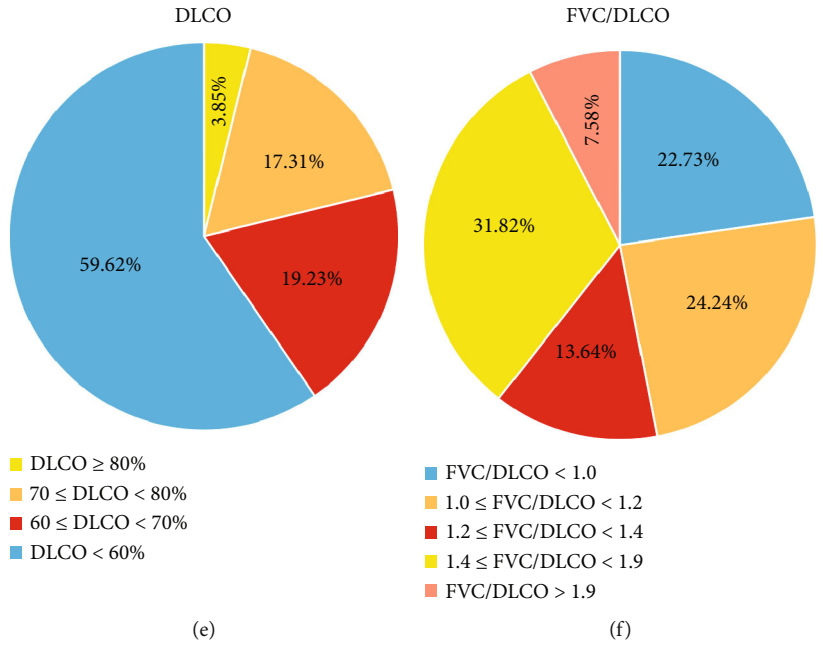

Figure 1: Pie chart of different pulmonary function parameters. FVC: forced vital capacity; FEV1: forced expiratory volume in 1 second; MEF50: maximum expiratory flow at 50% of vital capacity; TLC: total lung capacity; DLCO: diffusing capacity of the lung for carbon monoxide.

Table 2: Comparisons of pulmonary function parameters among different risk groups.

Parameters	Low risk	Intermediate risk	High risk	*P* value
FVC (%)	81.23 ± 15.20	76.80 ± 12.57	67.09 ± 22.31	0.104
FEV1/FVC (%)	85.03 ± 15.54	93.17 ± 8.65	83.03 ± 7.43	**0.029**
MEF50 (%)	69.88 ± 39.40	71.12 ± 26.32	35.81 ± 22.93	**0.021**
TLC (%)	82.25 ± 10.44	78.58 ± 11.29	74.59 ± 15.08	0.287
DLCO (%)	69.67 ± 7.62	48.89 ± 13.22	44.65 ± 16.44	**<0.001**
FVC/DLCO	1.18 ± 0.29	1.71 ± 0.74	1.52 ± 0.18	**0.014**

Bold values are statistically significant ($P < 0.05$). FVC: forced vital capacity; FEV1: forced expiratory volume in 1 second; MEF50: maximum expiratory flow at 50% of vital capacity; TLC: total lung capacity; DLCO: diffusing capacity of the lung for carbon monoxide.

All statistical tests were two-tailed, and p value < 0.05 was considered statistically significant.

3. Results

3.1. Baseline Characteristics. A total of 31 patients with CTD-PAH, including 22 patients with systemic lupus erythematosus (SLE) and 9 patients with systemic sclerosis (SSc), were recruited in this study. All patients were treated with PAH target therapy. Only 3 patients at low risk were treated with monotherapy, and the rest were treated with combination therapy. The baseline clinical characteristics were shown in Table 1.

As shown in Figure 1, nearly 70% of patients had declined FVC, 60% had declined TLC and MEF50, and 95% had a normal or mild decline in FEV1/FVC. A decline in DLCO was present in 96% of patients, and 60% were moderate to severe. Furthermore, 50% of patients had an FVC/DLCO ratio of less than 1.4.

3.2. Comparisons of Pulmonary Function Parameters among Different Risk Groups. The ANOVA test indicated that FEV1/FVC, MEF50, DLCO, and FVC/DLCO were significantly different among low risk, intermediate risk, and high risk groups (Table 2). In particular, DLCO declined significantly with the rise of risk stratification of PAH, while FEV1/FVC and FVC/DLCO were also significantly different among different risk groups, but there was no declining trend. Multiple comparisons showed that there was no significant difference in MEF50 between the low and intermediate risk groups, but there was a significant decline in the high risk group compared with the lower risk group.

3.3. Predictive Value of Pulmonary Function Parameters. After 6 months of follow-up in all patients, 17 patients were clinically improved and 14 were not. Univariate analysis showed that FEV1/FVC, DLCO, and FVC/DLCO were associated with disease prognosis (Table 3). After adjusting for age as a confounding factor, multivariate logistic regression

Table 3: Comparisons of pulmonary function parameters between groups with and without improvement.

Parameters	Group without improvement ($n = 14$)	Group with improvement ($n = 17$)	P value
FVC (%)	74.21 ± 19.34	79.01 ± 11.85	0.558
FEV1/FVC (%)	90.09 ± 7.67	87.57 ± 14.80	**0.020**
MEF50 (%)	57.24 ± 30.81	71.64 ± 34.09	0.553
TLC (%)	75.03 ± 13.71	82.71 ± 8.54	0.058
DLCO (%)	43.13 ± 13.20	65.76 ± 9.47	**0.001**
FVC/DLCO	1.82 ± 0.72	1.22 ± 0.25	**0.002**

Bold values are statistically significant ($P < 0.05$). FVC: forced vital capacity; FEV1: forced expiratory volume in 1 second; MEF50: maximum expiratory flow at 50% of vital capacity; TLC: total lung capacity; DLCO: diffusing capacity of the lung for carbon monoxide.

Table 4: Logistic regression analysis for the predictive value of pulmonary function parameters.

Parameters	OR	95% CI	P value
TLC (%)	0.911	0.817–1.017	0.096
FEV1/FVC (%)	1.044	0.950–1.147	0.371
DLCO (%)	4.813	1.039–22.300	**0.045**

OR: odds ratio; 95% CI: 95% confidence interval. Bold values are statistically significant ($P < 0.05$). FVC: forced vital capacity; FEV1: forced expiratory volume in 1 second; DLCO: diffusing capacity of the lung for carbon monoxide.

analysis revealed that DLCO was an independent predictive factor for the prognosis of CTD-PAH [odds ratio (OR) 4.813, 95% confidence interval (CI) 1.039–22.300] (Table 4).

4. Discussion

CTD-PAH belongs to group I of PH, and its pathophysiological changes are pulmonary vascular endothelial dysfunction, vascular remodeling, and progressive occlusion of small pulmonary arteries <200 μm in diameter [25, 26]. PFT can reflect the information of various physiological and pathological changes of the lung, including the ventilation function of the airway and the gas exchange function of the vascular interstitium [18]. The relationship between group I of PH and parameters related to pulmonary ventilation function is still controversial, but the decline of DLCO, a parameter reflecting gas exchange function, is considered to be a characteristic change of pulmonary function in most patients with PAH [27, 28]. The decline in DLCO is the comprehensive result of endothelial cell proliferation leading to thickening of alveolar capillary membranes, increased PVR leading to decreased pulmonary vascular blood volume, decreased right ventricular output, and local thrombosis [29]. In this study, 96% of patients with CTD-PAH had a decline in DLCO, and 60% of patients had a DLCO below 60%. Moreover, DLCO declined with rising risk stratification. Importantly, multivariate analysis found that DLCO was an independent predictive factor for the prognosis of CTD-PAH.

Studies have shown that TLC in 20–50% of patients with IPAH decline, but some studies have not found it [30]. This study indicated that 60% of CTD-PAH patients had declined FVC and TLC. The reason for lung volume limitation in patients with PAH remains unclear. One explanation is that pulmonary vascular enlargement may have a direct physical effect on the airway, limiting tracheal dilation by mechanical pressure on the airway [31]. In addition to the factors of enlarged pulmonary vessels, the subsequent enlargement of the atria and ventricles may lead to the displacement of lung tissue within the thoracic cavity and affect the lung volume [32]. Most studies show that FEV1/FVC is normal in group I of PH [33]. This study showed that 95% of patients with CTD-PAH had an FEV1/FVC above 70%. Nevertheless, it is not sufficient to conclude that there is no airway obstruction in PAH, because FEV1 does not change much when small airways are obstructed, and extensive small airway obstruction only causes a small decline in FEV1. This study showed that MEF50, a sensitive marker of small airway, declined in 60% of patients with CTD-PAH, of which 42% had a MEF50 below 60%. Moreover, the MEF50 in the high risk group was significantly lower than that in the low risk group, while there was no significant difference between the low and intermediate risk groups, suggesting that small airway obstruction was more common in CTD-PAH patients with high risk stratification [34]. As with lung volume, the cause of obstruction of the small airways in patients with PAH is also unclear. A possible histological explanation is that pulmonary artery thickening invades the adjacent airways, impairing airflow and causing airway obstruction [31, 32]. Some studies have also suggested that inflammatory cytokines in lung tissue not only play a role in pulmonary vascular remodeling but may also overflow from vessels to the airways, resulting in airway inflammation [35, 36]. Some substances that play a key role in the pathogenesis of PH, such as endothelin-1 and nitric oxide, can also affect the contraction and dilation of bronchi in vivo and vitro [37, 38]. We also observed improvement in TLC and FEV1/FVC after treatment of PAH, suggesting that the decrease in TLC and FEV1/FVC were related to PAH.

Some studies suggest that patients with PAH can have a mild decrease in FVC, but the decline in DLCO should be more significant [18]. Meanwhile, FVC and DLCO decreased synchronously in patients with ILD. Therefore, it is recommended to use FVC/DLCO to differentiate PAH from ILD. When FVC/DLCO is less than 1.4, the possibility of ILD is high, and when it is greater than 2, the diagnosis of PAH should be taken into consideration [39]. There are also studies finding that FVC/DLCO greater than 1.9 has a sensitivity and specificity of 87.5% and 100% in predicting PAH [40]. However, the results of this study showed that the FVC/DLCO of more than half of the patients with CTD-PAH was below 1.4, and only 10% of the patients had a ratio above 1.9, suggesting that the value of FVC/DLCO as a predictor of PAH is limited.

The study has several limitations. First, different types of CTD have different mechanisms of PAH, resulting in no significant difference in FVC/DLCO in this study. Second, only two types of CTD-PAH were included, which may lead to biased results. Third, the sample size was not large enough. A large-scale and multicenter study is needed in the future.

5. Conclusion

The pulmonary function of patients with CTD-PAH is abnormal in parameters such as lung volume, small airway, and gas exchange. PFT can reveal complex pathophysiological changes in the lungs of CTD-PAH patients and predict prognosis. Exploring the mechanism of abnormal pulmonary function may provide new directions for the treatment of CTD-PAH.

Data Availability

The data used to support the findings of this study will be available from the corresponding author upon reasonable request.

Conflicts of Interest

The authors declare that there are no conflicts of interest.

Authors' Contributions

Jiangbiao Xiong and Jianbin Li contributed equally to this work.

Acknowledgments

We would like to thank Zoe Zeng for her help with language editing.

References

[1] R. Savai, S. S. Pullamsetti, J. Kolbe et al., "Immune and inflammatory cell involvement in the pathology of idiopathic pulmonary arterial hypertension," *American Journal of Respiratory and Critical Care Medicine*, vol. 186, no. 9, pp. 897–908, 2012.

[2] D. B. Badesch, G. E. Raskob, C. G. Elliott et al., "Pulmonary arterial hypertension: baseline characteristics from the REVEAL Registry," *Chest*, vol. 137, no. 2, pp. 376–387, 2010.

[3] R. L. Rhee, N. B. Gabler, S. Sangani, A. Praestgaard, P. A. Merkel, and S. M. Kawut, "Comparison of treatment response in idiopathic and connective tissue disease-associated pulmonary arterial hypertension," *American Journal of Respiratory and Critical Care Medicine*, vol. 192, no. 9, pp. 1111–1117, 2015.

[4] S. Gaine, K. Chin, G. Coghlan et al., "Selexipag for the treatment of connective tissue disease-associated pulmonary arterial hypertension," *European Respiratory Journal*, vol. 50, no. 2, p. 1602493, 2017.

[5] R. L. Benza, D. P. Miller, M. Gomberg-Maitland et al., "Predicting survival in pulmonary arterial Hypertension," *Circulation*, vol. 122, no. 2, pp. 164–172, 2010.

[6] H. W. Farber, D. P. Miller, A. D. Poms et al., "Five-year outcomes of patients enrolled in the REVEAL Registry," *Chest*, vol. 148, no. 4, pp. 1043–1054, 2015.

[7] M. D'Alto, K. Dimopoulos, J. G. Coghlan, G. Kovacs, S. Rosenkranz, and R. Naeije, "Right heart catheterization for the diagnosis of pulmonary hypertension: controversies and practical issues," *Heart Failure Clinics*, vol. 14, no. 3, pp. 467–477, 2018.

[8] E. Bossone, A. D'Andrea, M. D'Alto et al., "Echocardiography in pulmonary arterial hypertension: from diagnosis to prognosis," *Journal of the American Society of Echocardiography*, vol. 26, no. 1, pp. 1–14, 2013.

[9] E. Hachulla, V. Gressin, L. Guillevin et al., "Early detection of pulmonary arterial hypertension in systemic sclerosis: a French nationwide prospective multicenter study," *Arthritis and Rheumatism*, vol. 52, no. 12, pp. 3792–3800, 2005.

[10] J. D. Rich, S. J. Shah, R. S. Swamy, A. Kamp, and S. Rich, "Inaccuracy of Doppler echocardiographic estimates of pulmonary artery pressures in patients with pulmonary hypertension: implications for clinical practice," *Chest*, vol. 139, no. 5, pp. 988–993, 2011.

[11] J. Xiong, S. Yu, R. Liu, X. Fang, and R. Wu, "The role of conjunctival microvasculation combined with echocardiography in evaluating pulmonary arterial hypertension in systemic lupus erythematosus," *Disease Markers*, vol. 2021, Article ID 2135942, 6 pages, 2021.

[12] D. Launay, D. Montani, P. M. Hassoun et al., "Clinical phenotypes and survival of pre-capillary pulmonary hypertension in systemic sclerosis," *PLoS One*, vol. 13, no. 5, article e0197112, 2018.

[13] Y. Jiang, M. A. Turk, and J. E. Pope, "Factors associated with pulmonary arterial hypertension (PAH) in systemic sclerosis (SSc)," *Autoimmunity Reviews*, vol. 19, no. 9, article 102602, 2020.

[14] P. M. Escribano, M. A. Sánchez, M. J. de Atauri, J. P. Frade, and I. M. García, "Lung function testing in patients with pulmonary arterial hypertension," *Archivos de Bronconeumología*, vol. 41, no. 7, pp. 380–384, 2005.

[15] R. Cogswell, M. Pritzker, and T. De Marco, "Performance of the REVEAL pulmonary arterial hypertension prediction model using non-invasive and routinely measured parameters," *Journal of Heart and Lung Transplantation*, vol. 33, no. 4, pp. 382–387, 2014.

[16] A. Low, S. George, L. Howard, N. Bell, A. Millar, and R. M. R. Tulloh, "Lung function, inflammation, and endothelin-1 in congenital heart disease-associated pulmonary arterial hypertension," *Journal of the American Heart Association*, vol. 7, no. 4, 2018.

[17] R. Schiess, O. Senn, M. Fischler et al., "Tobacco Smoke: A Risk Factor for Pulmonary Arterial Hypertension?: A Case- Control Study," *Chest*, vol. 138, no. 5, pp. 1086–1092, 2010.

[18] Z. C. Jing, X. Q. Xu, D. B. Badesch et al., "Pulmonary function testing in patients with pulmonary arterial hypertension," *Respiratory Medicine*, vol. 103, no. 8, pp. 1136–1142, 2009.

[19] X. Sun, J. Hansen, R. Oudiz, and K. Wasserman, "Pulmonary function in primary pulmonary hypertension," *Journal of the American College of Cardiology*, vol. 41, no. 6, pp. 1028–1035, 2003.

[20] D. Mukerjee, D. St George, C. Knight et al., "Echocardiography and pulmonary function as screening tests for pulmonary arterial hypertension in systemic sclerosis," *Rheumatology*, vol. 43, no. 4, pp. 461–466, 2004.

[21] M. Petri, A. M. Orbai, G. S. Alarcón et al., "Derivation and validation of the Systemic Lupus International Collaborating

Clinics classification criteria for systemic lupus erythematosus," *Arthritis and Rheumatism*, vol. 64, no. 8, pp. 2677–2686, 2012.

[22] F. van den Hoogen, D. Khanna, J. Fransen et al., "2013 classification criteria for systemic sclerosis: an American college of rheumatology/European league against rheumatism collaborative initiative," *Annals of the Rheumatic Diseases*, vol. 72, no. 11, pp. 1747–1755, 2013.

[23] M. M. Hoeper, H. J. Bogaard, R. Condliffe et al., "Definitions and diagnosis of pulmonary hypertension," *Journal of the American College of Cardiology*, vol. 62, no. 25, pp. D42–D50, 2013.

[24] N. Galiè, M. Humbert, J. L. Vachiery et al., "2015 ESC/ERS Guidelines for the diagnosis and treatment of pulmonary hypertension: the Joint Task Force for the Diagnosis and Treatment of Pulmonary Hypertension of the European Society of Cardiology (ESC) and the European Respiratory Society (ERS): Endorsed by: Association for European Paediatric and Congenital Cardiology (AEPC), International Society for Heart and Lung Transplantation (ISHLT)," *European Respiratory Journal*, vol. 46, no. 4, pp. 903–975, 2015.

[25] P. Dorfmüller and M. Humbert, "Progress in pulmonary arterial hypertension pathology: relighting a torch inside the tunnel," *American Journal of Respiratory and Critical Care Medicine*, vol. 186, no. 3, pp. 210–212, 2012.

[26] R. Tuder, "Pathology of pulmonary arterial hypertension," *Seminars in Respiratory and Critical Care Medicine*, vol. 30, no. 4, pp. 376–385, 2009.

[27] E. Diamanti, V. Karava, P. Yerly, and J. D. Aubert, "Carbon monoxide diffusion capacity as a severity marker in pulmonary hypertension," *Journal of Clinical Medicine*, vol. 11, no. 1, p. 132, 2022.

[28] V. K. Bournia, A. Kallianos, S. Panopoulos et al., "Cardiopulmonary exercise testing and prognosis in patients with systemic sclerosis without baseline pulmonary hypertension: a prospective cohort study," *Rheumatology International*, vol. 42, no. 2, pp. 303–309, 2022.

[29] G. I. Heiden, J. B. Sobral, C. S. G. Freitas et al., "Mechanisms of exercise limitation and prevalence of pulmonary hypertension in pulmonary Langerhans cell histiocytosis," *Chest*, vol. 158, no. 6, pp. 2440–2448, 2020.

[30] F. J. Meyer, R. Ewert, M. M. Hoeper et al., "Peripheral airway obstruction in primary pulmonary hypertension," *Thorax*, vol. 57, no. 6, pp. 473–476, 2002.

[31] S. H. Park, S. Y. Park, N. K. Kim et al., "Bronchial compression in an infant with isolated secundum atrial septal defect associated with severe pulmonary arterial hypertension," *Korean Journal of Pediatrics*, vol. 55, no. 8, pp. 297–300, 2012.

[32] C. Pedone, S. Scarlata, D. Chiurco, M. E. Conte, F. Forastiere, and R. Antonelli-Incalzi, "Association of reduced total lung capacity with mortality and use of health services," *Chest*, vol. 141, no. 4, pp. 1025–1030, 2012.

[33] M. Sobiecka, K. Lewandowska, J. Kober et al., "Can a new scoring system improve prediction of pulmonary hypertension in newly recognised interstitial lung diseases?," *Lung*, vol. 198, no. 3, pp. 547–554, 2020.

[34] C. Ars, P. Thurion, M. Delos, Y. Sibille, and C. Pilette, "Small airway obstruction in severe pulmonary arterial hypertension correlates with increased airway CD8+ T-cells and fractalkine expression," *European Respiratory Journal*, vol. 34, no. 6, pp. 1494–1496, 2009.

[35] E. Soon, A. M. Holmes, C. M. Treacy et al., "Elevated levels of inflammatory cytokines predict survival in idiopathic and familial pulmonary arterial hypertension," *Circulation*, vol. 122, no. 9, pp. 920–927, 2010.

[36] A. S. Droste, D. Rohde, M. Voelkers et al., "Endothelin receptor antagonist and airway dysfunction in pulmonary arterial hypertension," *Respiratory Research*, vol. 10, no. 1, 2009.

[37] F. Bacakoğlu, A. Atasever, M. H. Ozhan, C. Gurgun, H. Ozkilic, and A. Guzelant, "Plasma and bronchoalveolar lavage fluid levels of endothelin-1 in patients with chronic obstructive pulmonary disease and pulmonary hypertension," *Respiration*, vol. 70, no. 6, pp. 594–599, 2003.

[38] N. S. Goh, S. Veeraraghavan, S. R. Desai et al., "Bronchoalveolar lavage cellular profiles in patients with systemic sclerosis-associated interstitial lung disease are not predictive of disease progression," *Arthritis and Rheumatism*, vol. 56, no. 6, pp. 2005–2012, 2007.

[39] R. Gupta, "Pulmonary function test as screening test for pulmonary artery hypertension in scleroderma patients," *Rheumatology*, vol. 43, no. 10, 2004.

[40] N. M. Riad, N. A. Morshedy, and A. M. Shoukri, "Role of pulmonary function tests in screening pulmonary arterial hypertension in scleroderma," *Egyptian Journal of Bronchology*, vol. 9, no. 3, pp. 287–292, 2015.

Hindawi
Disease Markers
Volume 2022, Article ID 5062591, 7 pages
https://doi.org/10.1155/2022/5062591

Research Article

Prognosis and Influencing Factors of Early Microsurgery for Severe Hypertensive Brainstem Hemorrhage

Xianbing Meng,[1] **Qian Wang**,[1] **Xianguang Pei**,[2] **and Fangmin Xie**[1]

[1]*The Second Affiliated Hospital of Shandong First Medical University, Taian, Shandong Province 271000, China*
[2]*The First Hospital of Handan City, Handan, Hebei Province 056002, China*

Correspondence should be addressed to Fangmin Xie; 1977_1@sina.com

Received 3 August 2022; Accepted 3 September 2022; Published 22 September 2022

Academic Editor: Yi Shao

Objective. To investigate the prognosis and influencing factors of early microsurgery for severe hypertensive brainstem hemorrhage. *Methods*. The clinical data of 19 patients with severe hypertensive brainstem hemorrhage treated in the Department of Neurosurgery of the Second Affiliated Hospital of Shandong First Medical University between January 2018 and December 2021 were retrospectively analyzed. The clinical efficacy and risk factors affecting the prognosis were analyzed by chi-square test and multivariate logistic regression. *Results*. A total of 19 patients with severe hypertensive brainstem hemorrhage were treated by early microsurgery, including 14 cases by subtemporal approach and 5 cases by retrosigmoid approach. After 3 months of follow-up, 6 patients died and 13 patients survived. The 30-day and 90-day mortality rates were 21.1% and 31.6%, respectively, and the good prognosis rate was 15.4%. Univariate analysis showed that hematoma volume and hematoma clearance rate might be the factors affecting the prognosis of patients with severe hypertensive brainstem hemorrhage; the observed difference was statistically significant ($P < 0.05$). Multivariate logistic regression analysis further confirmed that hematoma volume was an independent factor affecting the death of patients with brainstem hemorrhage ($P < 0.05$), while hematoma volume (B: 2.909, OR: 18.332, 95% CI: 1.020–329.458, P: 0.048) was a risk factor. *Conclusion*. Hematoma volume resulted as an independent factor affecting the death of patients with severe hypertensive brainstem hemorrhage. Early microsurgical clearance of brainstem hematoma contributed to reducing the 30-day and 90-day mortality and improving the prognosis of patients.

1. Introduction

Hypertensive brainstem hemorrhage (HBSH), which is characterized by acute onset, rapid progress, high mortality, and disability rate, is one of the most dangerous types of hemorrhagic stroke [1, 2]. According to previous studies, its annual incidence is about 2–4/100,000 [3, 4], and it mostly affects patients 40 to 60 years old, being more common in men than in women [2]. A hematoma usually forms rapidly after brainstem hemorrhage, leading to coma, central fever, tetraplegia, respiratory and circulatory failure, and other symptoms [2, 5, 6]. Conservative treatment can be used for patients with a small amount of brainstem hemorrhage and clear consciousness [7]; However, for patients with severe hypertensive brainstem hemorrhage (SHBSH) (bleeding volume >5 mL, GCS score <8 points), conservative treatment cannot effectively prevent the progress of the disease, and the mortality is as high as 80–100% [8]. Scholars in China and abroad have been working meticulously to improve the treatment of brainstem hemorrhage, reduce the mortality and disability rate, and improve the prognosis of patients.

Due to its complex anatomy, an important function, and high operation risk, the brainstem has long been regarded as the "forbidden area of neurosurgery" [9]. With the in-depth study of the anatomical structure and physiological function of the brainstem, it was confirmed that there is a relatively "safe operation area" in the brainstem [10–12]. Microsurgery is expected to become one of the most important ways to improve the prognosis of SHBSH patients [2, 11].

Nevertheless, whether surgical treatment could improve the prognosis of patients with brainstem hemorrhage still remains controversial [13, 14]. Rohde et al. [7] and Haines and Mollman [15] argued that patients with brainstem hemorrhage accompanied by instant coma and severe neurological deficit had a low probability of survival and were not suitable for surgical treatment. The United States and European Guidelines for Spontaneous Intracerebral Hemorrhage also do not recommend surgical treatment for patients with HBSH [16, 17]. Recent studies have reported that some patients with HBSH had their symptoms improved after microsurgical treatment [3, 4, 18, 19]. However, there are few reports on the microsurgical treatment of SHBSH, and its safety and effectiveness have not been fully elucidated. In this study, we retrospectively analyzed the data of 19 patients with SHBSH treated by microsurgery in the early stage and further discussed its clinical efficacy and risk factors affecting the prognosis of patients.

2. Materials and Methods

2.1. General Information. A total of 19 patients with SHBSH treated by microsurgery in the Department of Neurosurgery of the Second Affiliated Hospital of Shandong First Medical University from January 2018 to December 2021 were included in the study. There were 13 males and 6 females, with the age range from 32 to 64 years old and an average of 49.1 years old. Glasgow Coma Scale (GCS) showed 17 cases with 3–5 points and 2 cases with 6–8 points.

This study was approved by the ethics committee of the Second Affiliated Hospital of Shandong First Medical University, and the patients' families signed the informed consent.

2.2. Inclusion and Exclusion Criteria. Inclusion criteria were the following: (1) brainstem hematoma volume >5 ml confirmed by brain CT; (2) GCS score ≤8 points, with/without progressive aggravation of consciousness; (3) onset time ≤24 hours and stable circulation and respiration; and (4) complete clinical case data.

Exclusion criteria were (1) secondary brainstem hemorrhage caused by vascular malformation, cavernous hemangioma, metastasis, etc.; (2) GCS score of 3 points and unstable vital signs; and (3) complicated with important organ failure or coagulation disorders.

2.3. Imaging Examination. Brainstem hemorrhage was confirmed by brain computed tomography (CT) examination in all of the 19 patients, and the hemorrhage location was limited to the pons. According to the Tada formula [20], the amount of hemorrhage was calculated. The hematoma amount was 5–10 ml in 12 cases and ≥10 ml in 7 cases. Among them, 2 patients were complicated with acute obstructive hydrocephalus.

2.4. Surgical Analysis. All of the 19 patients were operated within 24 hours after onset. Before the operation, the location of the hematoma was determined based on brain CT scanning and MPR (multiplanar reformatting), and the individualized surgical approach was designed according to the anatomical location and expansion direction of the hematoma. Among these patients, 14 were managed by a subtemporal approach. During the operation, the tentorium cerebelli was incised to expose the lateral brainstem operation area, and the location of the brainstem hematoma was determined according to the condition. Next, the brainstem was incised longitudinally, and the hematoma clearance operation strictly limited in the hematoma cavity was performed under the microscope. The operation did not exceed the boundary of the hematoma in order to avoid brainstem injury as much as possible. In 5 cases with retrosigmoid approach, the location of the hematoma was identified under a microscope, and the lateral pontine was incised under direct vision to clear the brainstem hematoma. In case of active hemorrhage, low-power bipolar electrocoagulation was used to stop bleeding. When patients were combined with acute obstructive hydrocephalus, the lateral ventricle was drained first.

Table 1: The modified Rankin scale (mRS).

Level	Details of the modified Rankin scale
0	No symptoms.
1	No significant disability. Able to carry out all usual activities, despite some symptoms.
2	Slight disability. Able to look after own affairs without assistance, but unable to carry out all previous activities.
3	Moderate disability. Requires some help, but able to walk unassisted.
4	Moderately severe disability. Unable to attend to own bodily needs without assistance, and unable to walk unassisted.
5	Severe disability. Requires constant nursing care and attention, bedridden, incontinent.
6	Dead.

2.5. Efficacy Evaluation. The rehemorrhage rate, infection rate, and 30-day and 90-day survival rate of patients were analyzed after the operation. The patients were followed up for 1 and 3 months, respectively. The survival of patients was investigated, and the prognosis of surviving patients was evaluated by a modified Rankin scale (mRS) [21] (Table 1), where mRS ≤3 points indicated good prognosis and mRS with 4–6 points indicated poor prognosis.

2.6. Statistical Analysis. Statistical analyses were performed by SPSS software (version 25.0). The enumeration data were represented as a number of cases or rates. The chi-square test of the cross table was used to compare the differences in univariate analysis, after which the factors with statistical significance in the chi-square test were further analyzed with ordinal logistic regression. A P value <0.05 was considered to be statistically significant.

3. Results

3.1. The 30-Day and 90-Day Mortality in Patients with Brainstem Hemorrhage. Among the 19 patients with severe

Table 2: The 30-day and 90-day mortality in patients with brainstem hemorrhage.

	Number of cases (n)	Yes	No	Mortality rate (%)
30-Day mortality rate	$n = 19$	4	15	21.1
90-Day mortality rate	$n = 19$	6	13	31.6

hypertensive brainstem hemorrhage treated by microsurgery, 6 died and 13 survived. The 30-day and 90-day mortality rates were 21.1% and 31.6%, respectively (Table 2). The mRS score of 13 surviving patients was 4.08 ± 0.64 at 3 months of follow-up and 4.09 ± 0.70 at 6 months of follow-up. Among surviving patients, 2 had mRS score ≤ 3 points, and the good prognosis rate accounted for 15.4% of the total number.

3.2. Univariate Analysis of Prognosis of Patients with Brainstem Hemorrhage. Univariate analysis (Table 3) showed that the effects of factors including GCS score, onset-operation time, complicated with hydrocephalus, gender, age, and hematoma type had no significant difference on prognosis (all $P > 0.05$). However, the differences in the influence of hematoma volume and hematoma clearance rate on prognosis showed statistical significance ($P < 0.05$), suggesting that these factors might affect the prognosis of brainstem hemorrhage.

3.3. Multivariate Logistic Regression Analysis for the Prognosis of Patients with Brainstem Hemorrhage. Taking death (death/survival: 1/0) as the dependent variable and the hematoma volume (>10 ml/5–10 ml: 1/0) and hematoma clearance rate (≥80%/<80%: 1/0) as the independent variables for multivariate logistic regression analysis with the input method revealed that the independent factor affecting the death of patients with brainstem hemorrhage was the hematoma volume ($P < 0.05$), while the hematoma volume (B: 2.909, OR: 18.332, 95% CI: 1.020–329.458, P: 0.048) was also a risk factor (Table 4).

3.4. Typical Cases of Patients with Severe Brainstem Hemorrhage (Figure 1)

4. Discussion

HBSH accounts for 6–10% of all hypertensive intracerebral hemorrhages [14], with pons hemorrhage being the most common [22]. Hemorrhage mainly originates from the perforating artery of the paramedian branches supplying the brainstem [3]. Hypertension and atherosclerosis are the most common causes of brainstem hemorrhage [2, 9]. Previous studies suggested that the following are mechanisms of pathological injury caused by brainstem hemorrhage: First, the mechanical destruction of hematoma directly leads to the primary injury of the brainstem; second, the compression of hematoma leads to the secondary injury of the brainstem such as local tissue ischemia, edema, or inflammatory reaction caused by hematoma catabolic products [9]. It was previously confirmed that the necrosis of brain tissue around the hematoma begins within 6 hours of the onset of intracerebral hemorrhage, increases after 12 hours, and reaches the peak within 24 hours [23]. Therefore, the prompt clearance of the brainstem hematoma after the onset of SHBSH is essential for reducing the primary injury and preventing secondary injury, which is conducive to the protection of brainstem nerve function [9, 23].

Hematoma clearance by craniotomy and stereotaxis and/or navigation-guided hematoma puncture and drainage are the main surgical methods for treating PBSH [2, 9]. Early studies have reported that stereotaxis or navigation-guided puncture of brainstem hematoma could benefit some patients, but hematoma cannot be completely cleared with such an approach, and once the bleeding starts, it cannot be stopped under direct vision, thus limiting its application [24, 25]. Hematoma clearance by craniotomy is a classic surgical method of PBSH, which can be performed under direct vision, with accurate hemostatic effect and decompression at the same time [2]. The optimal approach is essential for successful brainstem hemorrhage surgery [2]. Due to the complex anatomical structure of the brainstem, the principle of the shortest approach and least injury must be followed when planning the surgical path so as to avoid iatrogenic injury [26]. In this study, we followed Brown's Rule [27], i.e., multiplanar reformatting of brain CT scanning was combined, and individualized surgical approaches were adopted. There were 14 cases of hematoma cleared by subtemporal approach and 5 cases by retrosigmoid approach. If it is suspected that the hematoma is located in the middle and upper ventrolateral part of the pons, the subtemporal approach can be adopted. During the operation, the temporal lobe was gently lifted to expose the superior petrosal sinus, and the tentorial edge of the cerebellum was cut so that the middle and upper sides of the pons could be reached. Through this area, it was possible to reach the focus quickly, and it was safer to cut the brainstem, which was consistent with the previous literature [19]. For patients with ventrolateral pontine hematoma, the retrosigmoid approach could be adopted, by which the supratrigeminal and lateral pontine safety entry zones could be reached [28]. The difficulty of hematoma clearance by craniotomy is the localization of brainstem hematoma during operation. If the hematoma breaks through the surface of the brainstem, a hematoma can be easily located and identified, and the cavity could be accessed through the break [9]. If the hematoma is close to the surface of the brainstem, color changes or local uplift occurs, and the hematoma cavity can be accessed by cutting the brainstem longitudinally in the local lesion [9, 19]. If the hematoma is confined to the brainstem tissue and there is no change on the surface, the hematoma cavity can be accessed through the safe entry zone [11, 12]. In addition, during the hematoma clearance, the brainstem supplying arteries and draining veins should be avoided as much as possible so as to avoid iatrogenic injury.

Whether microsurgery can improve the prognosis of SHBSH patients remains controversial. In their study, Lan et al. found that the mortality of SHBSH patients in the conservative treatment group was 70.42%, while that in the craniotomy group was 30.43% [8]. The mortality in this study

Table 3: Univariate analysis of prognosis of patients with brainstem hemorrhage.

	Death ($n = 6$)	Survival ($n = 13$)	Mortality rate (%)	P
GCS score				1.000
3–5 points	6	11	35.3	
≥6 points	0	2	0.0	
Hematoma volume				0.010
5–10 ml	1	11	8.3	
≥10 ml	5	2	71.4	
Operation time				0.605
7–24 h	1	5	16.7	
≤6 h	5	8	38.5	
Combined hydrocephalus				0.071
Yes	3	1	75.0	
No	3	12	20.0	
Age	44.67 ± 8.38	51.54 ± 6.89	—	0.076
Gender				0.320
Male	3	10	23.1	
Female	3	3	50.0	
Hematoma clearance rate				0.041
≥80%	1	10	9.1	
<80%	5	3	62.5	
Hematoma type				0.511
Bilateral tegmental type	3	5	37.5	
Massive type	1	1	50.0	
Basal tegmental type	2	3	40.0	
Unilateral tegmental type	0	4	0.0	
Complicated with hydrocephalus				1.000
No	5	12	29.4	
Yes	1	1	50.0	
Complicated with intracranial infection				—
No	6	13	31.6	
Yes	0	0	—	
Complicated with intracranial hemorrhage				0.222
No	4	12	25.0	
Yes	2	1	66.7	
Complicated with patient vegetative survival				1.000
No	5	11	31.3	
Yes	1	2	33.3	

Two independent sample t tests were used to compare the difference in age between death and survival groups, and Fisher's exact test was used to compare other indicators.

Table 4: Multivariate logistic regression analysis for the prognosis of patients with brainstem hemorrhage.

	B	SE	Wald	df	P	OR	95% CI for OR	
							Lower	Upper
Hematoma volume (ml)	2.909	1.474	3.895	1	0.048	18.332	1.020	329.458
Hematoma clearance rate 24 h	−2.329	1.501	2.407	1	0.121	0.097	0.005	1.846
Constant	−1.139	1.210	0.886	1	0.346	0.320		

was 31.6% (6/19), which was consistent with the previous literature report. Jang et al. reported that the 30-day mortality of patients with brainstem hemorrhage was 39.1%, the 90-day mortality was 49.8%, and the 90-day good function recovery rate was 9.6% [6]. The 30-day and 90-day mortality rates in this study were 21.1% and 31.6%, respectively, and the good

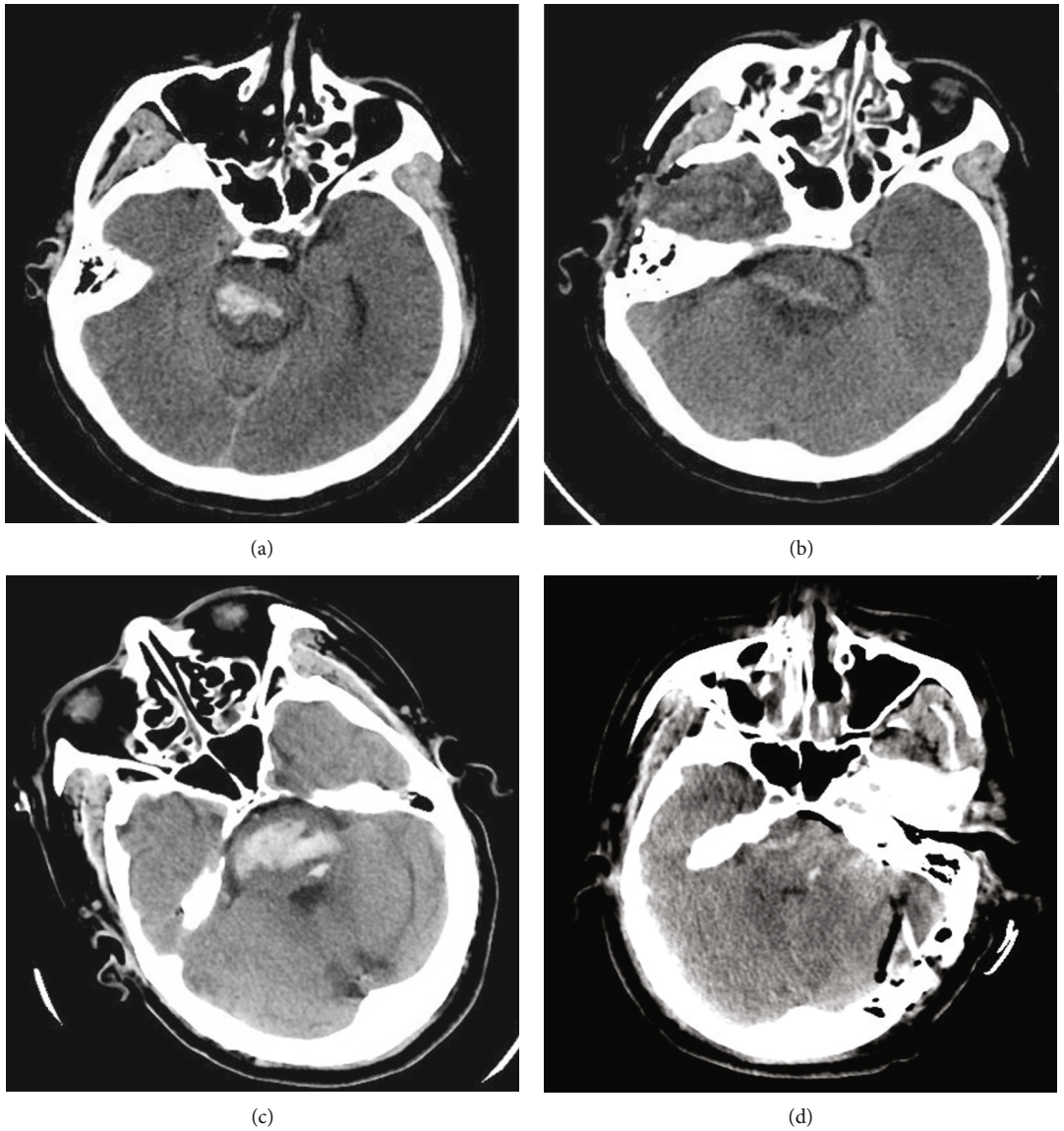

(a) (b) (c) (d)

Figure 1: Forty-eight years old, male, who was admitted to the hospital with sudden unconsciousness for 3 hours. Physical examination: The patient was in coma with respiratory failure and tracheal intubation. Bilateral pupils were 1.5 mm, and the light reflex was negative. The patient was quadriplegic and bilateral Babinski's sign positive. Preoperative brain CT showed that the brainstem hematoma was located in the upper part of the pons, which was of unilateral tegmental type (a). The hematoma was cleared by subtemporal approach. Brain CT at 24 hours after operation showed that pons hemorrhage was cleared satisfactorily (b). Fifty-four years old, male, admitted to the hospital with sudden unconsciousness for 1 hour. Physical examination: The patient was in coma with bilateral miosis and negative for light reflex. The patient presented with quadriplegia, hypotonia, and bilateral Babinski's sign positive. Preoperative brain CT showed that the hematoma was located in the middle and lower part of the pons, which was of bilateral tegmental type (c). The hematoma was cleared through the retrosigmoid sinus approach. Brain CT at 24 hours after operation showed that pons hematoma was completely cleared and the fourth ventricle was clear (d).

prognosis rate was 15.4% (2/19), which was better than the survival rate reported in the previous literature [6, 8].

Although previous studies argued that brainstem hemorrhage requires early surgery, there is no unified standard in China and abroad for the best timing of HBSH surgery. Lan et al. [8] found that the nervous system recovery in the early operation group (≤ 6 h) of PBSH patients was better than that in the late operation group (> 6 h), so they suggested that the best operation timing might be to receive surgical treatment within 6 hours after the onset of the disease. In their study, Chen et al. [3] retrospectively analyzed the data of 52 patients with brainstem hemorrhage and found that 12–48 hours after the onset of PBSH was the best timing for surgery. The consensus of Chinese experts recommends 6–24 h after hemorrhage as the best timing for surgery [9]. Some studies suggested that the surgery timing was an important factor affecting the prognosis of brainstem hemorrhage. Yet, our results revealed that the operation

timing was not statistically significant ($P > 0.05$), which was inconsistent with the previous studies, and may be related to the small sample size [8].

At present, the prognosis and influencing factors of hypertensive supratentorial hemorrhage have been well studied [16, 17]. However, brainstem hemorrhage-related studies are inadequate. Raison et al. believe that the prognosis of SHBSH patients depends on the location of hematoma, extent of hemorrhage, and the condition at the time of onset [29]. When the hematoma volume exceeds 10 ml, the mortality comes close to 100% [30]. Our results confirmed that the mortality of patients with hematoma volume >10 ml was 71.4% (5/7), and the mortality of patients with hematoma volume of 5–10 ml was <8.3% (1/11). Univariate analysis showed a significant difference in the influence of hematoma volume and hematoma clearance rate on prognosis ($P < 0.05$), suggesting that hematoma volume and hematoma clearance rate may be factors affecting the prognosis of brainstem hemorrhage. Multivariate logistic regression analysis confirmed that the hematoma volume was an independent factor affecting the death of patients with brainstem hemorrhage ($P < 0.05$), while the hematoma volume was a risk factor (P: 0.048). The results were consistent with those previously reported in the literature [29]. Chung and Park classified brainstem hemorrhage into four types based on the characteristics of brain CT imaging, of which the survival rate of unilateral tegmental hemorrhage was 94.1%; however, the survival rates of basal tegmental type, bilateral tegmental type, and giant type were 26.1%, 14.3%, and 7.1%, respectively [29]. In the present study, we found that the survival rate of patients with unilateral tegmental brainstem hemorrhage was close to 100%, and the other types had higher mortality, which was consistent with the previous literature reports. Other studies argued that the GCS score could be used as an independent risk factor for SHBSH death [19]. In this study, two patients with preoperative GCS score ≥6 points survived, while the mortality rate of 17 patients with a preoperative GCS score of 3 to 5 points was 35.3% (6/17). Univariate analysis showed that the GCS score had no statistical significance for the prognosis of patients with brainstem hemorrhage ($P = 1.000$), which was inconsistent with previous literature reports, and may be related to the small sample size in this study. According to previous studies, about 39.5% of PBSH broke into the ventricular system [2], and the incidence of hydrocephalus was as high as 30.3% when the hemorrhage was located around the fourth ventricle and midbrain aqueduct, with a significantly increased risk of death and poor prognosis [22, 31]. We found that the presence of hydrocephalus was not associated with surgical results ($P = 0.071$), which was inconsistent with the literature and could be attributed to the small sample size. In addition, it was confirmed that men were significantly more affected by brainstem hemorrhage than women; however, we found no significant difference in gender and age, which was consistent with the literature [22].

This study has a few limitations. This is a single-center, retrospective study with a small sample size and short follow-up time. Further prospective multicenter studies are needed to confirm the long-term efficacy.

In conclusion, early microsurgical treatment can reduce mortality and improve the prognosis of SHBSH patients.

Data Availability

The study data presented may be made available from the corresponding author upon reasonable request.

Conflicts of Interest

The author declares no conflict of interest.

Acknowledgments

This study was supported by the Science and Technology Research Project of the Shandong Geriatrics Association (No. LKJGG2021W095) and Tai'an Science and Technology Innovation and Development Project (policy guidance) (No. 2021NS267).

References

[1] S. Takeuchi, G. Suzuki, Y. Takasato et al., "Prognostic factors in patients with primary brainstem hemorrhage," *Clinical Neurology and Neurosurgery*, vol. 115, no. 6, pp. 732–735, 2013.

[2] D. Chen, Y. Tang, H. Nie et al., "Primary brainstem hemorrhage: a review of prognostic factors and surgical management," *Frontiers in Neurology*, vol. 12, article 727962, 2021.

[3] L. H. Chen, F. J. Li, H. T. Zhang, W. J. Chen, K. Sun, and R. X. Xu, "The microsurgical treatment for primary hypertensive brainstem hemorrhage: experience with 52 patients," *Asian Journal of Surgery*, vol. 44, no. 1, pp. 123–130, 2021.

[4] S. Ichimura, H. Bertalanffy, M. Nakaya et al., "Surgical treatment for primary brainstem hemorrhage to improve postoperative functional outcomes," *World Neurosurgery*, vol. 120, pp. e1289–e1294, 2018.

[5] Y. Iwasaki, M. Kinoshita, and K. Ikeda, "Primary pontine hemorrhage: clinico-computed tomographic correlations," *Computerized Medical Imaging and Graphics*, vol. 12, no. 6, pp. 365–370, 1988.

[6] J. H. Jang, Y. G. Song, and Y. Z. Kim, "Predictors of 30-day mortality and 90-day functional recovery after primary pontine hemorrhage," *Journal of Korean Medical Science*, vol. 26, no. 1, pp. 100–107, 2011.

[7] V. Rohde, E. Berns, I. Rohde, J. M. Gilsbach, and Y. M. Ryang, "Experiences in the management of brainstem hematomas," *Neurosurgical Review*, vol. 30, no. 3, pp. 219–224, 2007.

[8] Z. Lan, S. A. Richard, L. Hao, M. Chen, and C. You, "Spontaneous hypertensive brainstem hemorrhage: does surgery benefit the severe cases?," *Interdisciplinary Neurosurgery: Advanced Techniques and Case Management*, vol. 15, pp. 66–70, 2019.

[9] L. Chen, "Clinical neurorestorative therapeutic guideline for brainstem hemorrhage (2020 China version)," *Journal of Neurorestoratology*, vol. 8, no. 4, pp. 232–240, 2020.

[10] J. L. Serrato-Avila, J. A. P. Archila, M. D. S. da Costa et al., "Three dimensional quantitative analysis of the brainstem safe entry zones based on internal structures," *World Neurosurgery*, vol. 158, pp. e64–e74, 2021.

[11] A. Tayebi Meybodi, B. K. Hendricks, A. J. Witten, J. Hartman, S. B. Tomlinson, and A. A. Cohen-Gadol, "Virtual exploration of safe entry zones in the brainstem: comprehensive definition and analysis of the operative approach," *World Neurosurgery*, vol. 140, pp. 499–508, 2020.

[12] Y. Yang, B. van Niftrik, X. Ma et al., "Analysis of safe entry zones into the brainstem," *Neurosurgical Review*, vol. 42, no. 3, pp. 721–729, 2019.

[13] W. J. Zheng, S. W. Shi, and J. Gong, "The truths behind the statistics of surgical treatment for hypertensive brainstem hemorrhage in China: a review," *Neurosurgical Review*, vol. 45, pp. 1–10, 2022.

[14] S. S. Wang, Y. Yang, J. Velz et al., "Management of brainstem haemorrhages," *Swiss Medical Weekly*, vol. 149, article w20062, 2019.

[15] S. J. Haines and H. D. Mollman, "Primary pontine hemorrhagic events: hemorrhage or hematoma? Surgical or conservative management?," *Neurosurgery Clinics of North America*, vol. 4, no. 3, pp. 481–495, 1993.

[16] J. C. Hemphill 3rd, S. M. Greenberg, C. S. Anderson et al., "Guidelines for the management of spontaneous intracerebral hemorrhage," *Stroke*, vol. 46, no. 7, pp. 2032–2060, 2015.

[17] T. Steiner, R. A. S. Salman, R. Beer et al., "European Stroke Organisation (ESO) guidelines for the management of spontaneous intracerebral hemorrhage," *International Journal of Stroke*, vol. 9, no. 7, pp. 840–855, 2014.

[18] A. N. Konovalov, A. Spallone, U. B. Makhmudov, J. A. Kukhlajeva, and V. I. Ozerova, "Surgical management of hematomas of the brain stem," *Journal of Neurosurgery*, vol. 73, no. 2, pp. 181–186, 1990.

[19] H. T. Zhang, L. H. Chen, M. C. Bai, and R. X. Xu, "Anterior subtemporal approach for severe upper pontine hematomas: a report of 28 surgically treated cases," *Journal of Clinical Neuroscience*, vol. 54, pp. 20–24, 2018.

[20] X. Xu, X. Chen, J. Zhang et al., "Comparison of the Tada formula with software Slicer," *Stroke*, vol. 45, no. 11, pp. 3433–3435, 2014.

[21] J. P. Broderick, O. Adeoye, and J. Elm, "Evolution of the modified Rankin scale and its use in future stroke trials," *Stroke*, vol. 48, no. 7, pp. 2007–2012, 2017.

[22] R. Behrouz, "Prognostic factors in pontine haemorrhage: a systematic review," *European Stroke Journal*, vol. 3, no. 2, pp. 101–109, 2018.

[23] X. Q. Zhang, Z. M. Zhang, X. L. Yin, K. Zhang, H. Cai, and F. Ling, "Exploring the optimal operation time for patients with hypertensive intracerebral hemorrhage: tracking the expression and progress of cell apoptosis of prehematomal brain tissues," *Chinese Medical Journal*, vol. 123, no. 10, pp. 1246–1250, 2010.

[24] Q. Wang, W. Guo, Y. Liu et al., "Application of a 3D-printed navigation mold in puncture drainage for brainstem hemorrhage," *The Journal of Surgical Research*, vol. 245, pp. 99–106, 2020.

[25] H. Takahama, K. Morii, M. Sato, K. Sekiguchi, and S. Sato, "Stereotactic aspiration in hypertensive pontine hemorrhage: comparative study with conservative therapy," *No Shinkei Geka. Neurological Surgery*, vol. 17, no. 8, pp. 733–739, 1989.

[26] B. K. Shrestha, L. Ma, Z. G. Lan, H. Li, and C. You, "Surgical management of spontaneous hypertensive brainstem hemorrhage," *Interdisciplinary Neurosurgery*, vol. 2, no. 3, pp. 145–148, 2015.

[27] A. P. Brown, B. G. Thompson, and R. F. Spetzler, "The two-point method: evaluating brain stem lesions," *BNI Q*, vol. 12, pp. 20–24, 1996.

[28] D. D. Cavalcanti, M. C. Preul, M. Y. Kalani, and R. F. Spetzler, "Microsurgical anatomy of safe entry zones to the brainstem," *Journal of Neurosurgery*, vol. 124, no. 5, pp. 1359–1376, 2016.

[29] J. S. Raison, G. Bourbotte, T. P. Baum, and M. Pagès, "Primary brain stem hemorrhage: retrospective study of 25 cases," *Revue Neurologique*, vol. 164, no. 3, pp. 225–232, 2008.

[30] K. B. Huang, Z. Ji, Y. M. Wu, S. N. Wang, Z. Z. Lin, and S. Y. Pan, "The prediction of 30-day mortality in patients with primary pontine hemorrhage: a scoring system comparison," *European Journal of Neurology*, vol. 19, no. 9, pp. 1245–1250, 2012.

[31] K. Balci, T. Asil, M. Kerimoglu, Y. Celik, and U. Utku, "Clinical and neuroradiological predictors of mortality in patients with primary pontine hemorrhage," *Clinical Neurology and Neurosurgery*, vol. 108, no. 1, pp. 36–39, 2005.

Hindawi
Disease Markers
Volume 2022, Article ID 3631532, 11 pages
https://doi.org/10.1155/2022/3631532

Research Article

Echium amoenum L. Ethanol Extract Protects Retinal Ganglion Cell after Glutamate and Optic Nerve Crush Injury

Haibo Li,[1] Ghazaleh Behnammanesh,[2] Zhenkai Wu,[3] Rong Rong,[1] Mengling You,[1] Aman Shah Abdul Majid,[4] and Dan Ji[1]

[1]*Eye Center of Xiangya Hospital and Hunan Key Laboratory of Ophthalmology, Central South University, Changsha, 410008 Hunan Province, China*
[2]*Department of Pharmacology, School of Pharmaceutical Sciences, Universiti Sains Malaysia, Penang, Malaysia*
[3]*The First People's Hospital of Changde, Changde City, 415000 Hunan Province, China*
[4]*Department of Pharmacology, Quest International University Perak, Ipoh, Malaysia*

Correspondence should be addressed to Dan Ji; 475393400@qq.com

Received 10 August 2022; Accepted 27 August 2022; Published 22 September 2022

Academic Editor: Yi Shao

The development of low-cost and effective natural products for treating neuron degenerative diseases have proven to be safe and potentially effective. *Echium amoenum* L. (Boraginaceae) is an annual herb that grows wildly in Europe and western Asia. The aim of this study was to evaluate the neuroprotective properties of an ethanol extract of *E. amoenum* L. The effects of *E. amoenum* L. extract on oxidative stress were measured in the rat R28 retinal precursor cell line. Furthermore, the protective role of the extract on the glutamate-induced and optic nerve crush (ONC) injury-induced cell death were evaluated *in vitro* and *in vivo*, respectively. Our results showed that the ethanol extract of *E. amoenum* L. prevented the glutamate-induced decrease in cell viability and increase in cell death in R28 cells and suppressed the overproduction of ROS induced by glutamate. Moreover, the extract significantly inhibited microglial activation and optic nerve damage induced by ONC injury in mice. In addition, the mechanism was attributed to the ability of the extract to decrease NF-κB pathway activation and its downstream inflammatory cytokine production. In conclusion, *E. amoenum* L. ethanol extract had a potent neuroprotective effect against glutamate-induced and ONC-induced cell death. This is likely due to its antioxidant and anti-inflammatory properties.

1. Introduction

Degenerative diseases of the central nervous system (CNS), injury, and trauma lead to axonal damage, representing major causes of mortality and disability worldwide [1, 2]. Adult CNS neurons in mammals have reduced regenerative potential, leading to permanent impairments and disabilities following injury. Thus, identifying compounds that could be used to protect neurons or help them regenerate after injury is of clinical interest. Currently, the most accepted approach for neuroprotection is oxidative stress reduction using antioxidants, antiapoptotic drugs, anti-inflammatory agents, antiangiogenic agents, and neurotrophic factors [3]. Multiple natural or nutraceutical-based antioxidants have been used as neuroprotective agents to control or slow the development of neurodegenerative ailments, including Alzheimer's disease, amyotrophic lateral sclerosis, ischemic and hemorrhagic stroke, and Parkinson's disease [4–6].

In recent years, the development of low-cost and effective natural products for treating various human ailments has expanded based on large-scale efforts in the screening of crude plant extracts for their biological activities. Commercially, the most important step in developing naturally derived pharmaceuticals is the extraction procedure. The solvent used, yield, and validation assay to assess the pharmacological activities of the extract, availability of raw material, cost, safety of required solvents, and applicability for large-scale production are all important factors to be

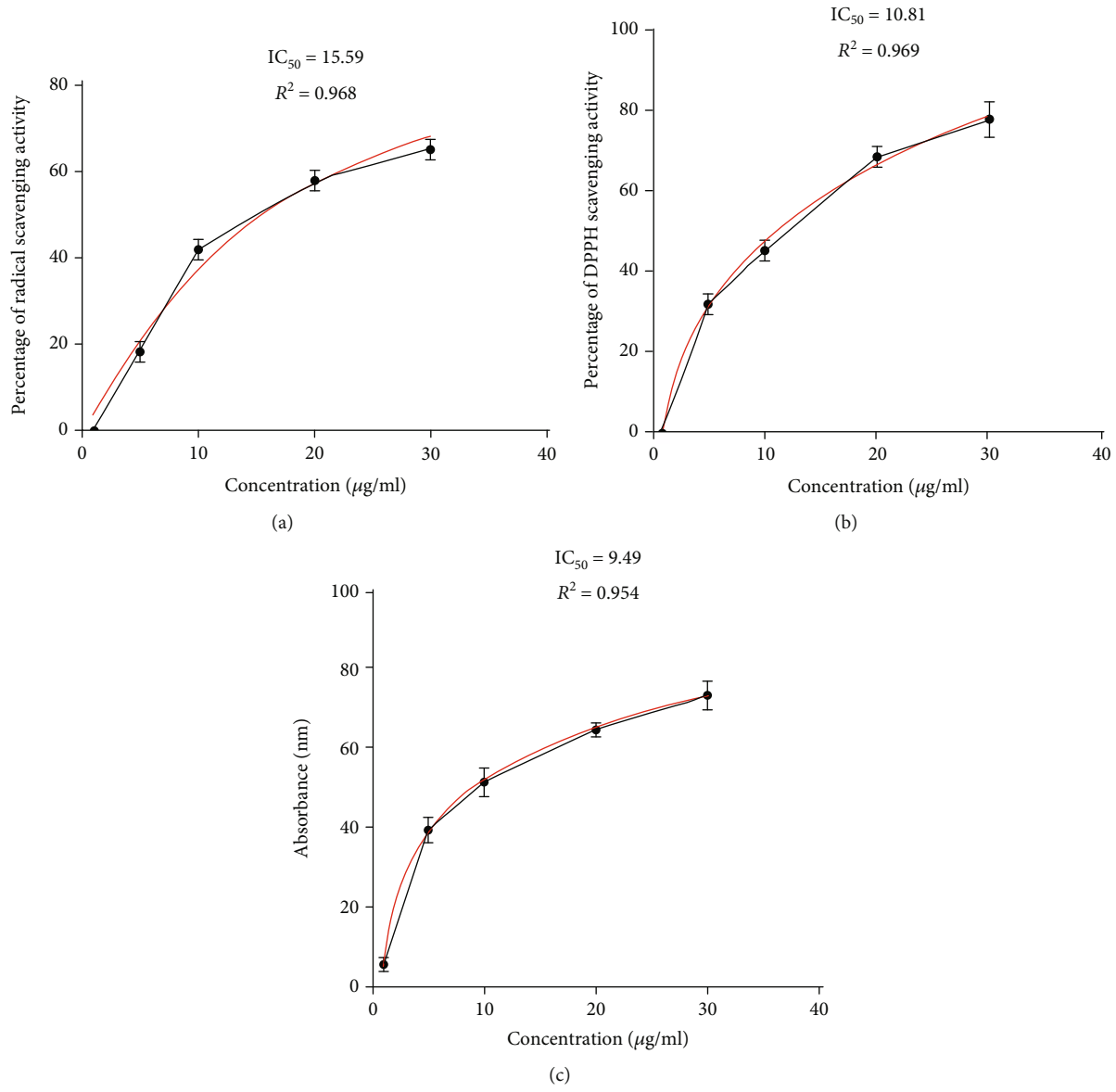

Figure 1: Antioxidant activities of *E. amoenum* ethanol extract. The free radical-scavenging activities of *E. amoenum* ethanol extract were measured using ABTS (a), DPPH (b), and β-carotene bleaching (c) assays. Data are shown as the mean ± SEM from three experiments.

considered. *E. amoenum* L. is an annual herb that grows in most parts of Europe, the Mediterranean region, and northern mountains of Iran. The flowers, stems, roots, and leaves of this plant are used for medicinal purposes. The petals of *E. amoenum* are traditionally brewed or boiled in water, and the flowers and leaves have been used as anti-inflammatory, antioxidant, antibacterial, analgesic, antiviral, anxiolytic, antidepressant, and mood-enhancing agents, and a possible protective effect against cancer has also been proposed [7, 8]. Although *E. amoenum* is extensively used as a medicinal herb in the Middle East, to date, no scientific report has evaluated its potential neuroprotective properties. Therefore, this study assessed the potential neuroprotective features of *E. amoenum* ethanol extract and screened for components that may contribute to such effects.

Optic nerve injury induces the death of 70–75% of retinal ganglion cells (RGCs) within 7 days and 80–90% of cells within 4 weeks, mainly because of apoptosis [9]. RGC death is accompanied by multiple progressive alterations, including glutamate excitotoxicity, ion imbalance, and oxidative stress [10, 11]. The ease of accessibility, coupled with the reproducibility of optic neurodegeneration, makes the optic nerve a highly effective structure for assessing CNS trauma and helps to understand the ensuing traumatic events that activate neuronal apoptosis [12, 13].

Current therapeutic options for neurodegenerative ailments are mainly based on symptomatic relief and not on changing the disease course or progression. Thus, the main aims of this study were to assess whether (a) the potential antioxidant effect of *E. amoenum* ethanol extract could explain its neuroprotective activity and (b) the extract could attenuate the inflammatory reaction associated with optic nerve crush (ONC) injury sustained in the mouse optic nerve. Toward this end, we first analyzed the compounds

Table 1: Chemical composition of the ethanol extract of *E. amoenum* determined using GC-MS.

Peak no.	R. time	Compound	Ref	Quality	Peak height	% area	RI
1	10.29	Palmitic acid, methyl ester	100707	99	703156	1.56	
2	10.62	n-Hexadecanoic acid	92228	96	561497	3.78	419.4
3	11.11	9,12-Octadecadienoic acid, methyl ester	114374	99	1667189	2.41	1394.8
4	11.15	Tricosane	113306	99	1123829	1.77	1479.7
5	11.22	Heptadecanoic acid 16-methyl-, methyl ester (methyl isostearate)	116689	98	562581	0.85	1627.2
6	11.43	9,12-Octadecadienoic acid	106289	99	701410	1.70	2026.6
7	11.95	Campesterol	107653	96	6852862	9.35	2300.1
8	12.36	Tetracosane	136482	95	782762	1.19	2399.9
9	13.76	Linolenic acid, (methyl ester)	130016	97	6070549	11.84	2699.9
10	13.24	Docosane	123096	95	471347	1.05	2600.1
11	15.06	Gamma-sitosterol	158131	99	3341735	9.14	2948.6
12	19.38	Eicosane	156589	91	445259	5.14	3771.1
13	20.88	Nonacosane	159285	99	604971	5.57	4056.9

present in *E. amoenum* ethanol extract and measured their antioxidant activity. We further established mouse and cell models of optic neuropathy to assess the neuroprotective effects of *E. amoenum* ethanol extract *in vitro* and *in vivo*. This study evaluates the potential neuroprotective properties of *E. amoenum* ethanol extracts on the optic nerve at the cellular and molecular levels. These findings could help to promote the clinical treatment of glaucoma optic neuropathy. We also investigated new, effective, and selective natural compounds derived from plants for optic nerve protection to lay an important foundation for the clinical application and large-scale production of natural compounds derived from E. amoenum L.

2. Material and Methods

2.1. Preparation and Extraction of E. Amoenum. Fresh petals of *E. amoenum* were harvested from a farm located 80 km north of Ghazvin, Iran, and authenticated by the Herbarium Unit, School of Biological Sciences, University of Science Malaysia (voucher reference 11525). The extraction was performed as previously described [14]. Briefly, pulverized petals were extracted using the maceration method by adding 800 mL of 98% ethanol to 200 g of plant material at room temperature (RT; 25 ± 2°C) for 48 h with intermittent shaking. The resulting extract was filtered and concentrated under reduced pressure using a rotary evaporator (BUCHI, Germany) at 35°C and lyophilized in a freeze dryer (Labconco, USA). The stock solution was stored at 2–8°C until use.

2.2. Total Phenolic Content Assessment. The total phenolic content of the extract was obtained as described previously [15], with gallic acid as the standard. One milliliter of gallic acid (1–30 μg/mL) in distilled water was added to 0.5 mL of Folin-Ciocalteu reagent (Merck, Darmstadt, Germany), incubated for 4 min at RT, and mixed with 20% Na_2CO_3 (1 mL) and distilled water (6 mL). The mixture was incubated in the dark for 2 h at RT, and the absorbance at 765 nm was measured using a Tecan microplate reader. The *E. amoenum* ethanol extract stock solution (1 mg/mL) was prepared using methanol. To determine the total phenolic content of the extract, Folin-Ciocalteu reagent, Na_2CO_3, test samples, and distilled water were added to a test tube, followed by the same procedures described above for gallic acid. Folin-Ciocalteu reagent is an acidic solution with a yellow color, which changes to blue as a result of molybdenum-tungsten blue complex production through the electron transfer mechanism. The data are presented in units of μg gallic acid equivalents (GAE)/g extract.

2.3. Total Flavonoid Level Assessment. A colorimetric assay was employed to determine the total flavonoid levels in the extract, with quercetin as a reference. Stock solutions of 2 mg/mL *E. amoenum* ethanol extract and 1 mg/mL quercetin were prepared in methanol. For the assay, 1 mL of standard solution (1–30 μg/mL in distilled water) or extract was added to 4 mL of distilled water and 0.3 mL of 5% sodium nitrite. The sample was incubated for 5 min at RT, followed by the addition of 0.3 mL of 10% (w/v) aluminum chloride. Subsequently, 2 mL of 1 M NaOH was added with distilled water to reach a volume of 10 mL. The optical density (OD) was measured at 510 nm using a Tecan microplate reader. For the blank assay, sodium nitrite and aluminum chloride were replaced with water.

2.4. Gas Chromatography-Mass Spectroscopy (GC-MS). GC-MS was used to detect the volatile constituents of the extract [16] on an Agilent GC-MS system (6890 N/5973I) equipped with a single quadruple detector and an HP-5 MS capillary column (0.25 mm × 30 m × 0.25 μm). The injection volume used was 1 μL. The *E. amoenum* components were confirmed using the NIST library identified with standards (retention time and mass spectra).

2.5. Radical Scavenging Activity

2.5.1. 2,2-Azinobis (3-Ethyl-Benzothiazoline-6-Sulfonic Acid) (ABTS) Assay. Radical scavenging activity was first tested using the ABTS assay, with some modifications regarding

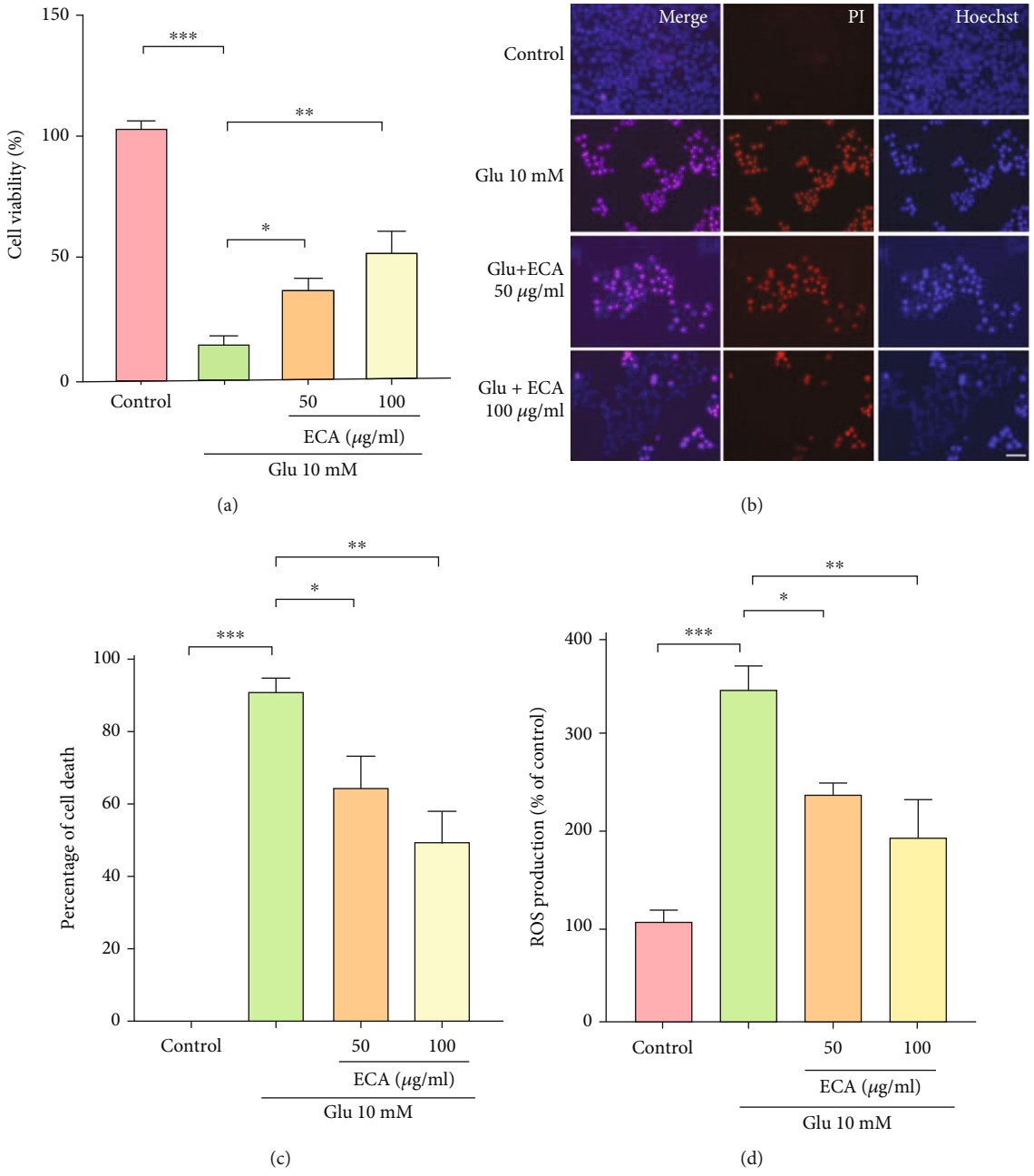

FIGURE 2: Protective effects of the *E. amoenum* ethanol extract on glutamate-induced R28 cell death. (a) Effects of 50 and 100 μg/mL *E. amoenum* ethanol extract on the viability of R28 cells treated with 10 mM glutamate for 24 h, as measured by the CCK-8 assay. (b) Effects of 50 and 100 μg/mL *E. amoenum* ethanol extract on the death of R28 cells treated with 10 mM glutamate for 24 h. (c) Quantification of the percentage of propidium iodide (PI)-positive cells. (d) Fluorescence-activated cell sorting to detect ROS production in glutamate-treated R28 cells. Scale bar = 20 μm. Data are mean ± SEM ($n = 6$); $^{*}P < 0.05$, $^{**}P < 0.01$, and $^{***}P < 0.001$ versus the negative control group. ECA: *E. amoenum* ethanol extract; Glu: glutamate; ROS: reactive oxygen species.

sample volumes and the ABTS solution. This assay assesses the capacity of compounds to scavenge the stable ABTS radical cation ($ABTS^{+}$). Fresh ABTS radicals were obtained by mixing 2.45 mM potassium persulfate and 7 mM ABTS aqueous solutions (2.5 mL each), and the mixture was maintained in the dark for 16–20 h at RT. This solution was adjusted to an OD at 734 nm of 0.70 ± 0.02. A stock solution of the test extract and standard (ascorbic acid) at 1 mg/mL was diluted in methanol to provide a series of working solutions of 1, 5, 10, 20, and 30 μg/mL. Final reaction mixtures consisting of 0.9 mL of ABTS and 0.1 mL of test sample solutions at various concentrations were thoroughly mixed and incubated for 6 min at RT. For blank samples, methanol (0.9 mL) was added to the sample solution at different concentrations (0.1 mL). ABTS solution (0.9 mL) was mixed with methanol (0.1 mL) as a negative control. The OD value was measured at 518 nm using a Tecan microplate reader. The percentage scavenging antioxidant activity was

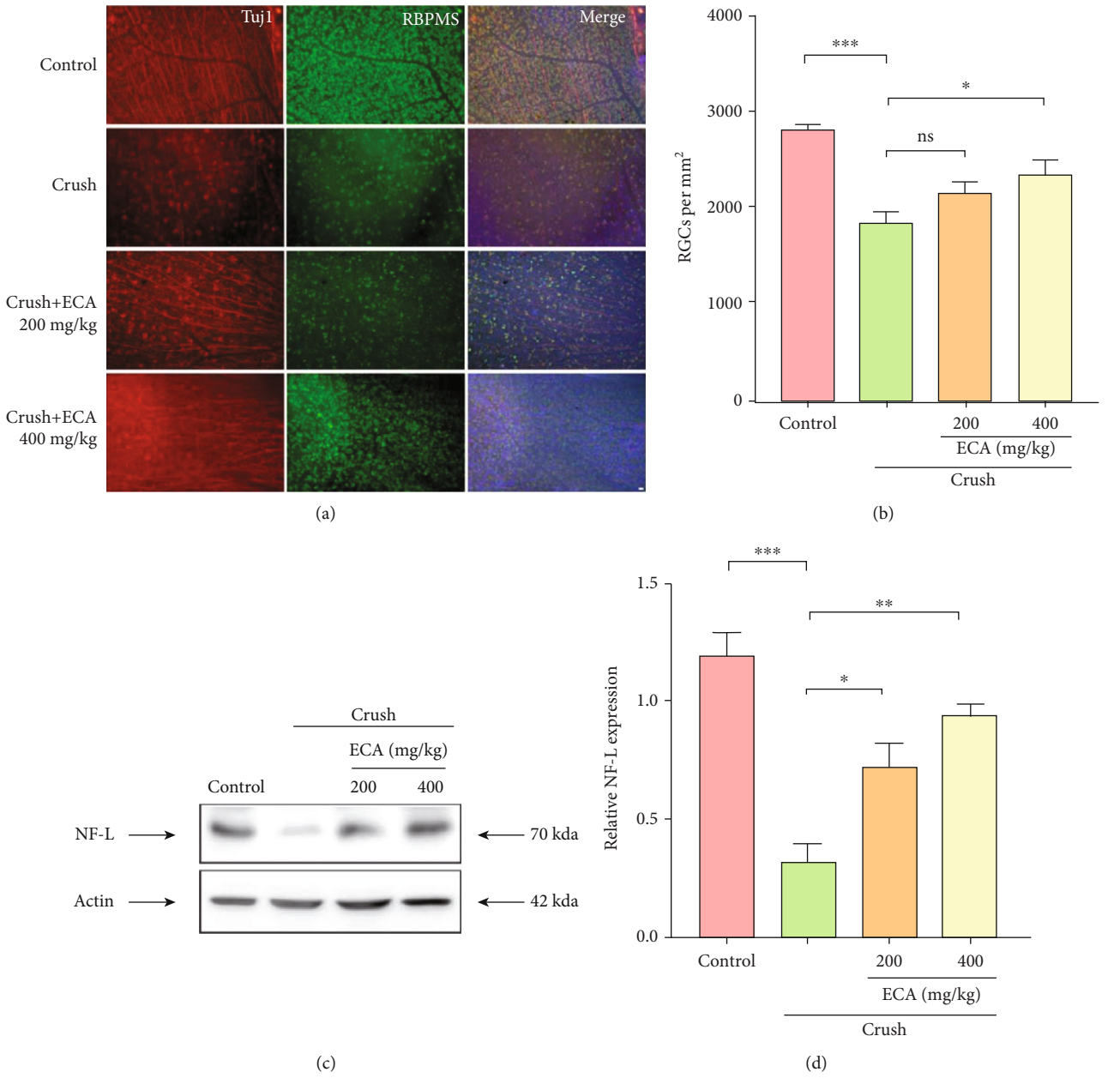

Figure 3: Neuroprotective effects of *E. amoenum* ethanol extract in the optic nerve crush (ONC) mouse model. (a) Retinas from different groups were harvested on day 7 after ONC, and flat-mounted retinas were subjected to immunostaining with RBPMS and Tuj1 antibodies. (b) Quantification of the number of RGCs in 1-mm^2 retina sections. (c) Expression of the optic nerve protein NF-L determined by immunoblotting. (d) Quantification of the NF-L levels. Relative protein levels were calculated using ImageJ software. Results were obtained from three independent experiments. Scale bar = 50 μm. Data are mean ± SEM; $^*P < 0.05$, $^{**}P < 0.01$, and $^{***}P < 0.001$. RGC: retinal ganglion cell; ECA: *E. amoenum* ethanol extract.

calculated as $([A_0 - (A_1 - A_2)]/A_0) \times 100$, where A_0, A_1, and A_2 are the OD values of the control sample, test extract/standard, and corresponding blank, respectively.

2.5.2. 2,2-Diphenyl-1-Picrylhydrazyl (DPPH) Assay. The DPPH assay was performed as previously described [17]. The *E. amoenum* ethanol extract was diluted in methanol to concentrations of 1, 5, 10, 20, and 30 μg/mL. The samples (2.5 mL) in methanol:water (1 : 1) were then mixed with 1 mL of 0.3 mM DPPH in methanol. For the blank samples, methanol (1 mL) was mixed with various extract concentrations. Rutin concentrations of 1, 5, 10, 20, and 30 μg/mL were used as the reference standard. As a negative control, 2.5 mL methanol and 1 mL of 0.3 mM DPPH were mixed. The mixtures were incubated at RT for 30 min to allow stable DPPH radicals to be reduced to diphenylpicrylhydrazine by antioxidants in various solutions. OD values were obtained at 517 nm, and the background value was subtracted. Data are presented as half-maximal inhibitory concentration (IC_{50}) ± standard error of the mean

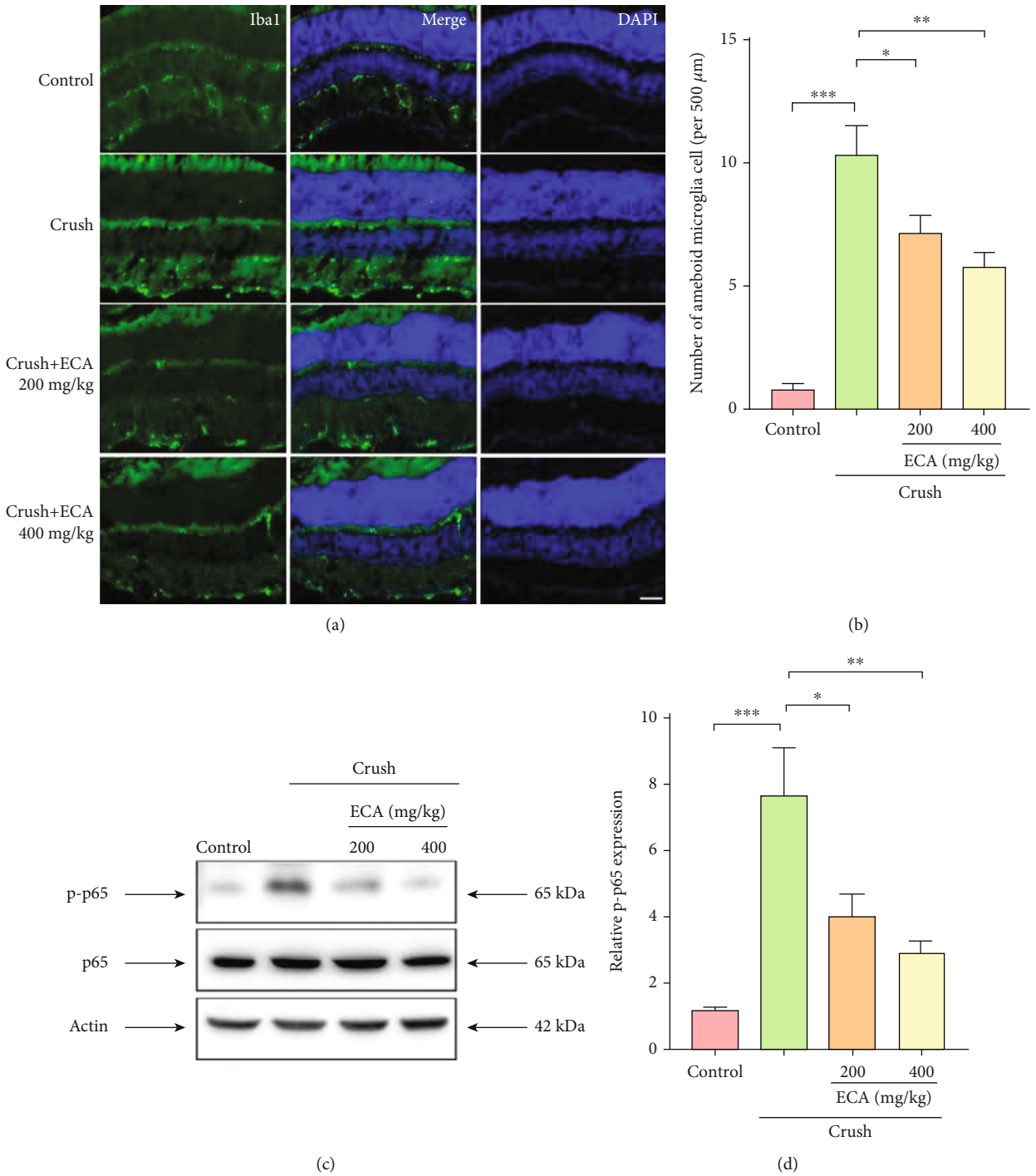

Figure 4: Continued.

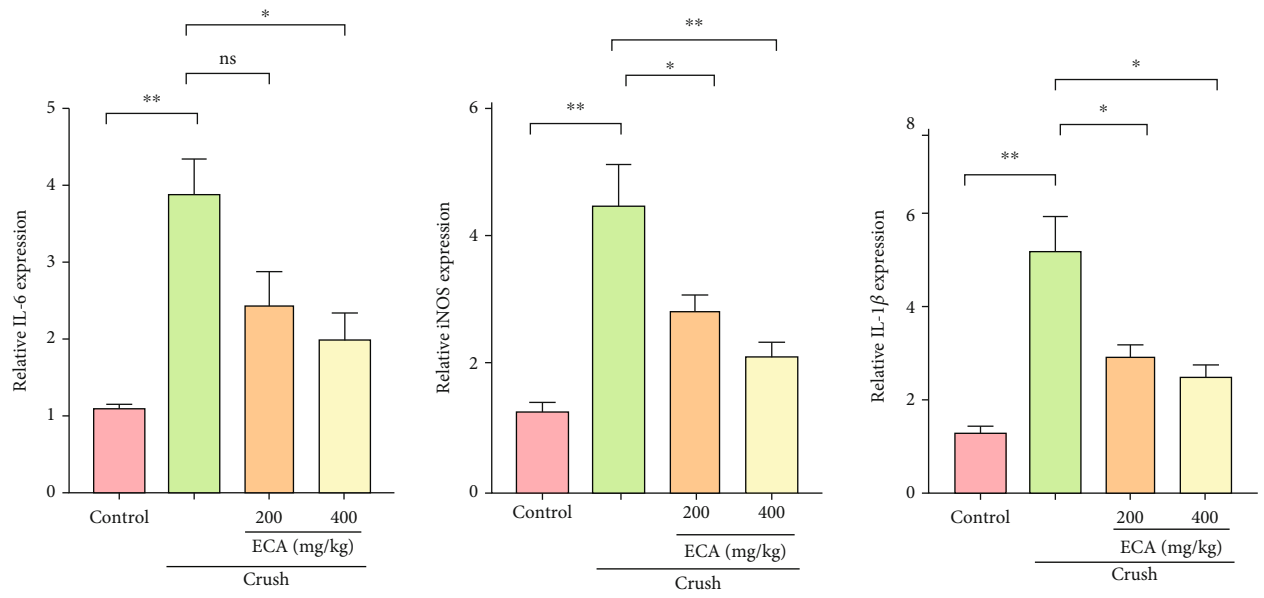

Figure 4: *E. amoenum* ethanol extract suppressed the inflammation response triggered by optic nerve crush (ONC) injury. (a) Retinas from different groups were harvested on day 7 after ONC and subjected to frozen-section immunostaining with Iba1. (b) Quantification of microglia in the retina. (c) Expression of p-p65 in different groups determined by immunoblotting. (d) Quantification of the p-p65 levels in each group. (e) Retinas from different groups were harvested 7 days after ONC and subjected to real-time PCR analysis to determine the relative mRNA levels of IL-6, iNOS, and IL-1β. Data are shown as the mean ± SEM ($n = 3$); $^{*}P < 0.05$, $^{**}P < 0.01$, and $^{***}P < 0.001$.

(SEM), representing the concentration with a scavenging activity of 50%. The percentage of free radical-scavenging activity was calculated as $([A_0 - (A_1 - A_2)]/A_0) \times 100$, where A_0, A_1, and A_2 are the OD values of the control sample, test extract/standard, and corresponding blank, respectively.

2.5.3. β-Carotene Bleaching Assay. The β-carotene bleaching assay was performed as previously described [18]. First, 1 mL of β-carotene in chloroform (0.2 mg/mL) was added to linoleic acid (20 mg) and 200 mg Tween 40. After the chloroform was removed using a rotary evaporator, distilled water (50 mL) was used for emulsification. Emulsion aliquots were mixed with 0.2 mL of the *E. amoenum* ethanol extract at 1, 5, 10, 20, and 30 μg/mL. Butylated hydroxytoluene (BHT; 0.5, 1, 5, 10, and 20 μg/mL) was used as the reference standard. The initial OD was obtained at 470 nm on a Tecan microplate reader immediately after emulsion addition. The samples were incubated at 50°C in a water bath, and OD values were obtained every 20 min until a color change in the control samples was observed. Antioxidant activity was calculated as $(\text{final } \beta - \text{carotene amount/initial } \beta - \text{carotene amount}) \times 100$. The IC_{50} value of the extract was obtained from the curve of antioxidant activity percentage versus the extract level.

2.6. Cell Viability and Cell Death Assays in R28 Cells. Rat retinal precursor R28 cells were used as an *in vitro* model owing to their similar characteristics to retinal neurons (Kerafast, Boston, MA, USA). Cell viability was measured using the Cell Counting Kit-8 (CCK-8; NCM Biotech, China). Hoechst 33342-propidium iodide dual staining (Beyotime, Shanghai, China) was used to detect cell death, according to the manufacturer's instructions.

2.7. Reactive Oxygen Species (ROS) Production. R28 cells were treated with the ethanol extract of *E. amoenum* (50 or 100 μg/mL) and 10 mM glutamate for 12 h, digested with collagenase IV (Gibco, Waltham, MA, USA), and then suspended in medium containing 10 μM of the fluorescent probe 2′-7′-dichlorofluorescin diacetate (Sigma-Aldrich, St. Louis, MO, USA). After 30 min of incubation at 37°C in the dark, the cells were centrifuged at 1000 g, resuspended in fresh medium, and subjected to fluorescence activated cell sorting analysis. The mean fluorescent intensity was compared between the treated groups and control group using FlowJo 7.6 software (Tree Star Inc., Ashland, USA). The experiments were repeated three times.

2.8. Animals. BALB/c mice were used in this study. All animal experiments were conducted in accordance with the Animal Ethics Guidelines of Xiangya Hospital, Central South University (permit number: 202108022). During the experimental period, all mice were maintained in standard cages in an animal room under normal environmental conditions. All surgery was performed under anesthesia, and all efforts were made to minimize suffering. Twelve male mice (8–12 weeks old) were randomly divided into four groups: the normal control and negative control groups and two groups of test animals ($n = 3$ per group). The two control groups were fed a normal diet. For the two test groups, the mice were orally administered 200 mg/kg and 400 mg/kg of ethanol extract once daily for 10 days. Subsequently, ONC

was performed as described below. In this study, no participants have involved in this basic research, so there is no need to provide informed consent.

2.9. ONC Model. Mice were anesthetized by intraperitoneal injection of ketamine (90 mg/kg) and xylazine (10 mg/kg). Unilateral ONC injury was induced in the negative control and test groups, as described previously [19]. The optic nerve of the left eye was pressed 0.5 mm posterior from the globe for 10s using Jeweler's forceps without damaging the ocular blood vessels. The contralateral eye was used as the uncrushed control.

2.10. Immunocytochemistry and Immunostaining of Flat-Mounted Retinas. For the retina immunohistochemistry analysis, the eyes were dissected and fixed in 4% paraformaldehyde at RT for 2 h and dehydrated in 20% sucrose before embedding in O.C.T. mounting medium. Frozen sections (16 μm) were then cut using a cryostat microtome (CM1860; Leica, Nussloch, Germany). Immunohistochemistry was performed using anti-Iba1 rabbit antibody (Abcam, ab178847, 1/300). The nuclei were stained with 4′,6-diamidino-2-phenylindole (DAPI) for 2 min. Slides were examined using a fluorescence microscope (Leica, Wetzlar, Germany). Iba1-positive cells were quantitatively analyzed using ImageJ software.

For immunostaining of flat-mounted retinas, the eyes of mice in the ONC group with or without *E. amoenum* ethanol extract treatment were enucleated and fixed in 4% paraformaldehyde for 1 h at RT. The retinas were peeled off, prepared as flattened whole mounts, and permeabilized in 0.5% Triton X-100 in phosphate-buffered saline (PBS) for 15 min at RT. The flat-mounted retinas were then washed with PBS and incubated overnight at 4°C with anti-RBPMS rabbit polyclonal antibody (Thermo Fisher Scientific, PA5-31231, 1/300) and anti-Tuj1 mouse monoclonal antibody (Millipore, MAB1637, 1/300). The nuclei were stained with DAPI for 2 min, and flat-mounted retinas were examined using a fluorescence microscope (Leica). Each image was obtained from eight 20× fields around the peripheral retina (two in each quadrant) for each whole-mounted retina. The number of RBPMS-positive cells, as a marker of RGCs, in each image was quantified using ImageJ software as described previously [20].

2.11. Immunoblotting. Immunoblotting was performed as described previously [21], with the following primary antibodies: mouse anti-Neurofilament light chain (NF-L) (Cell Signaling Technology, 2837S, 1/1000), antiphospho-NF-κB p65 (Ser536) rabbit antibody (Cell Signaling Technology, 3033S, 1/1000), anti-NF-κB p65 rabbit antibody (Cell Signaling Technology, 8242S, 1/1000), and mouse anti-actin (Cell Signaling Technology, 3700S, 1/5000). Mouse retinas of each group were isolated and sonicated in 150 μL of homogenization buffer (20 mM Tris/HCl, pH 7.4, containing 2 mM EDTA, 0.5 mM EGTA, 1% sodium dodecyl sulfate, 0.1 mM phenylmethylsulfonyl fluoride, 50 μg/mL aprotinin, 50 μg/mL leupeptin, and 50 μg/mL pepstatin A). An equal volume of sample buffer (62.5 mM Tris/HCl, pH 7.4, containing 4% sodium dodecyl sulfate, 10% glycerol, 10% mercaptoethanol, and 0.002% bromophenol blue) was immediately added, and samples were boiled for 2–3 min. The protein content was determined using a bicinchoninic acid protein kit (Sigma-Aldrich). Equal amounts of protein were separated by electrophoresis on 10% polyacrylamide gels containing 0.1% sodium dodecyl sulfate. Proteins were transferred to nitrocellulose membranes and the blots were incubated for 2 h at room temperature with primary antibodies. Detection was performed using the appropriate horseradish-conjugated secondary antibodies for 1 h at RT. Bands were visualized using an enhanced chemiluminescence solution and quantified using ImageJ software (Wayne Rasband, National Institutes of Health, Bethesda, MD, USA).

2.12. Quantitative Real-Time Polymerase Chain Reaction (PCR). Total RNA of mouse retinas was obtained using RNeasy® Kit (Qiagen), according to the manufacturer's instructions, and quantified on a NanoDrop 1000 spectrophotometer (Thermo Scientific, Waltham, MA, USA). Reverse transcription was performed using Oligo dT and Superscript III reverse transcriptase (Invitrogen, 11732020). Primers were manufactured by Sangon Biotech (Shanghai, China), and the following primer sequences were used: *Il6* (forward 5′-GTGGCTAAGGACCAAGACCA-3′ and reverse 5′-ACCA CAGTGAGGAATGTCCA-3′), *Il1b* (forward5′-GCAACG GGAAGATTCTGAAG-3′ and reverse 5′-TGACAAACTTC TGCCTGACG-3′), iNOS (forward 5′-ACGAGACGGAT AGGCAGAGA-3′ and reverse 5′-CACATGCAAGGAAGGG AACT-3′), and beta-actin (forward 5′-CACGATGGAGG GGCCGGACTCATC′ and reverse 5′-TAAAGACCTCTATG CCAACACAGT-3′).

Real-time PCR was performed with SYBR Green I Master mix (Applied Biosystems) in triplicate reactions (20 μL) containing 1 μL of cDNA template with 500 nM primers, at 95°C (10 min), followed by 40 cycles of 95°C (15 s) and 60°C (1 min), and finally 78°C for 20 s. Melting curve generation was performed using Dissociation Curves software (Applied Biosystems). The $2^{-\Delta\Delta CT}$ method was used for the data analysis.

2.13. Statistical Analysis. Statistical analyses were performed using GraphPad Prism software (version 8.0). One-way analysis of variance with Tukey's multiple comparison test was used for normally distributed variables or the Kruskal-Wallis test was used for variables with a skewed distribution. Data are presented as the mean percentage of control ± SEM . Statistical significance was set at $P < 0.05$.

3. Results

3.1. Antioxidant Activities of the E. amoenum Ethanol Extract. The total phenolic content of the dry *E. amoenum* ethanol extract was 1390 ± 22 μg GAE/g. The total flavonoid content of the dry extract was 9360 ± 83 μg QE/g. Figure 1(a) shows the free radical-scavenging activity of the *E. amoenum* ethanol extract in the ABTS assay, with an IC_{50} value of 15.59 μg/mL. Ascorbic acid, the reference antioxidant, displayed an IC_{50} of 4.97 ± 0.06 μg/mL. Figure 1(b) shows that the extract had a strong antioxidant effect, as indicated by the low IC_{50} of

10.81 μg/mL; the reference rutin had an IC_{50} of 3.23 ± 0.02 μg/mL. These findings indicated that the extract potently scavenged the stable free radical DPPH. The β-carotene bleaching effects of the extract are shown in Figure 1(c). The IC_{50} of the standard (BHT) was 0.89 ± 0.04 μg/mL. The low IC_{50} of 9.49 μg/mL of the extract indicated its high β-carotene bleaching activity. GC-MS analysis revealed the presence of 13 phytochemical constituents in the extract (Table 1), with linolenic acid, campesterol, and γ-sitosterol as the major components.

3.2. Protective Effects of the E. amoenum Ethanol Extract on Glutamate-Induced R28 Cell Death. R28 cells treated with 10 mM glutamate for 24 h showed significantly reduced viability (15.3% compared with the control). Moreover, treatment with 50 and 100 μg/mL *E. amoenum* ethanol extract increased cell viability by approximately 21.6% and 36.6%, respectively (Figure 2(a)). Further support for the neuroprotective effect of *E. amoenum* ethanol extract was obtained by propidium iodide dual staining (Figures 2(b) and 2(c)). Administration of 10 mM glutamate resulted in massive cell death. More specifically, the percentage of PI-positive cells in the glutamate-treated group for 24 h was 90.4% ± 3.6. Treatment with 50 and 100 μg/mL *E. amoenum* ethanol extracts reversed these glutamate-induced effects, with higher efficacy found for the higher dose (the percentage of PI-positive cells decreased to 63.9% ± 8.4 and 48.9% ± 8.7, respectively). As shown in Figure 2(d), R28 cells treated with glutamate showed a massive increase in ROS production, which was significantly decreased with treatment of *E. amoenum* ethanol extract (50 and 100 μg/mL). Collectively, these results demonstrated that *E. amoenum* ethanol extract protects against glutamate-induced oxidative stress and cell death.

3.3. Neuroprotective Effects of E. amoenum Ethanol Extract in ONC Mouse Model. After image acquisition and data recording of flat-mounted retinas, the number of RBPMS-positive cells (representing RGCs) was calculated in a 1-mm^2 section. ONC induced a significant decrease in RGCs, whereas the number of RGCs in animals administered 200 mg/kg and 400 mg/kg of *E. amoenum* ethanol extract was markedly increased compared with that in the ONC group, suggesting attenuation of RGC injury in response to ONC (Figures 3(a) and 3(b)). Neurofilament light chain (NF-L) is a neuronal intermediate filament in optic nerve axons that has been used as an indicator of optic nerve injury. ONC also reduced the NF-L protein levels, whereas administration of *E. amoenum* ethanol extract (200 or 400 mg/kg) significantly alleviated this effect (Figure 3(c)). Specifically, the decrease rates for NF-L protein after ONC in the negative control, 200 mg/kg *E. amoenum* ethanol extract, and 400 mg/kg *E. amoenum* ethanol extract groups were 87.6%, 47.2%, and 28.6%, respectively (Figure 3(d)). Taken together, these findings demonstrate that *E. amoenum* ethanol extract has a neuroprotective effect in an *in vivo* ONC model.

3.4. E. amoenum Ethanol Extract Suppressed the ONC-Induced Inflammation Response. To determine the anti-inflammatory effects of *E. amoenum* ethanol extract in the ONC mouse model, Iba1-positive cells were detected in the frozen sections of each group as a marker of ameboid microglia cells. The *E. amoenum* ethanol extract group showed a reduced number of activated microglia cells (Figures 4(a) and 4(b)). To explore the mechanism underlying the anti-inflammatory effect of *E. amoenum* ethanol extract, phospho-NF-κB p65 levels in ONC mice treated with or without *E. amoenum* ethanol extract were compared by immunoblotting. Interestingly, phospho-p65 levels in the 200 and 400 mg/kg groups were significantly decreased compared with the control values (Figures 4(c) and 4(d)). As the downstream targets of NF-κB activation, the elevated mRNA levels of proinflammatory cytokines such as IL-6, iNOS, and IL-1β triggered by glutamate were significantly decreased upon *E. amoenum* ethanol extract treatment (Figure 4(e)). Taken together, these results suggest that inhibition of the NF-κB pathway by *E. amoenum* ethanol extract blocks ONC-induced microglial activation and proinflammatory cytokine release.

4. Discussion

The complex process of neurodegeneration can be initiated as a result of serious acute traumatic injury or chronic intermittent and progressive damage by ischemic and hypoxic conditions associated with oxidative stress, e.g., in Alzheimer's, Parkinson's, and Huntington's diseases, as well as in optic neuropathies. Neuroprotection refers to any therapeutic strategy for the prevention, delay, or reversal of neuron damage or death associated with a given pathology [1, 2, 4, 22].

E. amoenum extract has shown anti-inflammatory, antioxidative effects and neuroprotective activity in traditional medicine. Recently, a study reported that *E. amoenum* extract could modulate the inflammatory modes of the macrophages through the inhibition of iNOS and COX2 enzymes as well as through cytokines expression [23], It has also been suggested the pharmacological effects of *E. amoenum* extract in treating patients with depression, generalized anxiety disorder, or Alzheimer's disease [24, 25]. However, its role in alleviating or protecting against CNS injury and the underlying mechanisms remain unclear. Here, we demonstrated that the simple crude ethanol extract of *E. amoenum* showed antioxidant capacity in the ABTS and DPPH tests, as well as in the β-carotene bleaching assay. These results confirmed that the extract is a potent antioxidant, as supported by previous studies [7, 26]. The extract also showed free radical-scavenging and neuroinflammatory mediator effects in an ONC mouse model. Thus, the current study is the first to assess the neuroprotective features of *E. amoenum* and to highlight the potential application of this herb as a model of neuronal injury in a mouse model of retinal neurodegeneration.

Further phytochemical screening of the extract revealed various constituents such as linolenic acid, γ-sitosterol, and campesterol, which together may exert synergistic effects leading to the observed neuroprotective activity. These three compounds were also found in a *Rhus coriaria* extract, which showed beneficial effects in a mouse model of ischemic optic neuropathy [27], supporting the results of the present study. Another study showed the beneficial effects of these compounds

in *Drosophila* models of neurodegenerative diseases [28]. In addition, since linolenic acid, γ-sitosterol, and campesterol were found at high levels in the extract, they could be used as markers for the standardization of *E. amoenum* ethanol extract and its development as a functional neuroprotective agent.

Microglia undergo different phenotypic changes in different disease states, and several studies have found that the activation of microglia has both protective and damaging effects. When the inflammatory state persists for a long time, the reaction products of microglia may cause damage to the surrounding tissues and even affect healthy cells, especially neurons. Many studies have shown that microglia-mediated inflammation is involved in RGC death, and thus inhibiting the immune response of microglia has a protective effect on RGCs [29, 30]. A similar phenomenon was observed in the present study as *E. amoenum* ethanol extract inhibited microglial activation and cytokine production. NF-κB is involved in many signaling pathways, including inflammation, development, cell growth, and apoptosis [31]. Glutamate-associated apoptosis and NF-κB expression are correlated in vascular endothelial cells, cardiomyocytes, and RGCs [31, 32]. Therefore, NF-κB is considered a potential drug target for novel treatments that reduce inflammation and apoptosis [33]. Consistent with these previous studies, the present study showed that ONC upregulated the expression of molecules associated with the NF-κB pathway, whereas *E. amoenum* ethanol extract significantly downregulated NF-κB expression and its downstream cytokine production. Of course, there is a strong possibility that other pathways might be involved in the observed effects, and thus additional studies are needed to determine the exact mechanisms of *E. amoenum* ethanol extract.

In summary, *E. amoenum* ethanol extract demonstrated potent neuroprotective effects in an *in vivo* model of retinal neurodegeneration, likely because of its antioxidant and anti-inflammatory properties. Accordingly, the present findings support the premise that *E. amoenum* is a bioactive herb that should be further evaluated as an adjunctive neuroprotective agent for preventing neurodegenerative ailments such as glaucoma and neurodegenerative diseases.

Abbreviations

CNS:	Central nervous system
CCK-8:	Cell Counting Kit-8
DAPI:	4′,6-diamidino-2-phenylindole
E. Amoenum:	*Echium amoenum* L
ECA:	*E. amoenum* ethanol extract
Glu:	Glutamate
ONC:	Optic nerve crush
ROS:	Reactive oxygen species.

Data Availability

The data used to support the findings of this study are available from the corresponding author upon request.

Conflicts of Interest

The authors declared no potential conflicts of interest with respect to the research, authorship, and/or publication of this article.

Authors' Contributions

Haibo Li, Ghazaleh Behnammanesh, and Zhenkai Wu contributed equally to this work.

Acknowledgments

The authors disclosed receipt of the following financial support for the research, authorship, and/or publication of this article. This work was supported by grants from the National Key Research and Development Program of China (2021YFA1101200 and 2021YFA1101202) and the Natural Science Foundation of Hunan Province (2021JJ31068).

References

[1] N. Egawa, J. Lok, K. Washida, and K. Arai, "Mechanisms of axonal damage and repair after central nervous system injury," *Translational Stroke Research*, vol. 8, no. 1, pp. 14–21, 2017.

[2] M. Curcio and F. Bradke, "Axon regeneration in the central nervous system: facing the challenges from the inside," *Annual Review of Cell and Developmental Biology*, vol. 34, no. 1, pp. 495–521, 2018.

[3] D. Nuzzo, "Role of natural antioxidants on neuroprotection and neuroinflammation," *Antioxidants (Basel)*, vol. 10, 4, p. 608, 2021.

[4] X. Antoniou, T. Borsello, T. F. Lüscher, and G. G. Camici, "Antioxidants and neuroprotection," in *Systems Biology of Free Radicals and Antioxidants*, pp. 2175–2189, Springer, Verlag Berlin Heidelberg, 2014.

[5] B. A. Q. Gomes, J. P. B. Silva, C. F. R. Romeiro et al., "Neuroprotective mechanisms of resveratrol in Alzheimer's disease: role of SIRT1," *Oxidative Medicine and Cellular Longevity*, vol. 2018, Article ID 8152373, 15 pages, 2018.

[6] S. Paul and E. Candelario-Jalil, "Emerging neuroprotective strategies for the treatment of ischemic stroke: an overview of clinical and preclinical studies," *Experimental Neurology*, vol. 335, article 113518, 2021.

[7] H. Azizi, S. Ghafari, R. Ghods, A. Shojaii, M. Salmanian, and J. Ghafarzadeh, "A review study on pharmacological activities, chemical constituents, and traditional uses of Echium amoenum," *Pharmacognosy Reviews*, vol. 12, no. 24, pp. 208–213, 2018.

[8] F. Nadi, "Bioactive compound retention in Echium amoenum Fisch. & C. A. Mey. petals: effect of fluidized bed drying conditions," *International Journal of Food Properties*, vol. 20, no. 10, pp. 2249–2260, 2017.

[9] V. Vigneswara, N. Akpan, M. Berry, A. Logan, C. M. Troy, and Z. Ahmed, "Combined suppression of CASP2 and CASP6 protects retinal ganglion cells from apoptosis and promotes axon regeneration through CNTF-mediated JAK/STAT signalling," *Brain*, vol. 137, pp. 1656–1675, 2014.

[10] E. Y. C. Kang, P. K. Liu, Y. T. Wen et al., "Role of oxidative stress in ocular diseases associated with retinal ganglion cells degeneration," *Antioxidants (Basel)*, vol. 10, no. 12, p. 1948, 2021.

[11] I. Christensen, B. Lu, N. Yang, K. Huang, P. Wang, and N. Tian, "The susceptibility of retinal ganglion cells to glutamatergic excitotoxicity is type-specific," *Frontiers in Neuroscience*, vol. 13, p. 219, 2019.

[12] A. S. Ibrahim, K. Elmasry, M. Wan et al., "A controlled impact of optic nerve as a new model of traumatic optic neuropathy in mouse," *Investigative Ophthalmology & Visual Science*, vol. 59, no. 13, pp. 5548–5557, 2018.

[13] E. G. Burke, S. M. Cansler, and N. K. Evanson, "Indirect traumatic optic neuropathy: modeling optic nerve injury in the context of closed head trauma," *Neural Regeneration Research*, vol. 14, no. 4, pp. 593-594, 2019.

[14] M. Rabbani, S. E. Sajjadi, and S. Khalili, "A Lack of tolerance to the anxiolytic action of Echium amoenum," *Research in Pharmaceutical Sciences*, vol. 6, pp. 101–106, 2011.

[15] D. W. Al-Dualimi, A. Shah Abdul Majid, S. F. F. Al-Shimary et al., "50% Ethanol extract of Orthosiphon stamineus modulates genotoxicity and clastogenicity induced by mitomycin C," *Drug and Chemical Toxicology*, vol. 41, pp. 82–88, 2018.

[16] O. D. Sparkman, Z. Penton, and F. G. Kitson, *Gas Chromatography and Mass Spectrometry: A Practical Guide: A Practical Guide*, Academic Press, 2011.

[17] J. Xie and K. M. Schaich, "Re-evaluation of the 2,2-diphenyl-1-picrylhydrazyl free radical (DPPH) assay for antioxidant activity," *Journal of Agricultural and Food Chemistry*, vol. 62, pp. 4251–4260, 2014.

[18] M. A. Prieto, I. Rodríguez-Amado, J. A. Vázquez, and M. A. Murado, "β-Carotene assay revisited. Application to characterize and quantify antioxidant and prooxidant activities in a microplate," *Journal of Agricultural and Food Chemistry*, vol. 60, no. 36, pp. 8983–8993, 2012.

[19] Z. Tang, S. Zhang, C. Lee et al., "An optic nerve crush injury murine model to study retinal ganglion cell survival," *Journal of Visualized Experiments*, vol. 50, 2011.

[20] X. Guo, J. Zhou, C. Starr et al., "Preservation of vision after CaMKII-mediated protection of retinal ganglion cells," *Cell*, vol. 184, pp. 4299–4314.e12, 2021.

[21] Y. Li, H. Li, L. Zhang et al., "Growth/differentiation 5 promotes the differentiation of retinal stem cells into neurons via Atoh8," *Journal of Cellular Physiology*, vol. 234, pp. 21307–21315, 2019.

[22] K. D. Kang, A. S. Abdul Majid, K. A. Kim et al., "Sulbutiamine counteracts trophic factor deprivation induced apoptotic cell death in transformed retinal ganglion cells," *Neurochemical Research*, vol. 35, pp. 1828–1839, 2010.

[23] N. Naseri, K. Kalantar, and Z. Amirghofran, "Anti-inflammatory activity of Echium amoenum extract on macrophages mediated by inhibition of inflammatory mediators and cytokines expression," *Research in Pharmaceutical Sciences*, vol. 13, pp. 73–81, 2018.

[24] M. Anushiravani, A. A. Manteghi, A. Taghipur, and M. Eslami, "Comparing effectiveness of a combined herbal drug based on Echium amoenum with citalopram in the treatment of major depressive disorder," *Current Drug Discovery Technologies*, vol. 16, pp. 232–238, 2019.

[25] L. Sadeghi, V. Yousefi Babadi, and F. Tanwir, "Improving effects of Echium amoenum aqueous extract on rat model of Alzheimer's disease," *Journal of Integrative Neuroscience*, vol. 17, pp. 661–669, 2018.

[26] L. Safaeian, S. Haghjoo Javanmard, M. Ghanadian, and S. Seifabadi, "Cytoprotective and antioxidant effects of Echium amoenum anthocyanin-rich extract in human endothelial cells (HUVECs)," *Avicenna Journal of Phytomedicine*, vol. 5, no. 2, pp. 157–166, 2015.

[27] S. Khalilpour, G. Behnammanesh, F. Suede et al., "Neuroprotective and anti-inflammatory effects of Rhus coriaria extract in a mouse model of ischemic optic neuropathy," *Biomedicine*, vol. 6, no. 2, 2018.

[28] M. J. Lee, S. H. Park, J. H. Han et al., "The effects of hempseed meal intake and linoleic acid on drosophila models of neurodegenerative diseases and hypercholesterolemia," *Molecules and Cells*, vol. 31, no. 4, pp. 337–342, 2011.

[29] P. Yang, L. Chen, Y. Shi et al., "Progesterone alters the activation and typing of the microglia in the optic nerve crush model," *Experimental Eye Research*, vol. 212, article 108805, 2021.

[30] N. Wu, J. Yu, S. Chen et al., "Alpha-Crystallin protects RGC survival and inhibits microglial activation after optic nerve crush," *Life Sciences*, vol. 94, pp. 17–23, 2014.

[31] W. C. Jia, G. Liu, C. D. Zhang, and S. P. Zhang, "Formononetin attenuates hydrogen peroxide (H2O2)-induced apoptosis and NF-kappaB activation in RGC-5 cells," *European Review for Medical and Pharmacological Sciences*, vol. 18, pp. 2191–2197, 2014.

[32] Y. Li, J. Xia, N. Jiang et al., "Corin protects H_2O_2-induced apoptosis through PI3K/AKT and NF-κB pathway in cardiomyocytes," *Biomedicine & Pharmacotherapy = Biomedecine & Pharmacotherapie*, vol. 97, pp. 594–599, 2018.

[33] A. Panday, M. E. Inda, P. Bagam, M. K. Sahoo, D. Osorio, and S. Batra, "Transcription factor NF-kappaB: an update on intervention strategies," *Archivum Immunologiae et Therapiae Experimentalis*, vol. 64, pp. 463–483, 2016.

Hindawi
Disease Markers
Volume 2022, Article ID 4046809, 6 pages
https://doi.org/10.1155/2022/4046809

Review Article

Progress of Bulbar Conjunctival Microcirculation Alterations in the Diagnosis of Ocular Diseases

Zhengze Sun,[1] **Yaxin Li**,[1,2] **Rongjun Liu**,[1] **Baikai Ma**,[1] **Yifan Zhou**,[1] **Hongyu Duan**,[1] **Linbo Bian**,[1] **Wenlong Li**,[1] **and Hong Qi**[1]

[1]*Department of Ophthalmology, Peking University Third Hospital, Beijing Key Laboratory of Restoration of Damaged Ocular Nerve, Beijing 100191, China*
[2]*The First Hospital of Fangshan District, Beijing 102400, China*

Correspondence should be addressed to Hong Qi; doctorqihong@hotmail.com

Received 10 July 2022; Accepted 20 August 2022; Published 28 August 2022

Academic Editor: Yang Qi-Chen

Bulbar conjunctival microcirculation is a microvascular system distributed in the translucent bulbar conjunctiva near the corneal limbus. Multiple ocular diseases lead to bulbar conjunctival microcirculation alterations, which means that bulbar conjunctival microcirculation alterations would be potential screening and diagnostic indicators for these ocular diseases. In recent years, with the emergence and application of a variety of noninvasive observation devices for bulbar conjunctiva microcirculation and new image processing technologies, studies that explored the potential of bulbar conjunctival microcirculation alterations in the diagnosis of ocular diseases have been emerging. However, the potential of bulbar conjunctival microcirculation alterations as indicators for ocular diseases has not been exploited to full advantage. The observation devices, image processing methods, and algorithms are not unified. And large-scale research is needed to concrete bulbar conjunctival microcirculation alterations as indicators for ocular diseases. In this paper, we provide an update on the progress of bulbar conjunctival microcirculation alterations in the diagnosis of ocular diseases in recent five years (from January 2017 to March 2022). Relevant ocular diseases include contact lens wearing, dry eye, conjunctival malignant melanoma, conjunctival nevus, and diabetic retinopathy.

1. Introduction

The bulbar conjunctiva is a microvascular-rich translucent membrane that covers the sclera. Microcirculation refers to the microvessels between arterioles and venules, which is the basic functional unit of blood circulation. The bulbar conjunctival microcirculation is an uneven reticulated system adjacent to the corneal limbus, supplied primarily by the anterior ciliary artery and the palpebral artery arch. The anterior ciliary artery separates a small upper branch of the sclera 3 to 5 mm outside the corneal limbus to form a blood vessel network and is distributed in the bulbar conjunctiva. The palpebral artery arch crosses the tarsal plate and is distributed in the palpebral conjunctiva, conjunctival fornix, and bulbar conjunctiva 4 mm or more from the corneal limbus. The bulbar conjunctival microcirculation is rich in branches and anastomosis, the ratio of arterioles to venules is about 1 : 2, the diameter of microvessels is between 5 and 70 μm, and the blood flow velocity is between 0.52 and 3.26 mm/s [1, 2]. A variety of ocular diseases affect the bulbar conjunctival microcirculation, and due to the translucent nature of the bulbar conjunctiva, noninvasive observations of the bulbar conjunctival microcirculation can be made.

The observation of the bulbar conjunctival microcirculation initially adopted the invasive method represented by fluorescein angiography and indocyanine green contrast and could only be made qualitatively or semiquantitatively. In 2004, minimally invasive confocal fluorescence microscopy

was applied to microcirculation in vivo observations at the bulbar conjunctiva of mice [3]. Since then, noninvasive methods such as digital slit-lamps, computer-assisted intravital microscopy (CAIM), retinal function imager (RFI), orthogonal polarization spectroscopy (OPS), EyeFlow™, functional slit-lamp microscopy (FSLB), and optical coherence tomography angiography (OCTA) have emerged and enabled accurate quantitative observations combined with image processing techniques [4].

With the emergence and application of advanced bulbar conjunctival microcirculation observation equipment and new image processing techniques, bulbar conjunctival microcirculation observation has been objective, quantitative, noninvasive, and easy to operate. However, at the same time, due to the lack of unified standards between different devices and the inconsistent observation processes between laboratories, the data obtained by different laboratories are less comparable. In addition, because of the location and physiological characteristics of the bulbar conjunctiva, the bulbar conjunctival microcirculation is susceptible to multiple internal and external environmental factors, making bulbar conjunctival microcirculation alterations lack specificity.

To provide an update on the progress of bulbar conjunctival microcirculation alterations in the diagnosis of ocular diseases in recent five years, a computerized search from January 2017 to March 2022 of the online electronic database PubMed was performed, using the MeSH terms "bulbar conjunctiva" and "vessel". More generalized complementary research regarding bulbar conjunctival microcirculation alterations was also obtained from the PubMed database. A total of 37 records were initially identified. After exclusion of nonrelevant, non-English, and duplicate studies, a total of 17 records were found eligible, all of which were included in this review. Relevant ocular diseases include contact lens wearing, dry eye, conjunctival malignant melanoma, conjunctival nevus, and diabetic retinopathy as reviewed below.

2. Bulbar Conjunctival Microcirculation Parameters

Commonly used bulbar conjunctival microcirculation parameters include bulbar conjunctival blood flow velocity, bulbar conjunctival vessel diameter, bulbar conjunctival blood flow rate, and bulbar conjunctival vessel density.

Bulbar conjunctival blood flow velocity is often calculated by the distance of red blood cells in several consecutive shots of the bulbar conjunctiva, and the accuracy of the measurement is interfered with by eye movements. Jo et al. [5] developed a motion correction algorithm based on deep learning, which opened up a new idea for solving the problem of motion illusion in the measurement of bulbar conjunctival blood flow velocity.

There are many ways to measure bulbar conjunctival vessel diameter, and in the early days, one or more places were manually selected on the image of the bulbar conjunctival vessels for measurement. Uji et al. [6] defined the vessel diameter index as the total area of the region representing the blood vessels in the binary image divided by the total length of the blood vessels in the vascular skeleton image. Jiang et al. [2] calculated bulbar conjunctival vessel diameter by the distance between two points at half of the maximum brightness in the vertical direction of vessels in the bulbar conjunctival vessels image.

Bulbar conjunctival blood flow rate is calculated by the blood flow velocity and the vessel diameter, and the formula is

$$Q = V_s \frac{\pi D^2}{4}. \tag{1}$$

In the formula, Q is the bulbar conjunctival blood flow rate, V_s is the average blood flow velocity of the cross section of the bulbar conjunctiva vessels, and D is the inner diameter of the bulbar conjunctival vessels (the diameter of the vascular cavity). V_s is estimated by the axial blood flow velocity of the bulbar conjunctiva vessels, and the commonly used conversion formula [1] is

$$V_s = \begin{cases} V_{\text{ax}}, & \frac{D}{D_c} \le 0.6, \\ \frac{V_{\text{ax}}}{1.58\left(1 - e^{-\sqrt{2D/D_c}}\right)}, & \frac{D}{D_c} > 0.6. \end{cases} \tag{2}$$

In the formula, V_{ax} is the axial blood flow velocity of the bulbar conjunctiva vessels and D_c is the diameter of human erythrocytes, taking $7.65\,\mu$m [1]. This conversion formula takes into account the uneven velocity of blood flow across the cross section of the blood vessels.

One way to define bulbar conjunctival vessel density is the ratio of the area occupied by blood vessels in the image to the total area of the image, which can be calculated by counting the number of pixels occupied by blood vessels divided by the total number of pixels. However, this method is affected by vessel diameter. The use of bulbar conjunctival vessel length density, i.e., the length of bulbar conjunctival vessels per unit area [6], can exclude the effect of vessel diameter. Another way is fractal, an algorithm that reflects structural complexity and irregularities, and fractal dimensions can reflect the complexity and density of blood vessels [7]. Liu et al. [8] confirmed that the fractal dimension of the bulbar conjunctival vessels is positively correlated with the bulbar conjunctival vessel density obtained by pixel counting.

In addition to the above four main bulbar conjunctival microcirculation parameters, Cheung et al. [9] summarized 15 identifiable abnormal alterations in bulbar conjunctival microcirculation in diabetic patients, including abnormal vessel diameter, abnormal vascular wall thickness, beading, curvature, congestion, distension, injury, hemosiderin deposition, microaneurysm, abnormal vascular distribution, abnormal arteriovenous ratio, ischemic area, obstruction, intermittent blood flow, and abnormal blood flow velocity, and defined the severity index (SI) of abnormal alterations in the bulbar conjunctival microcirculation, that is, the number of anomalous alterations in the bulbar conjunctival microcirculation above, used for CAIM semiquantitative

observation of bulbar conjunctival microcirculation alterations.

The microcirculation parameters of the bulbar conjunctiva are greatly influenced by physiological factors such as respiration and heartbeat, and patients are often allowed to sit still for 10 minutes before measurement [10]. The bulbar conjunctival microcirculation was observed several times a day, and the measured blood flow velocity, vessel diameter [11], and vessel density [12] of the bulbar conjunctiva were stable. In the two observations with a long interval (17 ± 12 weeks apart), vessel density and blood flow rate of the bulbar conjunctiva were still stable [10]. A study on the stability of bulbar conjunctival vessel density in observations with a distant interval is lacking.

The bulbar conjunctival microcirculation is regulated by the nervous and endocrine systems and has a complex self-regulatory mechanism. Alterations in the microcirculation parameters of the bulbar conjunctiva caused by different pathological conditions are often the same, so the alterations in the microcirculation parameters of the bulbar conjunctiva are nonspecific and their significance needs to be discussed under specific pathological conditions. For example, in dry eye, the faster bulbar conjunctival blood flow velocity, the larger bulbar conjunctival vessel diameter, the greater bulbar conjunctival blood flow rate, and the greater bulbar conjunctival vessel density, indicating that the inflammation of the patient's ocular surface is more serious; in diabetes mellitus, a larger SI indicates that the patient has more serious diabetic vasculopathy, and with the progression of diabetic vasculopathy, bulbar conjunctival blood flow velocity, vessel diameter, and vessel density vary differently.

3. Bulbar Conjunctival Microcirculation Alterations in Ocular Diseases

3.1. Contact Lens Wearing-Related Bulbar Conjunctival Microcirculation Alterations. With the increasing demand for refractive correction, myopia prevention, and control and medical cosmetology, the number of contact lens wearers is increasing. However, adverse effects of contact lenses are issues to be paid close attention to. Conjunctival congestion is one of the most common adverse effects of contact lenses [13]. The existing diagnosis of conjunctival congestion mainly relies on qualitative indicators, which are subjective, such as the degree of congestion and vascular contour clarity. Bulbar conjunctival microcirculation alterations can be used to quantitatively analyze bulbar conjunctival congestion, facilitate its early diagnosis, and correct grading and can be used to further predict adverse effects of contact lens wearing and guide contact lens wearing.

Contact lens wearing causes bulbar conjunctival microcirculation alterations through 2 different mechanisms. One is the direct physical action between the corneal contact lens and the bulbar conjunctiva, such as friction causing bulbar conjunctival hyperplasia and the tear crescent, which mainly acts on the corneal limbus. The limbal SI was significantly higher in patients who wore soft contact lenses (>2 years) than in those who did not wear contact lenses. The results showed that vessel diameter at the limbus was significantly increased, blood flow velocity was significantly decreased, and bulbar conjunctiva microvessel injury, hemosiderin deposition, congestion, intermittent blood flow, and bulbar conjunctiva microvessel curvature were significantly increased [14]. The effect of orthokeratology (Ortho-K) on bulbar conjunctiva microcirculation was similar, and the limbal SI of patients who wore Ortho-K (>1 year) was significantly higher than that of those who did not wear contact lenses [9].

The other is that wearing contact lenses can indirectly cause bulbar conjunctiva microcirculation alterations through compensatory mechanisms for inadequate blood supply to the bulbar conjunctiva in the contact area of the corneal contact lens, such as dilation and reopening of bulbar conjunctival vessels [15]. The bulbar conjunctival blood flow velocity, blood flow rate, vessel diameter, and vessel density in the area without contact with the soft contact lens were significantly higher in the patients wearing contact lens (>6 months) than in controls [16, 17], where blood flow velocity was positively correlated with the length of time per day and the number of days per week that contact lenses were worn [16]. Even after a full night's rest, bulbar conjunctival blood flow velocity, blood flow rate, and vessel density in habitual (>3 years) contact lens wearers were still greater than those in noncontact lens wearers [17], suggesting that contact lens wearing may cause chronic inflammation of the ocular surface and short periods of rest is not enough to restore damage caused by contact lenses. In addition, wearing contact lenses can also cause short-term alterations in the bulbar conjunctival microcirculation parameters. Blood flow velocity, blood flow rate, vessel diameter, and vessel density of bulbar conjunctiva increased after 6 hours of wearing the soft contact lens, regardless of whether the subjects have worn contact lenses previously [2, 15]. Moreover, the comfort degree of contact lens wearers was positively correlated with bulbar conjunctival blood flow velocity and negatively correlated with bulbar conjunctival vessel density [18].

However, there are currently no studies of bulbar conjunctival microcirculation alterations associated with the wearing of rigid gas-permeable contact lenses. In addition, most of the research on the bulbar conjunctival microcirculation alterations associated with the wearing of contact lenses is limited to observation, and there is a lack of exploration of the diagnosis and grading of conjunctival hyperemia using bulbar conjunctival microcirculation alterations.

3.2. Dry Eye-Related Bulbar Conjunctival Microcirculation Alterations. Dry eye is a multifactorial ocular surface disease characterized by homeostasis of the tear film and accompanied by symptoms of ocular discomfort, which seriously affects the quality of life. At present, most clinical dry eye examination and diagnostic methods have the limitations of high subjectivity and lack of objective quantitative indicators and analysis. Ocular surface inflammation is one of the main pathophysiological mechanisms of dry eye [19], and its primary clinical manifestation is conjunctival hyperemia. When the ocular surface is inflamed, due to the increase in the secretion of vasomotor substances such as NO, the

vessels dilate and congest, bulbar conjunctival vessel diameter and blood flow velocity increase, and if chronic inflammation occurs, vessel density will also increase under the action of angiogenesis factors such as VEGF [20]. The use of bulbar conjunctival microcirculation alterations allows for quantitative analysis of bulbar conjunctival hyperemia, which helps to improve the sensitivity, specificity, and efficiency of dry eye diagnosis [21].

According to Chen et al. [22], blood flow velocity, blood flow rate, vessel diameter, and vessel density of bulbar conjunctiva in patients with dry eye were significantly higher than those in healthy people. Among them, the areas under the curve of the receiver operating characteristic with bulbar conjunctival vessel diameter and blood flow rate as diagnostic indicators of dry eye were 0.861 and 0.856, respectively, comparable with the ocular surface disease index (OSDI) [23] and the noninvasive tear film break-up time [24, 25], indicating that bulbar conjunctival vessel diameter and blood flow rate have good sensitivity and specificity as diagnostic indicators for dry eye. In addition, bulbar conjunctival vessel density in patients with dry eye was positively correlated with their OSDI, which may mean that bulbar conjunctival vessel density can reflect the symptoms and subjective feelings of patients with dry eye [22]. Moreover, patients with dry eye have significantly reduced bulbar conjunctival blood flow velocity, blood flow rate, vessel diameter, and vessel density after receiving local anti-inflammatory therapy [26], which further demonstrated that the bulbar conjunctival microcirculation alterations reflected the severity of ocular surface inflammation and contributed to the monitoring of the effect of dry eye treatment.

3.3. Conjunctival Malignant Melanoma- and Conjunctival Nevus-Related Bulbar Conjunctival Microcirculation Alterations. Conjunctival malignant melanoma is a potentially fatal tumor, while conjunctival nevus is a congenital benign hamartoma derived from the neuroectoderm, which is rarely malignant, and the differential diagnosis of the two is difficult, requiring histopathological examination [27] and the difference in the bulbar conjunctival microcirculation alterations at the lesion is one of the potential distinguishing indicators. In the past, fluorescein angiography was used to observe the bulbar conjunctival microcirculation alterations at the lesion, which had the disadvantages of invasive, time-consuming, and qualitative observation.

Brouwer et al. [28] attempted to use OCTA to distinguish conjunctival nevus from conjunctival malignant melanoma. They examined the density and curvature of the bulbar conjunctiva vessels in the lesions of conjunctival nevus, conjunctival malignant melanoma, and primary acquired melanosis and found that there was no significant difference between vessel density at the site of conjunctival malignant melanoma lesion and conjunctival nevus; both of which were lower than the normal vessel density, and the vessels were more curved than the normal bulbar conjunctival vessels, while vessel density at primary acquired melanosis was similar to that at the normal bulbar conjunctiva. Their study failed to distinguish conjunctival nevus from conjunctival malignant melanoma. Future studies using bulbar conjunctival microcirculation alterations to identify conjunctival malignant melanoma and conjunctival nevus could consider exploring more bulbar conjunctival microcirculation parameters or switching to other imaging devices.

3.4. Diabetic Retinopathy-Related Bulbar Conjunctival Microcirculation Alterations. Diabetic retinopathy (DR) is the most common retinal vasculopathy and is one of the leading blinding ocular diseases in people over 50 years of age [29]. According to the severity, retinopathy can be divided into nonproliferative diabetic retinopathy (NPDR) and proliferative diabetic retinopathy (PDR). Patients with DR are visually impaired and difficult to reverse, but reasonable interventions can be implemented to stop their progression [30]. Therefore, the prevention and early diagnosis of DR are very important. The gold standard for DR diagnosis is ophthalmic fundus examination, which often requires dilated pupils and is not suitable for large-scale screening [31]. Alterations in the bulbar conjunctival microcirculation reflect the severity of diabetic vasculopathy, with sensitivity and specificity as diagnostic indicators of type 2 diabetes reaching 78.70% and 69.08% [32]. And its observation has the advantages of simple operation, short time consumption, and no need to pretreat patients, and it is promising to be applied to the early diagnosis or large-scale screening of diabetic retinopathy.

Patients with DR have multiple bulbar conjunctival microcirculation alterations. Schuerch et al. [33] found that there was no significant difference between bulbar conjunctival vessel density in no clinically visible diabetic retinopathy (NDR) patients and healthy controls, while DR patients (did not distinguish between NPDR and PDR) had significantly lower bulbar conjunctival vessel density than healthy people. NDR and NPDR patients had larger bulbar conjunctival venule diameter than healthy people [34].

Patterns of alterations in bulbar conjunctival blood flow velocity in DR patients are complex and controversial. Khansari et al. [34] found that the bulbar conjunctival arteriolar blood flow velocity in NDR patients was significantly smaller than that in healthy people, but there was no significant difference between the arteriolar blood flow velocity in NPDR patients and healthy people. In patients with PDR, the bulbar conjunctival arteriolar blood flow velocity was not significantly different from that of healthy people, but the venular blood flow velocity was greater than that of healthy people. Hwang et al. [35] found that the venular blood flow velocity showed a pattern of first increasing and then decreasing in healthy people, diabetic patients without diabetic complications, and diabetic patients with diabetic complications. Both patients with NDR and diabetes without diabetic complications had lower levels of diabetic vasculopathy, but in the two studies described above, the alterations in bulbar conjunctival blood flow velocity in the two studies were reversed, possibly due to the different types of blood vessels observed (arterioles/venules), different blood vessel diameters, or different circumstances of studying ethnicity, age, and whether subjects have other diseases within each group. Despite the controversy, both studies suggested that early diabetic vasculopathy causes alterations in bulbar

conjunctival blood flow velocity, which has the potential to screen for early diabetic vasculopathy, particularly retinopathy. Further studies should focus on how to synthesize the bulbar conjunctival microcirculation parameters to improve the sensitivity and specificity of diabetic retinopathy screening. And longitudinal cohort studies are desperately needed to determine whether bulbar conjunctival microcirculation alterations can predict the occurrence of diabetic retinopathy before other abnormalities are found.

4. Conclusions

The translucent nature of the bulbar conjunctiva makes it possible to assist in the diagnosis of ocular diseases by assessing bulbar conjunctival microcirculation alterations noninvasively. In recent years, with the continuous emergence and application of new image acquisition devices and image processing techniques, bulbar conjunctival microcirculation has played an important role in the diagnosis of many ocular diseases and has become more and more refined and automated.

There are still some problems with the current study of bulbar conjunctival microcirculation. The vast majority of studies have been limited to the use of bulbar conjunctival microcirculation alterations as a means of basic study, with fewer assessments of their diagnostic potential. There are two main reasons for this; first, a variety of diseases and physiological states may trigger bulbar conjunctival microcirculation alterations in a similar way, which makes the bulbar conjunctival microcirculation alterations cannot be independently used as a diagnostic indicator of a disease, but only as an auxiliary diagnostic indicator or grading indicator. In addition, the data obtained by different imaging equipment, image processing methods, and algorithms are not uniform, and there is no standardized procedure for bulbar conjunctival microcirculation exploration, which makes the data obtained by different laboratories not comparable.

There is still a wide range of exploration space for research on bulbar conjunctival microcirculation alterations. It will be a series of emerging fields to study and analyze the differences between multiple imaging equipment, image processing methods, and algorithms, update imaging equipment and algorithms, and concrete bulbar conjunctival microcirculation alterations as indicators for ocular diseases with large-scale research.

Conflicts of Interest

The authors declare that there is no conflict of interest regarding the publication of this paper.

Authors' Contributions

Zhengze Sun and Yaxin Li contributed equally to this work.

Acknowledgments

This work was supported by the National Natural Science Foundation of China (82171022 and 81974128) and the Capital Health Research and Development of Special (2020-2-4097).

References

[1] A. G. Koutsiaris, S. V. Tachmitzi, N. Batis et al., "Volume flow and wall shear stress quantification in the human conjunctival capillaries and post-capillary venules in vivo," *Biorheology*, vol. 44, no. 5-6, pp. 375–386, 2007.

[2] H. Jiang, J. Zhong, D. C. DeBuc et al., "Functional slit lamp biomicroscopy for imaging bulbar conjunctival microvasculature in contact lens wearers," *Microvascular Research*, vol. 92, pp. 62–71, 2014.

[3] E. Laemmel, M. Genet, G. Le Goualher, A. Perchant, J. F. Le Gargasson, and E. Vicaut, "Fibered confocal fluorescence microscopy (Cell-viZio) facilitates extended imaging in the field of microcirculation. A comparison with intravital microscopy," *Journal of Vascular Research*, vol. 41, no. 5, pp. 400–411, 2004.

[4] G. G. Wei Rong and S. Yi, "Research in imaging of conjunctival microcirculation," *Int Rev Ophthalmol*, vol. 42, pp. 199–203, 2018.

[5] H. C. Jo, H. Jeong, J. Lee, K. S. Na, and D. Y. Kim, "Quantification of blood flow velocity in the human conjunctival microvessels using deep learning-based stabilization algorithm," *Sensors*, vol. 21, no. 9, article 3224, 2021.

[6] A. Uji, S. Balasubramanian, J. Lei, E. Baghdasaryan, M. Al-Sheikh, and S. R. Sadda, "Impact of multiple en face image averaging on quantitative assessment from optical coherence tomography angiography images," *Ophthalmology*, vol. 124, no. 7, pp. 944–952, 2017.

[7] S. Dinesen, P. S. Jensen, M. Bloksgaard et al., "Retinal vascular fractal dimensions and their association with macrovascular cardiac disease," *Ophthalmic Research*, vol. 64, no. 4, pp. 561–566, 2021.

[8] Z. Liu, H. Wang, H. Jiang, G. R. Gameiro, and J. Wang, "Quantitative analysis of conjunctival microvasculature imaged using optical coherence tomography angiography," *Eye and Vision*, vol. 6, no. 1, pp. 1–9, 2019.

[9] A. T. W. Cheung, P. C. Y. Chen, K. Y. Wong, A. Banerjee, B. D. Tracy, and To W J, "Microvascular complications in orthokeratology (Ortho-K): a real-time study on the microvasculature of the bulbar conjunctiva in Ortho-K treatment," *Clinical Hemorheology and Microcirculation*, vol. 72, no. 2, pp. 119–128, 2019.

[10] M. M. Khansari, M. Tan, P. Karamian, and M. Shahidi, "Intervisit variability of conjunctival microvascular hemodynamic measurements in healthy and diabetic retinopathy subjects," *Microvascular Research*, vol. 118, pp. 7–11, 2018.

[11] Z. Xu, H. Jiang, A. Tao et al., "Measurement variability of the bulbar conjunctival microvasculature in healthy subjects using functional slit lamp biomicroscopy (FSLB)," *Microvascular Research*, vol. 101, pp. 15–19, 2015.

[12] S. Cai, F. Zhao, and C. Du, "Repeatability of ocular surface vessel density measurements with optical coherence tomography angiography," *BMC Ophthalmology*, vol. 19, no. 1, pp. 1–6, 2019.

[13] M Society of Contact Lens Safety and A Vision Health of Chinese Health, "Expert consensus on diagnosis and treatment of adverse reactions of contact lens wear in China (2021)," *Zhonghua Yan Ke Za Zhi*, vol. 57, no. 8, pp. 573–579, 2021.

[14] A. T. W. Cheung, B. S. Hu, S. A. Wong et al., "Microvascular abnormalities in the bulbar conjunctiva of contact lens users," *Clinical Hemorheology and Microcirculation*, vol. 51, pp. 77–86, 2012.

[15] W. Chen, Z. Xu, H. Jiang, J. Zhou, L. Wang, and J. Wang, "Altered bulbar conjunctival microcirculation in response to contact lens wear," *Eye Contact Lens*, vol. 43, no. 2, pp. 95–99, 2017.

[16] L. Hu, C. Shi, H. Jiang, Y. Shi, Z. Sethi, and J. Wang, "Factors affecting microvascular responses in the bulbar conjunctiva in habitual contact lens wearers," *Investigative Ophthalmology & Visual Science*, vol. 59, no. 10, pp. 4108–4114, 2018.

[17] Y. Shi, L. Hu, W. Chen, D. Qu, H. Jiang, and J. Wang, "Evaluated conjunctival blood flow velocity in daily contact lens wearers," *Eye Contact Lens*, vol. 44, Suppl 1, pp. S238–Ss43, 2018.

[18] Q. Chen, H. Jiang, and J. Wang, "Conjunctival vascular adaptation related to ocular comfort in habitual contact lens wearers," *American Journal of Ophthalmology*, vol. 216, pp. 99–109, 2020.

[19] J. S. Wolffsohn, R. Arita, R. Chalmers et al., "TFOS DEWS II Diagnostic Methodology report," *The Ocular Surface*, vol. 15, no. 3, pp. 539–574, 2017.

[20] V. L. Perez, M. E. Stern, and S. C. Pflugfelder, "Inflammatory basis for dry eye disease flares," *Experimental Eye Research*, vol. 201, article 108294, 2020.

[21] M. Rolando and S. Barabino, "Are there clinical ways to assess inflammation in dry eye disease?," *Ocular Immunology and Inflammation*, vol. 29, no. 6, pp. 1183–1189, 2021.

[22] W. Chen, Y. Deng, H. Jiang et al., "Microvascular abnormalities in dry eye patients," *Microvascular Research*, vol. 118, pp. 155–161, 2018.

[23] T. S. Kang, J. Cho, J. Kim et al., "Modified ocular surface disease index as a screening criteria for dry eye syndrome presenting after successful dacryocystorhinostomy," *PLoS One*, vol. 16, no. 2, article e0247168, 2021.

[24] E. Muhafiz and M. S. Demir, "Ability of non-invasive tear break-up time to determine tear instability in contact lens wearers," *International Ophthalmology*, vol. 42, no. 3, pp. 959–968, 2022.

[25] W. W. Binotti, B. Bayraktutar, M. C. Ozmen, S. M. Cox, and P. Hamrah, "A review of imaging biomarkers of the ocular surface," *Eye Contact Lens*, vol. 46, Suppl 2, pp. S84–s105, 2020.

[26] Y. Deng, W. Chen, P. Xiao et al., "Conjunctival microvascular responses to anti-inflammatory treatment in patients with dry eye," *Microvascular Research*, vol. 131, article 104033, 2020.

[27] C. L. Shields and J. A. Shields, "Tumors of the conjunctiva and cornea," *Survey of Ophthalmology*, vol. 49, no. 1, pp. 3–24, 2004.

[28] N. J. Brouwer, M. Marinkovic, J. C. Bleeker, M. J. Jager, and G. P. M. Luyten, "Anterior Segment OCTA in pigmented lesions of the conjunctiva and iris," *Acta Ophthalmologica*, vol. 98, 2020.

[29] L. Yin, D. Zhang, Q. Ren, X. Su, and Z. Sun, "Prevalence and risk factors of diabetic retinopathy in diabetic patients: a community based cross-sectional study," *Medicine*, vol. 99, no. 9, article e19236, 2020.

[30] R. Raman, R. Krishnan, K. Ramasamy, and S. Natarajan, "Diabetic retinopathy: a right time to intervene," *Indian Journal of Ophthalmology*, vol. 68, no. 2, pp. 305-306, 2020.

[31] S. Vujosevic, S. J. Aldington, P. Silva et al., "Screening for diabetic retinopathy: new perspectives and challenges," *Lancet Diabetes Endocrinology*, vol. 8, no. 4, pp. 337–347, 2020.

[32] X. Li, C. Xia, X. Li et al., "Identifying diabetes from conjunctival images using a novel hierarchical multi-task network," *Scientific Reports*, vol. 12, no. 1, pp. 1–9, 2022.

[33] K. Schuerch, H. Frech, and M. Zinkernagel, "Conjunctival microangiopathy in diabetes mellitus assessed with optical coherence tomography angiography," *Translational Vision Science & Technology*, vol. 9, no. 6, 2020.

[34] M. M. Khansari, J. Wanek, M. Tan et al., "Assessment of conjunctival microvascular hemodynamics in stages of diabetic microvasculopathy," *Scientific Reports*, vol. 7, pp. 1–9, 2017.

[35] J. Hwang, V. Karanam, J. Wang et al., "Conjunctival vessels in diabetes using functional slit lamp biomicroscopy," *Cornea*, vol. 40, no. 8, pp. 950–957, 2021.

Hindawi
Disease Markers
Volume 2022, Article ID 4988256, 6 pages
https://doi.org/10.1155/2022/4988256

Research Article

Development and Application of an Intelligent Diagnosis System for Retinal Vein Occlusion Based on Deep Learning

Wei Xu,[1,2] **Zhipeng Yan**,[3] **Nan Chen**,[3] **Yuxin Luo**,[3] **Yuke Ji**,[3] **Minli Wang**,[4] **and Zhe Zhang**[5]

[1]*Department of Optometry, Jinling Institute of Technology, Nanjing, Jiangsu, China*
[2]*Nanjing Key Laboratory of Optometric Materials and Application Technology, Nanjing, Jiangsu, China*
[3]*The Laboratory of Artificial Intelligence and Big Data in Ophthalmology, Affiliated Eye Hospital of Nanjing Medical University, Nanjing, Jiangsu, China*
[4]*The First Affiliated Hospital of Huzhou University, Huzhou, Zhejiang, China*
[5]*Shenzhen Eye Hospital, Jinan University, Shenzhen, Guangdong, China*

Correspondence should be addressed to Minli Wang; wangminli1981@163.com and Zhe Zhang; whypotato@126.com

Received 26 June 2022; Revised 11 August 2022; Accepted 16 August 2022; Published 24 August 2022

Academic Editor: Yi Shao

This study is aimed at developing an intelligent algorithm based on deep learning and discussing its application for the classification and diagnosis of retinal vein occlusions (RVO) using fundus images. A total of 501 fundus images of healthy eyes and patients with RVO were used for model training and testing to investigate an intelligent diagnosis system. The images were first classified into four categories by fundus disease specialists: (i) healthy fundus (group 0), (ii) branch RVO (BRVO) (group 1), (iii) central RVO (CRVO) (group 2), and (iv) macular branch RVO (MBRVO) (group 3), before being diagnosed using the ResNet18 network model. Intelligent diagnoses were compared with clinical diagnoses. The specificity of the intelligent diagnosis system under each attention mechanism was 100% in group 0 and also revealed a high sensitivity of over 95%, $F1$ score of over 97%, and an accuracy of over 97% in this group. For the other three groups, the specificities of diagnosis ranged from 0.45 to 0.91 with different attention mechanisms, in which the ResNet18+coordinate attention (CA) model had the highest specificities of 0.91, 0.88, and 0.83 for groups 1, 2, and 3, respectively. It also provided a high accuracy of over 94% with a coordinate attention mechanism in all four groups. The intelligent diagnosis and classifier system developed herein based on deep learning can determine the presence of RVO and classify disease according to the site of occlusion. This proposed system is expected to provide a new tool for RVO diagnosis and screening and will help solve the current challenges due to the shortage of medical resources.

1. Introduction

Retinal vein occlusion (RVO) is a common retinal vascular degenerative disease with an increasing prevalence in individuals aged 30–89 years, which makes the blindness rate higher than that of other retinal vascular disorders besides diabetic retinopathy [1]. Characterized by retinal vein filling, proximal vascular occlusion, distal vascular dilation, retinal hemorrhage, and edema due to ischemia and hypoxia, possible causes of RVO include external compression or disease of the vein wall, such as vasculitis [2, 3]. Based on the location of the blocked blood vessels, RVO can be divided into two primary categories depending on the site of occlusion: branch RVO (BRVO) and central RVO (CRVO) [4]. Sight-threatening complications of RVO include macular edema, macular ischemia, and vitreous hemorrhage due to retinal neovascularization. This damages the visual function of patients and even causes permanent and irreversible vision loss [5–7].

The treatment of RVO mainly focuses on its etiology including hypertension, arteriosclerosis, and inflammation and complications, such as macular edema, ischemia, and neovascularization [8]. Currently, intravitreal therapy is an economical and effective method for the treatment of this

disease [9]. In addition, laser photocoagulation has been recommended for patients with neovascularization and macular edema, and many surgical treatment modalities have been reported for critical patients [8, 10]. The choice of treatment should be personalized to the individual patient for different subtypes of RVO; therefore, diagnosis and differential diagnosis are important. Fundus examination and fundus photography are important methods for the preliminary evaluation of RVO. Other imaging diagnostic methods, such as fluorescein angiography (FA) and optical coherence tomography (OCT), are also widely used for detection and evaluation [11].

With the wide application of deep learning in the field of image recognition, an increasing number of ophthalmologists and intelligent technologists have begun to explore image recognition and classification technologies based on deep learning and apply it to the clinical diagnosis and treatment of retinal diseases. Chandrakumar et al. [12] classified fundus images using a 13-layer convolutional neural network. Ardiyanto et al. [13] proposed a compact deep learning algorithm with small, embedded plates for detecting diabetic retinopathy. Kermany et al. [14] established a classifier system for screening age-related macular degeneration (AMD) and diabetic macular edema, utilizing transfer learning on a dataset of OCT images. Li et al. [15] proposed an OCT image segmentation algorithm based on a 3D neural network to solve the problem of retinal fluid segmentation. Wan [16] presented a convolutional neural network named EAD-Net that can achieve pixel-level accuracy for different types of lesions in diabetic retinopathy. Xu et al. [17] proposed two biomarker segmentation schemes integrating the semiautomatic localization technique and the low-rank and sparse decomposition theory to locate the leakage area in laser surgery of chronic central serous chorioretinopathy. Promoting the deep integration of artificial intelligence (AI) and medical care will help alleviate problems due to shortage of specialized medical resources in China and will improve the efficiency of disease screening. This study is aimed at developing an intelligent algorithm based on deep learning and discussing its application for the classification and diagnosis of RVO using fundus images, expected to aid in promoting the early diagnosis and treatment of treatable RVO cases, thereby achieving better prognosis.

2. Materials and Methods

2.1. Ethical Approval. This study was approved by the Institutional Research Ethics Committee of Nanjing Medical University and followed the tenets of the Declaration of Helsinki. All fundus photographs were anonymized before inclusion and contained no information of the patients, except for the diagnoses.

2.2. Image Acquisition and Preprocessing. The dataset used in this study was acquired from the Eye Hospital affiliated with Nanjing Medical University and contained 501 fundus images. All photographs were taken using a nonmydriatic fundus camera over 45° of the posterior pole. The fundus images were complied with Chinese annotation and quality control specifications for fundus colour photographs [18], and data anonymization was applied before the study.

The images were classified into four categories by fundus disease specialists as follows: (i) healthy fundus (group 0), (ii) BRVO (group 1), (iii) central CRVO (group 2), and (iv) MBRVO (group 3) (as shown in Figure 1). Then, they were randomly allocated into the test, training, and validation sets. The samples of the training set and the other two sets were divided in a ratio of 2 : 8 (Table 1).

The dataset covering 501 photographs was not adequate for the deep convolutional neural network in this study; therefore, it was augmented to decrease the phenomenon of overfitting. Only the original data were appropriately transformed without changing the amount of original data or introducing any irrelevant data to increase the sample data and improve the generalizability of the model. Data augmentation was applied only to the training set in an online form, which was omitted from the statistics. The methods of adjustment included image inversion, image rotation, image compression, image random cropping, brightness adjustment, and gamma correction.

2.3. Model Training and Evaluation. The main network framework used in this study was a convolutional neural network called ResNet18, which is a fusion of the inception and residual networks. The basic architecture of the ResNet18 model includes convolutional, max pooling, and activation layers and a fully connected layer (Figure 2). The batch size of the model was four per card, and the gradual warmup method was used for learning rate optimization. A total of 50 epochs were trained, with a learning rate set between 10^{-2} and 10^{-5}. The best learning rate was selected by comparing the output results for different learning rates. One of the three attention mechanisms, coordinate attention (CA), convolutional block attention module (CBAM), and squeeze and excitation network (SENet), was added to the basic network model of ResNet18 for the controlled study. Networks with different attention mechanisms were trained on the same dataset and treated them in the same way.

Intelligent diagnosis was performed based on fundus images. The same images were consulted by three retinal specialists in a double-blind trial. Final clinical diagnostic results were created for two or more identical grading diagnoses, taken as the expert diagnosis. The sensitivity, specificity, $F1$ score, and accuracy of the intelligent diagnosis system were calculated by comparing the results of expert and intelligent diagnoses.

2.4. Statistical Analysis. Statistical analyses were conducted by SPSS 24.0. Enumeration data were represented by the number of images and indicators including accuracy, specificity, sensitivity, and $F1$ score.

3. Results

In this study, 501 fundus images were used to evaluate the proposed intelligent grading and diagnosis system for RVO. According to the analysis of the above results, the

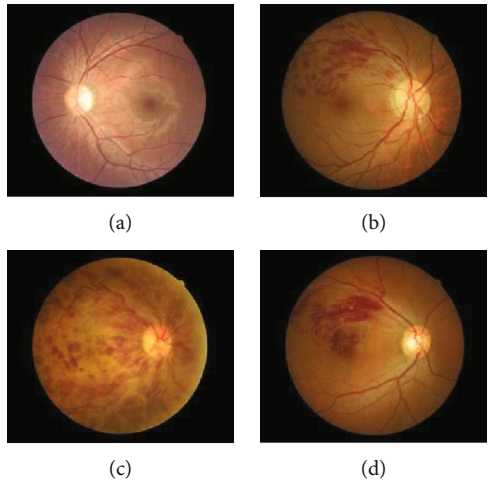

Figure 1: Four categories of the fundus images. (a) Group 0: healthy fundus. (b) Group 1: branch retinal vein occlusion (BRVO). (c) Group 2: central retinal vein occlusion (CRVO). (d) Group 3: macular branch retinal vein occlusion (MBRVO).

Table 1: Dataset.

n	Test set	Training set	Validation set	Total
Group 0 (healthy fundus)	62	166	31	259
Group 1 (BRVO)	24	76	17	117
Group 2 (CRVO)	14	45	10	69
Group 3 (MBRVO)	12	36	8	56
Total	112	323	66	501

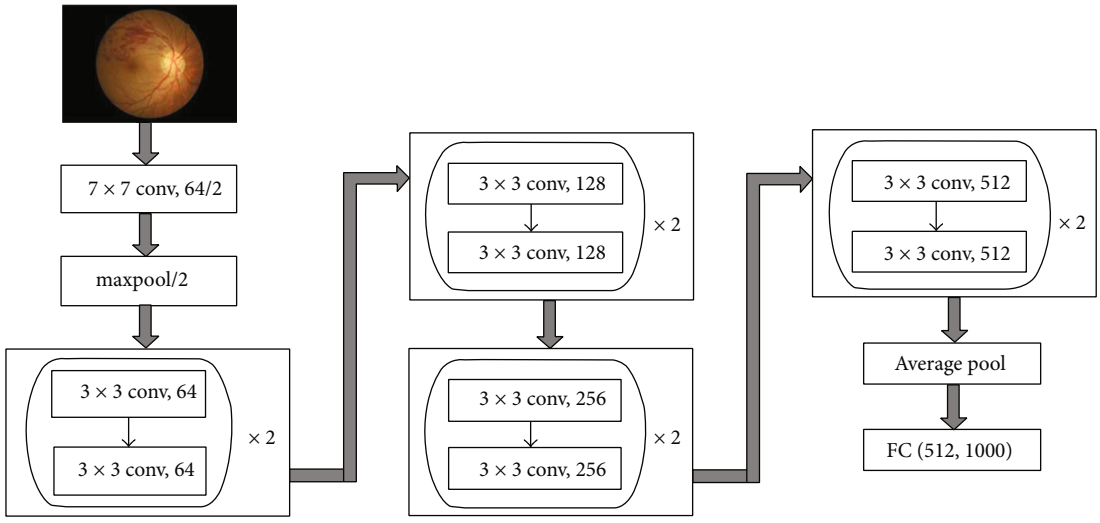

Figure 2: Architectural diagram of ResNet18.

training effect of the model achieved the best results, with a learning rate of 10^{-5}. Therefore, the learning rate was set at 10^{-5} and the other parameters remained unchanged. The training results of different networks were compared.

Compared with the expert diagnosis, the positive predictive value (PPV) and specificity of the intelligent diagnosis system under each attention mechanism were almost 100% in group 0. The method also provided a high sensitivity of over 95% and an accuracy of over 97% in this group. For the other three groups, the specificities of diagnosis differed from 0.45 to 0.91 with different attention mechanisms, in which the ResNet18+CA model had the highest specificities of 0.91, 0.88, and 0.83 in groups 1, 2, and 3, respectively. The highest sensitivities for the intelligent diagnosis were 100%

Table 2: Evaluation index results of different models.

Model	Evaluation indicators	Group			
		Group 0	Group 1	Group 2	Group 3
ResNet18	Specificity	1.0000	0.5333	0.5556	0.5000
	Sensitivity	0.9516	0.6667	0.3517	0.5833
	*F*1 score	0.9752	0.5926	0.4348	0.5385
	Accuracy	0.9732	0.8036	0.8839	0.8929
ResNet18+SE	Specificity	1.0000	0.6500	0.6923	0.4500
	Sensitivity	0.9516	0.5417	0.6429	0.7500
	*F*1 score	0.9752	0.5909	0.6667	0.5625
	Accuracy	0.9732	0.8393	0.9196	0.8750
ResNet18+CBAM	Specificity	1.0000	0.6800	0.6429	0.6667
	Sensitivity	0.9839	0.7083	0.6429	0.6667
	*F*1 score	0.9919	0.6939	0.6429	0.6667
	Accuracy	0.9911	0.8661	0.9107	0.9286
ResNet18+CA	Specificity	1.0000	0.9091	0.8750	0.8333
	Sensitivity	1.0000	0.8333	1.0000	0.8333
	*F*1 score	1.0000	0.8696	0.9333	0.8333
	Accuracy	1.0000	0.9464	0.9821	0.9643

in group 0 and 100% in group 2. Overall, the intelligent diagnosis system provided a high accuracy of over 94% with a coordinate attention mechanism in all four groups (Table 2).

4. Discussion

The aim of this study was to investigate the possibility of constructing an intelligent diagnosis of RVO from fundus photographs using deep learning-based algorithms. Owing to the lack of fundus specialists, screening for RVO is difficult in areas lacking medical resources. The results of this study show that the deep learning model has high specificity, sensitivity, and accuracy for RVO detection and diagnosis. It also enables mass screening for fundus diseases in remote and rural areas.

Anitha et al. [19] evaluated 420 abnormal retinal images from four different categories (nonproliferative diabetic retinopathy (DR), CRVO, central serous retinopathy, and central neovascularization membrane). The authors used 95 images from CRVO for image classification using an identification technique for abnormal fundus images based on the Kohonen neural network (KNN). It showed a sensitivity of 0.97, specificity of 0.99, and an accuracy of 98% for CRVO detection. Zheng et al. [20] proposed a five-category intelligent auxiliary diagnosis model for common fundus diseases, including RVO, high myopia, glaucoma, and DR. The evaluation indicators of sensitivity, specificity, and *F*1 score were 88.27%, 95.99%, and 83.14%, respectively, in the RVO group. Overall, these results indicate that AI can identify RVO efficiently based on their appearance.

Previous studies have focused on RVO. Nagasato et al. [21, 22] created a deep convolutional neural network (DNN) model and trained it using preprocessed image data of CRVO and BRVO cases and that of non-RVO samples. The findings suggested that the proposed DNN model may be useful in diagnosing RVO by identifying suspected retinal hemorrhages, and the deep learning model has higher sensitivity, specificity, and AUC values than the support vector machine model for detecting RVO in fundus photographs. Thus, the proposed intelligent technique can aid in accurate diagnosis based on fundus images without human input and can be used for RVO screening and early diagnosis at a low cost for a large number of patients.

In this study, the network performance improved when the attention mechanism was added, among which the ResNet18+CA achieved the best performance. The classification effect of the different networks for group 0 was better than that of the other three groups. The possible reason was that group 0, as healthy fundus images, accounted for the largest percentage in the whole dataset, and the number of the other three groups, including CRVO, BRVO, and MBRVO, shares an uneven proportion. In addition, the quality of the fundus images of different RVO types in the dataset varied greatly. The fundus images of BRVO, CRVO, and MBRVO showed significant differences in size, shape, brightness, and other aspects (Figures 3–5), whereas the healthy fundus images showed minimal difference in these aspects and were better in quality than the other three types (Figure 6). Therefore, the training results for the fundus images of group 0 were better than those for the other three groups. Similar findings were reported by Chen et al. [23].

Despite the above findings, this study had a few limitations. As suggested in the results, the intelligent diagnosis was less sensitive in groups 1 to 3 than in group 0, indicating further optimization and investigation of the diagnostic model. In future studies, the samples for model

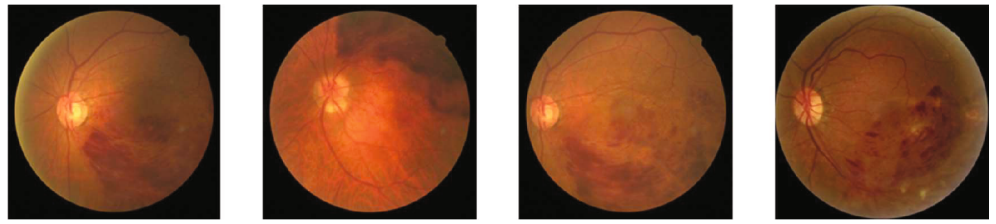

Figure 3: Examples of group 1 (BRVO).

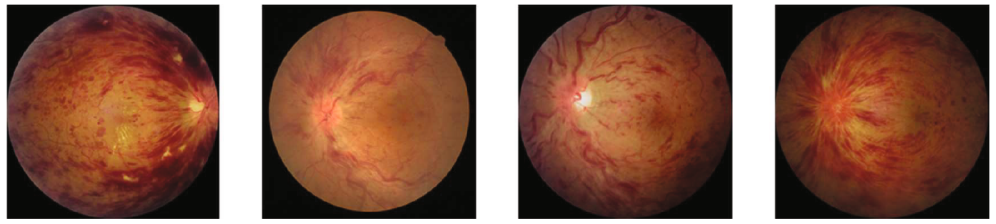

Figure 4: Examples of group 2 (CRVO).

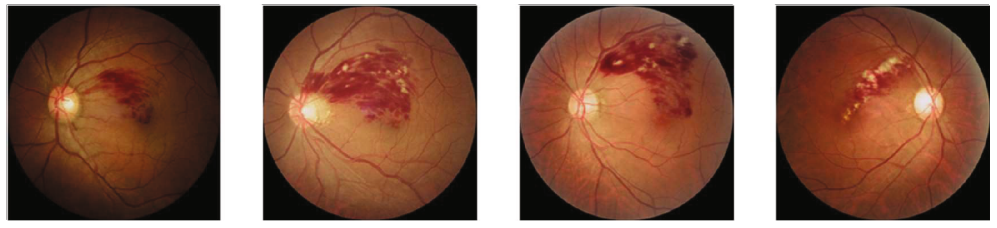

Figure 5: Examples of group 3 (MBRVO).

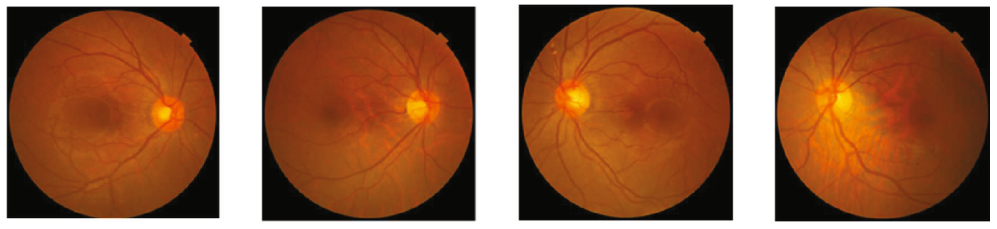

Figure 6: Examples of group 0 (healthy fundus).

training should be enlarged, and the quality of the images should be controlled, as these elements are significant for model training and testing. With the development of artificial intelligence in ophthalmology, eye care practitioners have a better understanding of intelligent diagnosis than other professional technicians [24]. We expect more cooperation between ophthalmologists and experts in the field of artificial intelligence in attempt to define a more concise network model to reduce operating costs. Proceeding to the next stages, we consider comparing the accuracy of RVO diagnosis system with ophthalmologists of different stage and incorporating research on single RVO disease in multiple fundus diseases, to make the intelligent diagnosis system a better landing in clinic. Due to the lack of specialized ophthalmologists in remote or rural areas, screening for fundus diseases such as RVO still faces a huge gap. We expected to help promote the integration of artificial intelligence and healthcare and to solve the current medical resource shortage in the "last kilometer" in China.

5. Conclusions

This proposed system is expected to provide a new tool for RVO diagnosis and screening and will help solve the current challenges due to the shortage of medical resources.

This study focused on expanding the core theoretical models and key techniques required in the intelligent diagnosis for RVO. Based on deep learning algorithm, the intelligent diagnosis and classifier system developed herein can determine the presence of RVO and preferably classify disease according to the site of occlusion, and the intelligent diagnosis achieved was highly consistent with clinical diagnosis in all groups with the addition of the ResNet18 +CA model.

Data Availability

The raw data supporting the conclusions of this article will be made available by the authors, without undue reservation.

Conflicts of Interest

The authors declare that the research was conducted in the absence of any commercial or financial relationships that could be construed as a potential conflict of interest.

Authors' Contributions

Wei Xu, Zhipeng Yan, and Nan Chen contributed equally to this work. Wei Xu acquired and analyzed the data and drafted the manuscript. Zhipeng Yan and Nan Chen acquired and analyzed the data. Yuke Ji and Yuxin Luo drafted the manuscript. Minli Wang and Zhe Zhang designed the research, acquired the clinical information, and revised the manuscript.

Acknowledgments

This study was supported by the Medical Science and Technology Development Project Fund of Nanjing (Grant No. YKK21262).

References

[1] P. Song, Y. Xu, M. Zha, Y. Zhang, and I. Rudan, "Global epidemiology of retinal vein occlusion: a systematic review and meta-analysis of prevalence, incidence, and risk factors," *Journal of Global Health*, vol. 9, no. 1, 2019.

[2] A. Patel, C. Nguyen, and S. Lu, "Central retinal vein occlusion: a review of current evidence-based treatment options," *Middle East African Journal of Ophthalmology*, vol. 23, no. 1, pp. 44–48, 2016.

[3] J. P. Ehlers, S. J. Kim, S. Yeh et al., "Therapies for macular edema associated with branch retinal vein occlusion: a report by the American Academy of Ophthalmology," *Ophthalmology*, vol. 124, no. 9, pp. 1412–1423, 2017.

[4] M. Laouri, E. Chen, M. Looman, and M. Gallagher, "The burden of disease of retinal vein occlusion: review of the literature," *Eye*, vol. 25, no. 8, pp. 981–988, 2011.

[5] N. L. B. Christoffersen and M. Larsen, "Pathophysiology and hemodynamics of branch retinal vein occlusion," *Ophthalmology*, vol. 106, no. 11, pp. 2054–2062, 1999.

[6] P. S. Prasad, S. Oliver, R. E. Coffee, J. P. Hubschman, and S. D. Schwartz, "Ultra wide-field angiographic characteristics of branch retinal and hemicentral retinal vein occlusion," *Ophthalmology*, vol. 117, no. 4, pp. 780–784, 2010.

[7] R. F. Spaide, "Retinal vascular cystoid macular EDEMA," *Retina*, vol. 36, no. 10, pp. 1823–1842, 2016.

[8] G. Coscas, A. Loewenstein, A. Augustin et al., "Management of retinal vein occlusion–consensus document," *Ophthalmologica*, vol. 226, no. 4–28, 2011.

[9] A. Pielen, N. Feltgen, C. Isserstedt, J. Callizo, B. Junker, and C. Schmucker, "Efficacy and safety of intravitreal therapy in macular edema due to branch and central retinal vein occlusion: a systematic review," *PLoS ONE*, vol. 8, no. 10, p. e78538, 2013.

[10] I. L. Mcallister, "Chorioretinal anastomosis for central retinal vein occlusion: a review of its development, technique, complications, and role in management," *Asia-Pacific Journal of Ophthalmology*, vol. 9, no. 3, pp. 239–249, 2020.

[11] C. F. Coscas, A. Glacet-Bernard, A. Miere et al., "Optical coherence tomography angiography in retinal vein occlusion: evaluation of superficial and deep capillary plexa," *American Journal of Ophthalmology*, vol. 161, pp. 160–171.e2, 2016.

[12] T. Chandrakumar and R. Kathirvel, "Classifying diabetic retinopathy using deep learning architecture," *International Journal of Engineering & Technical Research*, vol. V5, no. 6, pp. 19–24, 2016.

[13] I. Ardiyanto, H. A. Nugroho, and R. L. B. Buana, "Deep learning-based diabetic retinopathy assessment on embedded system," in *International Conference of the IEEE Engineering in Medicine and Biology Society*, pp. 1760–1763, 2017.

[14] D. S. Kermany, W. Goldbaum, W. Cai et al., "Identifying medical diagnoses and treatable diseases by image-based deep learning," *Cell*, vol. 172, no. 5, pp. 1122–1131.e9, 2018.

[15] M. X. Li, S. Q. Yu, W. Zhang et al., "Segmentation of retinal fluid based on deep learning: application of three-dimensional fully convolutional neural networks in optical coherence tomography images," *International Journal of Ophthalmology*, vol. 12, no. 6, pp. 1012–1020, 2019.

[16] C. Wan, Y. Chen, H. Li et al., "EAD-Net: a novel lesion segmentation method in diabetic retinopathy using neural networks," *Disease Markers*, vol. 2021, Article ID 6482665, 13 pages, 2021.

[17] J. Xu, J. Shen, Q. Jiang, C. Wan, Z. Yan, and W. Yang, "Research on the segmentation of biomarker for chronic central serous chorioretinopathy based on multimodal fundus image," *Disease Markers*, vol. 2021, Article ID 1040675, 11 pages, 2021.

[18] X. Zhang, Y. Xu, and W. Yang, "Annotation and quality control specifications for fundus color photograph," *Intelligent Medicine*, vol. 1, no. 2, pp. 80–87, 2021.

[19] J. Anitha, C. Vijila, A. I. Selvakumar, A. Indumathy, and D. Jude Hemanth, "Automated multi-level pathology identification techniques for abnormal retinal images using artificial neural networks," *British Journal of Ophthalmology*, vol. 96, no. 2, pp. 220–223, 2012.

[20] B. Zheng, Q. Jiang, B. Lu et al., "Five-category intelligent auxiliary diagnosis model of common fundus diseases based on fundus images," *Translational Vision Science & Technology*, vol. 10, no. 7, p. 20, 2021.

[21] D. Nagasato, H. Tabuchi, H. Ohsugi et al., "Deep-learning classifier with ultrawide-field fundus ophthalmoscopy for detecting branch retinal vein occlusion," *International Journal of Ophthalmology*, vol. 12, no. 1, pp. 94–99, 2019.

[22] D. Nagasato, H. Tabuchi, H. Ohsugi et al., "Deep neural network-based method for detecting central retinal vein occlusion using ultrawide-field fundus ophthalmoscopy," *Journal of Ophthalmology*, vol. 2018, Article ID 1875431, 6 pages, 2018.

[23] Q. Chen, W. Yu, S. Lin et al., "Artificial intelligence can assist with diagnosing retinal vein occlusion," *International Journal of Ophthalmology*, vol. 14, no. 12, pp. 1895–1902, 2021.

[24] B. Zheng, M. Wu, S. Zhu et al., "Attitudes of medical workers in China toward artificial intelligence in ophthalmology: a comparative survey," *BMC Health Services Research*, vol. 21, no. 1, p. 1067, 2021.